Simulation and Modeling of Multiple Timescale Effects from Cyclic Capacitive Loads on Thin-Film Batteries

by

Kendall B. Teichert

A dissertation submitted in partial fulfillment
of the requirements for the degree of
Doctor of Philosophy
(Mechanical Engineering)
in the University of Michigan
2017

Doctoral Committee:

Associate Professor Kenn Richard Oldham, Chair
Professor Krishnakumar R Garikipati
Assistant Research Scientist Jason Benjamin Siegel
Professor Dennis Michael Sylvester

Kendall B. Teichert

kbt@umich.edu

ORCID iD: 0000-0002-0653-0497

DEDICATION

This dissertation is dedicated to my wife, Lucy, and to James Hugh, and Flossie.

ACKNOWLEDGMENTS

First off I need to acknowledge the funding sources, that this work was supported by the National Science Foundation [grant numbers NSF CMMI 0954422 and NSF CMMI 1435222].

I would like to thank the many people that helped and contributed to this work. Briefly, I want to thank my labmates and other students that have helped, and provided support and conversation. I want to thank my doctoral committee for their time and help. I would especially like to thank my adviser Prof. Oldham, for his patience and encouragement over these several years.

I need to thank my amazing family, and my wonderful wife who took me into her life during the middle of this crazy time. I'm so thankful for her and our new son who came just in time for me to try to get this dissertation together. And above all I thank God for all His work in my life.

TABLE OF CONTENTS

LIST OF FIGURES

LIST OF TABLES

ABSTRACT

Understanding dynamic phenomena in systems powered by thin-film batteries can be valuable for proper system modeling, design, and control. Some scenarios, such as repeated, fast dynamic loading, may create phenomena at multiple timescales. This could, for example, arise as a consequence of driving common microelectromechanical (MEMS) actuators such as piezoelectric or electrostatic actuators. One application area for these actuators is microrobotics, which is used as a motivating topic throughout this thesis.

This thesis first looks experimentally at switched capacitive loads on thin-film batteries, reporting phenomena such as switching and leakage losses and parasitic capacitance. This data is used in development and implementation of calibration and validation of various modeling approaches. In this modeling, the fast nature of the switching dynamics and the slow nature of the full battery discharge creates a type of multiple timescales problem. To address this, a state projection approach is developed and presented. The initial approach uses a perturbing method to develop a transition matrix to approximate future system states based on past and current changes. This approach captures a full battery discharge with an approximate numerical cost of 6.3% compared to fully modeling all loading event. The next approach uses direct simulation information to reduce overhead in development of the transition matrix reducing numerical cost to 0.46% for the scenario presented. An error analysis was performed to understand errors in the projection process. This error analysis was used to develop an updating approach that increases projection fidelity, further reducing numerical expense to 0.14%. This reduction in numerical cost is part of allowing this approach to be used for design purposes.

Finally, a set of case studies are presented highlighting two topics related to this modeling approach. First, existence of a tradeoff between depth of detail needed in modeling and the severity of the loading applied is presented. Second, example analysis is presented, demonstrating the potential of this modeling approach as a design tool. It is anticipated that through greater understanding of and an increased ability to model these types of battery loading situations, design of microsystems operating in this fashion can be aided.

CHAPTER 1 INTRODUCTION

Energy and power are key issues in society, with importance from policy to research. There is significant effort going into research on energy production, storage, and consumption due to their ever-increasing impact in our lives. One specific area that is of critical interest is that of battery technologies [1]. Batteries are key components in a variety of systems, from small microrobotic applications to large power grid systems. Understanding the specifics of battery use in a given system is important in the design, control, and application of both the battery itself and the system in which it is used. Additionally, this understanding of the battery use, or specific loading of the battery in a given system, can aid in proper selection, implementation and adaptation of required models of the battery. The selection of the battery modeling approach is dependent on the depth of precision needed, the needed model outputs, and the specifics of the loading scenario. For example it is possible for the combination of the battery and associated system to have characteristic changes at vastly different timescales, and consideration may need to be made as to how to handle these. Another potential issue in properly analyzing these types of scenarios is in understanding the inherent error in the modeling for better accuracy or computational efficiency. Ultimately a properly developed model of the battery and associated system can be used to inform design and implementation.

This thesis looks at the modeling of a battery subject to dynamic phenomena with very different characteristic timescales. A primary focus here are thin-film batteries as might be used in microelectromechanical system (MEMS) applications. This introductory chapter will discuss briefly the array of existing battery types, with explanation of batteries particularly suited for MEMS applications. A basic presentation of battery physics will be given. Since the dynamic response of a battery is coupled with the dynamics of the load applied, common MEMS actuation loads will be discussed.

Of particular interest to this work are issues related to modeling of timescale disparities in MEMS battery systems, therefore an explanation of timescale issues with modeling will be presented. Evidence of these various aspects come together in the driving application behind this

work which is a MEMS fabricated microrobot application, and a review of this system will be given. The use of term "multiple timescales" throughout this thesis refers to disparate characteristic timescales of given dynamic phenomena within a system, for example, fast dynamic responses due to e.g. switching loads, and slow changes in accumulated lithium as the battery discharges from repeatedly switched loads. Lastly, an outline of the overall thesis with a brief description of each chapter, will be presented with a list of contributions of this work.

1.1 Battery Varieties

Many dynamical systems use batteries as a form of energy storage, requiring a broad variety of batteries where the specifics of the application guide the battery selection and implementation. For example, battery form factors range from small coin cell batteries (e.g. those in a hearing aid), to prismatic batteries (e.g. cell phone batteries), to cylindrical (e.g. a traditional AA battery), to other forms or configurations (e.g. car starter batteries and batteries for electric vehicles). Additionally there are a variety of different chemistries and architectures [1].

Two research thrusts that have seen a significant amount of attention in regards to battery research over the last several years are the automotive industry and consumer electronics industry. These are driven by several different battery configurations and chemistries. In addition to automotive and consumer electronics, many other applications also use battery power. One example of another area reliant largely on battery power is autonomous microelectromechanical systems (MEMS), having potential application in devices such as medical implants [2] and microrobotics [3-5]. However, battery research in this area seems to have received less attention. A discussion of potential differences in implementation in MEMS applications as opposed to larger devices will be helpful.

Due to the nature of MEMS systems and fabrication, battery implementation has different constraints than larger systems, as such, for MEMS applications there are advantages to thin-film and/or solid state batteries. Thin-film batteries are batteries that have active layers deposited as thin-films. Although, other solid-state battery configurations may also be advantageous in MEMS (such as thick film), and may benefit equally from the techniques described here, they are not addressed directly in this work. These batteries are typically configured with a solid thin-film anode, cathode and electrolyte. This is in contrast to the typical liquid electrolyte used in conventional batteries. This results in several advantages for a MEMS setting with respect to sealing, ease of miniaturization, safety, and battery life [6, 7]. One drawback of the solid

electrolyte, however, is that the ionic conductivity is typically lower than that of traditional liquid electrolytes, though this is mitigated by the reduced thickness of the electrolyte layer [7]. Additionally, due to the reduced risk of shorting across a solid electrolyte, metallic lithium can be used more safely as the negative electrode rather than a carbon based electrode. Several works have looked at the fabrication and materials of thin-film batteries, for example [6, 8]. This thesis focuses on identifying and modeling certain effects in thin-film lithium batteries that are relevant to MEMS devices, as will be explained throughout the text.

1.2 Battery Physics and Modeling

A complete description of the fundamental electrochemical equations for batteries is beyond this work, but a basic introduction into the key aspects in a thin-film battery configuration will be helpful. A typical thin-film battery is composed of three main components: a positive electrode (the cathode during discharge), a negative electrode (the anode during discharge), and the electrolyte. For illustrative purposes the discharge of a typical thin-film lithium battery will be presented.

On discharge the lithium ions are stored in the negative electrode (anode) and diffuse through the electrolyte into the positive electrode (cathode). The potential changes in the battery then occur in five main locations: the electrolyte/electrode interfaces, across the electrolyte, and in the electrodes themselves. In addition to the potential drops in the battery, lithium concentration profiles are also of interest. Determining the modeling approaches of these physics and the proper assumptions will depend on the battery chemistry and the battery loading.

Due to the broad nature of battery research, a variety of different battery-modeling approaches have been developed. Two of the most common modeling approaches, equivalent circuit and electrochemical, are discussed here.

Equivalent circuit models are simplified representations of the physics of the battery system where these physics are approximated by various electrical circuit components. For example, a common simple example is the Randles Model [9] as seen in Figure 1.1. The simplicity and ease of solving makes equivalent circuit models a very common and useful approach in many applications [10-12]. However, as Li et al. has pointed out, one major disadvantage with these types of models is that "it is not easy to directly relate internal physical properties of batteries to model prediction." [13]

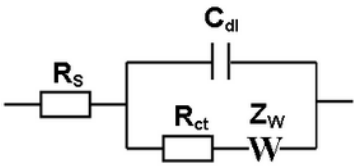

Figure 1.1 Randles model, a simple equivalent circuit representation of a battery (image in public domain).

Electrochemical models are based on the basics physics of the electrochemistry of the system [14-16]. These models overcome the challenge of relating to physical parameters seen in equivalent circuit models; however, this comes at the cost of additional complexity. To reduce the complexity of these models many different simplifications have been proposed in a variety of different models, for example: constant temperature, constant electrolyte conductivity, negligible voltage drop in the negative electrode[14], negligible voltage drop at the negative electrode electrolyte interface [15], single particle approximation for porous electrodes [17], and many others.

1.3 MEMS Loading

In addition to the battery design, loading conditions applied to the battery are critical in determining battery behavior. Many studies have looked at effects of batteries subjected to constant current [18], pulsed [19], resistive [20], and circuit specific loads [21]. There have also been results showing impacts on battery use due to the loading condition [20, 21], with some disagreement in the literature [22]. Although these works may look at different scenarios, they highlight the importance of understanding loading of battery systems.

Two key aspects of the battery loading that can be used for categorization are frequency and electrical circuit equivalence of the load. In MEMS, many actuation types have maximum frequencies in the frequency range (1Hz – 10kHz), see Figure 1.2 modified from [23]. The frequencies shown are approximations of maximum frequencies for the various actuation types, and highlight that this area constitutes a significant range of MEMS actuation. This mid-frequency range falls between low speed mechanical devices that would change loading in the few Hz or less, and power systems, that typically operate at high frequencies.

In addition to frequency of actuation, there are different characteristic physics for the different types of loads. For example, some actuation is current or power driven, such as thermal actuation, or magnetic actuation, whereas others are charge driven, such as, electrostatic actuation and piezoelectric actuation. This charge-driven or capacitive nature of the loading seen

in some MEMS actuators is rarely the dominant loading condition at other scales. The intersection of mid-frequency loading and capacitive or charge driven actuation is characteristic of a significant fraction of MEMS devices as highlighted in Figure 1.2. This type of loading is a type of periodic loading.

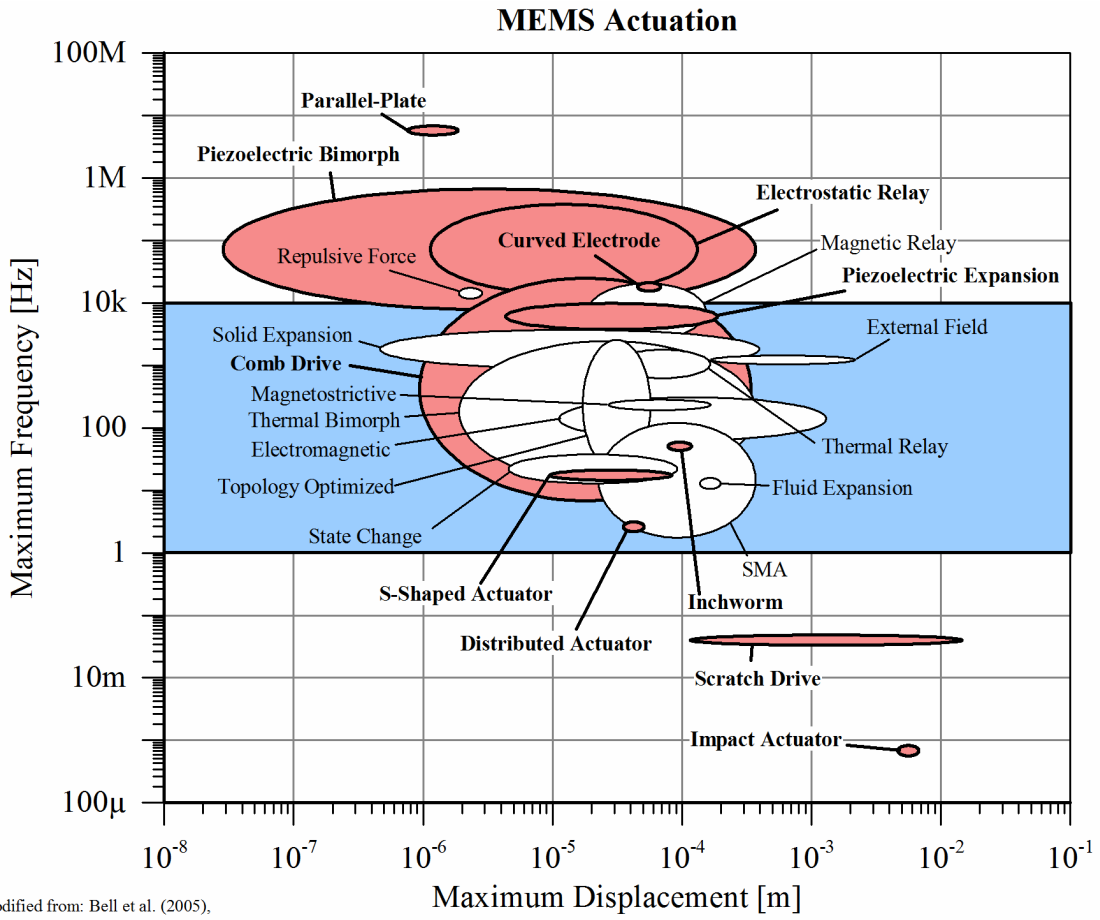

Modified from: Bell et al. (2005),
"MEMS actuators and sensors: observations on their performance and selection for purpose," *J. Micromech. Microeng.* **15** S153-164.

Figure 1.2 Maximum frequency of various MEMS actuation types. Blue highlighted region represents the mid-frequency range common in MEMS actuation. Actuation types that create capacitive loads are highlighted in red. Modified and used with permission from [23].

Fast periodic loading for batteries has been studied in relation to wireless sensing nodes and other circuits, but these are primarily experimental works with coin cell batteries, rather than thin-film batteries. One exception is work by Salloux et al. [24] driving a piezo stack off a thick film polymer battery. Their work focused on experimentally verifying the feasibility of using their battery to drive a piezoelectric stack. This is one example of a low voltage battery (12 and 6 V batteries) being used in a piezoelectric driving configuration. However, the battery used is too large for micro applications, but was suggested for use in sensing nodes. Additionally, only

limited experimental data is looked at, and understanding of the implications on the battery caused by the loading is not addressed.

1.4 Timescales and Model Reduction

When combining the internal dynamics of a battery discharge with external dynamics of the load, dynamics in different timescales can be present. Throughout this thesis we refer to multiple timescale dynamics, to be clear we are discussing dynamic phenomena that have characteristic features at different timescales (e.g. μs vs. hours).

In the context of the current work we are particularly interested in accumulated effects from fast dynamic events over long time periods. As discussed, thin-film batteries provide a potential power source for MEMS devices, which commonly have actuators that operate with a capacitive behavior. The timescale of the dynamics of, for example, piezoelectric MEMS actuation can be in the microsecond range with the individual loading events potentially having significant dynamic effects, yet the battery discharge can be on the order of hours. These overall electrochemical aspects of the battery over its full discharge are a slow accumulation of these individual dynamic events, with electrochemical dynamics potentially varying over many orders of magnitude longer than the individual events.

The bulk of this dissertation examines methods for addressing these types of systems. While the bridging of timescales has been done in various settings [25-29], certain aspects of the dynamics studied here make direct application of some traditional multirate approaches unclear. In particular, the following aspects increase the challenge of modeling this type of battery/load system:

1) A Neumann boundary condition exists in the positive electrode
2) Incremental changes by the fast dynamics drive the slow dynamics
3) Variable coefficients are present (Diffusion coefficient is dependent on concentration)
4) Fast dynamic loads may, in some scenarios, not die out before the next occurs depending on loading conditions.

It may be possible to still apply other multiple timescale methods to the problem studied here, but we have selected a transition matrix approach that will be describe throughout the work.

The issue of multirate dynamics can be particularly difficult when coupled with complex modeling of the battery itself. This can be aided by using different model reduction techniques.

Several reduction methods for battery modeling have been reported, but a few example may be instructive. Santhanagopalan looked at two simplified models for porous electrode batteries to achieve model reduction for models over 1C discharge [30]. Lower current rates were said to be able to be handled with simple models. Kim and Qiao use a hybrid model to take advantage of the simplicity of an electrical circuit model but include some of the more complex dynamics of the battery in a variable voltage source [31]. Gao et al. uses physical data to set up a variable equivalent circuit [32]. Afshar et al. use a mathematical means to converts algebraic differential equations to a set of differential equations in part through linearization of the constraint equations [33]. In this thesis we are primarily looking at thin-film batteries, and begin with including reduction methods outlined by Fabre et al. to use a 1D battery model with constant conductivity in the electrolyte [14] and other approximations.

1.5 MEMS Microrobot Application

One example of a MEMS system that lies at the intersection of the topics covered by this work is piezoelectrically actuated walking microrobots such as those in [34-37]. These mm-sized robots are fabricated using microfabrication techniques. Thin-film piezoelectric actuation is used to provide motion that mimics natural motion in insects. This example will be used throughout the thesis as a basis for loading. The actuation is driven in the Hz-kHz range. One challenge with battery power in this application is that using voltages around 12 volts requires a voltage conversion. Understanding the implications on the power supply of using batteries in series or other voltage conversion circuitry is valuable in making critical design decisions. The design decisions can include tradeoff between energy and weight which can be challenging. For example, Zhang et al. states that this is still an active area of research in their flying insect-scale robot [38], highlighting the value of understanding the effects loading conditions have on battery use in microrobotic applications.

Study of the effects of loading in microrobotic applications typically focuses on the circuit side of the load e.g. in the flying microrobot mentioned above [39]. The simple approach reported for addressing battery effects due to loading in that same system is to use a degrading factor for higher currents to try to capture the losses that occur as stated by Karpelson et. al [40]. It was the aim of this thesis to present more rigorous approaches for analyzing battery effects in this area to aid in design and future research.

1.6 Thesis Overview and Contributions

This work will look at the intersection of various features that are important players in MEMS power systems (battery type, load frequency, load circuitry, and modeling approach). In particular this work looks at modeling and simulation of thin-film batteries subjected to repeated fast-dynamic loads, particularly capacitive loads.

This work is composed of four main sections: experimental observations, electrochemical modeling including state projection approaches to address desperate timescales, projection approach adaptation and error analysis for numerical efficiency, and demonstration/exploration of the modeling approach in various scenarios. Each of these sections is in a stand-alone paper form and several are published or currently submitted which will be noted in each chapter. The papers are presented verbatim including the abstract for ease of access of the various parts. Because of this, some information will be redundant, but should give easier accessibility to those looking in individual chapters.

A brief description of each of these sections will be provided here, along with the associated contributions.

1.6.1 Chapter 2: Experimental Phenomena

The physics of such a complex system as a battery are difficult to fully characterize let alone reproduce analytically. Because of this, modeling approaches require simplifications as mentioned previously. We are interested in the effects caused by cyclic capacitive loading on thin-film batteries. The cyclic loading is often done through some sort of switching mechanism. The dynamics of the switching and the load then create a combined effect on the battery. In order to understand the various aspects of the switching and load dynamics, in connection with the battery dynamics, a suite of experimental tests were run. Through these tests it was possible to determine information for guiding the modeling decisions required. This testing also provided additional insight into certain aspects of the system that were not previously considered, e.g. parasitic capacitance within the order of magnitude of some of the loads was detected in the battery system. This work was publish as [41]. The battery used for the data gathered here and used throughout the thesis was a Cymbet^{TM} [46] 50μAh battery that, although has a chemistry that would likely be applicable for autonomous MEMS, due to packaging and form factor, may not be adequate for all applications, but is useful for demonstration here.

1.6.2 Chapter 3: Model Implementation

With a deeper understanding of the physical phenomena that ought to be incorporated into our modeling, we built on existing modeling techniques to capture these effects. In part, in order to be able to better correlate our model with physical parameters of our system, to allow for design specifications for potential future fabrication, we selected an electrochemical modeling approach. Other approaches could be used, and may still be advantageous in future simplification and applications. However, as a baseline model we used an electrochemical model.

Our model was based heavily on that presented by Fabre et al. [14] which is similar to the works by Danilov et al. [15] and Thomas et al. [16]. Our model incorporated various experimentally observed phenomena. Along with development of the model, a parameter calibration approach was developed and implemented.

One key aspect in modeling this system is the differences in timescale. The dynamics of the switching, battery recovery and capacitor charging can be on the microsecond scale, however, the full discharge of the battery can be on the hour timescale. This disparity of timescales needed to be addressed in order to make modeling of the full battery discharge realistic. A projection style approach was implemented that used a transition matrix to project the states of the battery over several cycles of the load charge/discharge. This work was publish as [42].

1.6.3 Chapter 4: Error Analysis and Model Refinement

The process for creating the transition matrix proved to be numerically expensive when performed on limited processor hardware. To improve simulation speed a different transition matrix approach was developed that obtained the transition matrix in one step instead of one step per state (distributed over processing cores if available). This proved to provide a significant decrease in numerical expense. The error of the approach was analyzed and provided key insight in implementation of error reduction by targeted updating of the transition explored. This allowed detailed understanding of sources of error during state projection. This work is submitted and under review [43].

1.6.4 Chapter 5: Model Application Case Studies

The final portion of this thesis is a collection of case studies that demonstrate the application of these modeling approaches. There are four main case studies that are presented. First, the modeling for the prior chapters will be compared with a simplistic battery model. This model

will incorporate the principles of state projection but will use only the capacity transfered from the battery as the state. This removes the need to calculate the detailed internal electrochemistry of the battery. For the mild loads that have been used it can be seen that this simplistic battery model is adequate. The second case study will look at a higher average current load, and here we will see that the simplistic battery model begins to deviate significantly from experimental data, thus demonstrating the value of the full model over a more simplistic electrochemical model. The final two scenarios will explore battery modeling in alternative system configurations. These include a scenario with batteries in series and a boost converter circuit. Through these case studies we are able to highlight the aspects of these techniques reported in this work in additional circuit and battery configurations.

1.6.5 Contributions

Among the main contributions of this work are the following:

1) Experimentally observed characteristics of switching loads on thin-film batteries,
2) Augmented existing thin-film battery models to explore fast cyclic dynamic loads on thin-film batteries,
3) Addressed modeling of dynamics in these systems with disparate timescales through a transition matrix approach,
4) Addressed numerical cost in transition matrix approach by changing system state definitions,
5) Performed error analysis on projection approach that enabled targeted error reduction,
6) Provided several scenarios to demonstrate the use of these techniques, and their relation to autonomous MEMS systems.

CHAPTER 2 EXPERIMENTAL DYNAMICS AND CHARACTERISTICS[1]

2.1 Abstract

Piezoelectric actuation has potential advantages in autonomous microsystems due to relatively high efficiency and low voltage requirements when deposited as a thin-film. However, the power available to autonomous microsystems may have many restrictions due to electrical loading, weight, and size requirements. Modeling of the power sources and loads can be beneficial for design and implementation; however, understanding the various associated phenomena is important for a valid model. This work examines mid-frequency cycled capacitive loading of thin film batteries to simulate application to autonomous micro-robots. Commercial 50μAh $LiCoO_2$/Lipon thin film batteries were cycled over a frequency range between 100Hz-10kHz and at two levels of capacitance (1, 10nF). Detailed data was acquired of the dynamics of the battery and capacitor voltages during switching. The significance of understanding losses from switching and leakage at the micro scale is clearly shown. The impact of similarity in timescales for various dynamics is discussed. Additionally, indications of parasitic capacitance in the battery system are seen and discussed. An example implementation of the findings in a switching model is presented as well as a simple design application example.

2.2 Introduction

Power-sourcing for microscale autonomous applications presents certain challenges due to size, weight, and fabrication constraints. One such application is that of walking micro-robotics powered by piezoelectric actuation [37]. These actuators are operated at frequencies in the range of tens to hundreds of Hz [37, 44]. Switching circuitry is needed, and additionally voltage conversion may also be needed which would operate at much higher frequencies [45]. If one

[1]

were to drive the actuators directly from the power source, the electrical load of thin-film piezoelectric actuators can be approximated as a simple capacitor. The combination of the cyclic nature of this application with the very dynamic load profile of a charging capacitor requires a more thorough look at the power source and the effects of such dynamic loading on an already design-constrained component.

Various types of micro-batteries are discussed in the literature with a variety of different chemistries [6, 8]. One that is commercially available is $LiCoO_2$ [46]. Although the exact size and form is not the same as would be in a walking robot, these batteries offer a platform to explore loading effects on thin film batteries under cyclic capacitive loading conditions. Work has been done by others indicating that loading profiles of coin cells affects battery useful capacity [20, 47]. There has been some debate over whether pulsed loads are advantageous or not [19]. However, information about a pure cyclic capacitive load seems lacking in the literature.

This paper presents experimental results of thin film batteries under cyclic capacitive loading to simulate walking micro-robotic actuation. The primary reason for this work was to see if we could detect any effects on battery capacity due to switching speed and load characteristics under these conditions. Experiments were performed on thin film $LiCoO_2$ batteries. For simplicity, no voltage conversion/boost circuitry was used, and potentials were kept at a those supplied by a single battery. Insights and conclusions from this study can be used to add to the foundation for future design of robot gait, control, and circuitry.

In addition, these results highlight the timescales of battery, switching, and actuator dynamics. In this application, timescales of these three can be very similar causing critical interplay between their dynamics. Understanding this characteristic can aid in proper implementation of things like model simplifications or refinements. For example, it may not be reasonable to assume an ideal power source when the timescale of the changes in the battery voltage during switching are similar to the time it takes for switching to occur or for the capacitor to show significant charging.

This testing also demonstrates potential losses that this microscale system can encounter. The purpose of this paper was not to determine a better switching approach, or present lower leakage current circuits, but rather by using a simple circuit and switching approach to assess the effect of capacitive load switching on the battery. The losses that are seen and reported here only

highlight the importance of addressing loses especially in microscale switching circuit as mentioned by [37, 44]. Additionally, by using a variety of different loading conditions it is possible to understand the potential tradeoffs that occur in applications with switched capacitive loads. Finally, an example implementation of these findings into a switching model is presented.

2.3 Experimental

2.3.1 Setup

There were three main components of the experimental setup: the battery, circuitry, and data acquisition. Cymbet^{TM} 50μAh rechargeable batteries were selected for these tests (batteries were tested in a packaged configuration, however, only a bare die is currently available) [46]. Although exact specifications are not all reported, the information given in the safety specifications indicates that these batteries are a thin-film $LiCoO_2$/LiPON likely in a "Li-Free" configuration where the lithium anode is plated on the current collector during the initial charging [48]. These batteries offered a viable chemistry for future use in walking micro-robotics even if the form factor is currently not suitable. Five individual batteries were used in these tests, with multiple tests performed on each battery (not all tests reported here).

The switching circuitry was implemented on a PCB and included a simple h-bridge switching configuration, as shown in Figure 2.1.

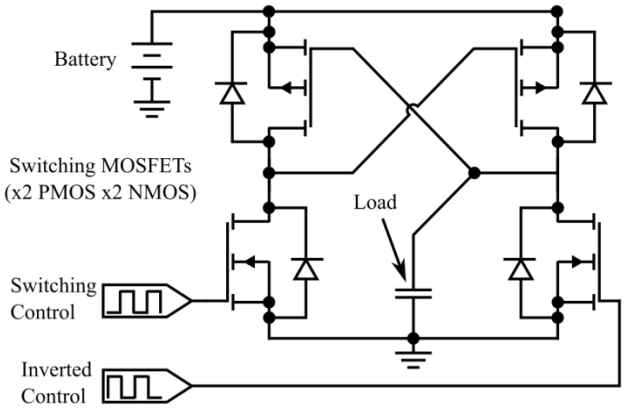

Figure 2.1 Switching circuit schematic. Switching performed by an H-bridge with 4 MOSFETS (2 PMOS, 2 NMOS). The load was 1 or 10 nF capacitor or 10k, 100k or 1M Ω resistor. Circuit switching design based on [11].

The battery was mounted on the PCB using a simple socket for easy replacement. The PCB was designed for easy changing of load components (capacitor/resistor). MOSFETs were selected for their response times and for their low capacitance (ON Semiconductor PMOS Part# NTR1P02T1G: 165pF input capacitance; NMOS Part MGSF1N02LT1G: 125pF input

capacitance). A square wave was used to drive the switching and was supplied to the circuit by a National Instruments DAQ card (NI USB-6211) controlled through LabVIEW. External power was supplied for powering circuit op-amps, an inverter used for mirroring the square wave for switching, and a low drop-out regulator used in battery charging.

Data acquisition was performed by two separate means. The NI DAQ was used to acquire low sample-rate data of the battery voltage and the voltage across the load. The DAQ also provided triggering signals for the switching control and data capture. Detailed switching dynamics of capacitor charge and discharge were captured periodically using an oscilloscope (Agilent DSO-X 2024A). LabVIEW was used for the main logic/control platform. Additionally, an AC current probe (Tektronix CT-6) was used near the battery terminal to acquire the total current leaving the battery.

2.3.2 Testing Parameters and Approach

Load type (Capacitor/Resistor), load size, and switching frequency were parameters varied between test runs. The load elements used included: 1MΩ, 100kΩ, and 10kΩ resistors and 1nF and 10nF capacitor. Effects of other aspects of the setup and experiment are not addressed.

Testing was conducted approximately as follows: (1) at least thirty minutes rest time for the battery, (2) battery charged at constant 4.1V for at least thirty minutes, (3) at least thirty minutes rest period to allow the battery to partially equilibrate, (4) cyclic loading until the battery voltage dropped below 3.3V (resistive loads were not cycled).

Voltages of the battery and capacitor were logged as well as current probe measurements. The data was analyzed to determine different ways the capacity of the battery was expended. In this paper “useful capacity” is either the power consumed by the resistive load, or the amount of charge transferred from the battery to the load capacitor (the capacitor represents the actuator, so charge stored roughly correlates to actuation). “Leakage current” is the amount of current consumed by the circuitry. A relationship of voltage to leakage current was determined by replacing the battery in the circuit with a power supply (Keithley 2400 Sourcemeter) and monitoring the current flow at various voltages in the on and off states of the switching circuit with the load element removed. “Switching loss” is the loss during switching. These were determined using data from the current probe and calculated as follows: during switching, the current out of the battery minus the amount of current into the capacitor, as indicated by the charge, and the leakage current.

2.3.3 Limitations

Current Probe Data: In this test setup an AC current probe was used. To convert these readings to DC current, an approximate transfer function of the probe was developed using a combination of experimental data and the probe datasheet, and subsequent slope adjustment was performed. Because of this, current measurements and switching losses are accurate only to the accuracy of the probe model.

O-scope Data: Some data sets contained corrupted data, where possible this was replaced with approximate data using adjacent data. Additionally, some of the current spikes during switching were clipped by the O-scope window settings. Also during charging, the capacitor voltage would often read higher than the battery voltage, the source of this error was not determined, but the discrepancy is shown in the error bars of the figures were necessary.

DAQ Data: Issues with noise or spurious signals were seen in the data, but overall trends are considered correct.

Charge/Cutoff Voltage: To adjust for some variations in charging and cutoff voltages, a correction was made to overall run data to adjust to a common voltage. This correction is seen only in the data presented in Figure 2.4F.

Additional Variation: Variation from battery to battery was not analyzed. Some variation/refinements in testing procedures occurred over the set of testing, for example often batteries were left overnight before charging or testing. The first run for all batteries was the 1MΩ run. Charging time for all runs was 30min with the exception of the first run for each battery which had a 60 min charge time.

2.4 Results and Discussions

The experimental results and discussion are separated into four sections. First, the detailed dynamic profile of switching will be presented. Second, comparison and discussion of the losses from different scenarios will be shown. Third, a discussion and evidence of parasitic capacitance in the battery will be explored. Finally, an overall discussion of the combination of these different findings will be given.

2.4.1 Switching Dynamics Profile

Figures 2.2 and 2.3 show typical switching profiles for a 10nF and 1nF capacitor load respectively. The basic sequence of switching events starts with the battery at rest and the

capacitor with zero charge. As the switching circuit begins to switch there is a spike of current from the battery as the battery has a momentary connection to ground. The battery voltage is pulled down to the switching voltage dictated by the MOSFETs. Once the battery reaches this switching voltage there is a slight delay before the capacitor starts to charge. Once the capacitor starts to charge, and until it reaches the battery voltage, the charging is approximately linear.

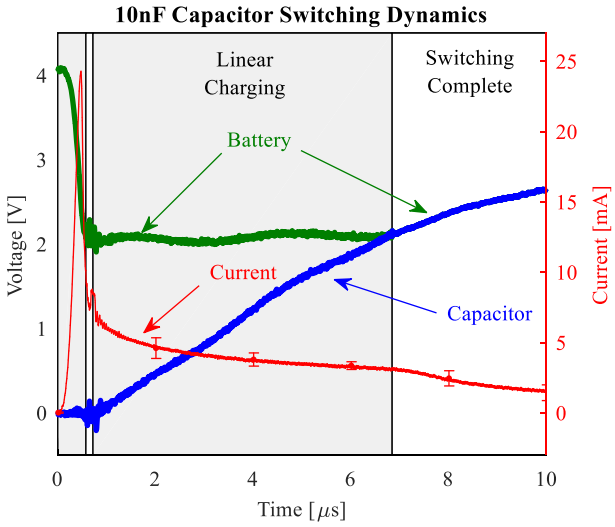

Figure 2.2 Switching dynamic profile for 10nF capacitor. Battery voltage (green), capacitor voltage (blue), and current out of the battery (red) are shown during the switching process for a 10nF capacitor. Relative timescales can be seen for the battery, switching, and capacitor dynamics. Error bars for the current are the standard deviation of a moving average before measurement adjustment not absolute error.

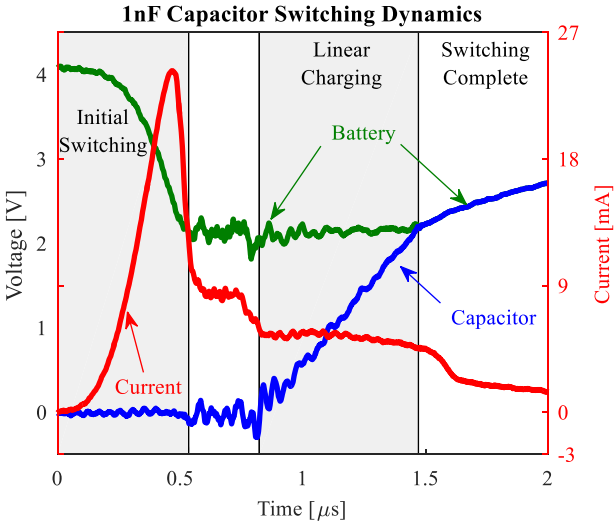

Figure 2.3 Switching dynamic profile for 1nF capacitor. Battery voltage (green), capacitor voltage (blue), and current out of the battery (red) are shown during the switching process for a 1nF capacitor. Relative timescales can be seen for the battery, switching, and capacitor dynamics. Rolling average error for current during a spike has limited meaning and is omitted.

This is dictated again by the switching circuit which holds the battery at a set voltage/current. After the capacitor has reached the battery voltage it is assumed that switching is complete and the capacitor charging and battery rise approximately together. In the figures, switching is initiated at time zero as determined by when the current begins to rise.

These switching dynamics are not particularly novel, but it is critical to notice that charging of the capacitor, battery response to the switching, and switching dynamics are all on a similar timescale. This is especially true in the 1nF capacitor scenario (Figure 2.3) which is a typical size for the actuator capacitance in our walking robot application. This similarity of timescales is important in that it the effects of any one aspect cannot be neglected. By recognizing this similarity of timescales future modeling approaches can be better informed about the importance of simplifications in regards to battery, switching and capacitor dynamics.

Additionally these results demonstrate aspects of the switching dynamics that may need to be considered in future modeling. These other effects include lag in the switching as well as a "linear" charging region seen. This linear region is caused by the h-bridge configuration used.

2.4.2 Capacity Use Distribution

Various testing scenarios were performed to determine effects capacitor size and cycling frequency have on useful battery capacity. A brief comparison of the types of losses seen in this work is given in Figure 2.4. Losses at low-power, micro-scale applications can be very high (as seen here even up to two to three times larger than the useful capacity in some scenarios). Approaches to increase efficiency and reduce loss can be seen in the literature including [49-51] and is not the point of this work, rather we want to reiterate that these losses should not be disregarded, and the design of the circuitry is important.

Several general points can be taken from this data:

1) Leakage and switching losses can account for a substantial portion of the battery capacity used on this scale.
2) There is interplay between the switching speed, load size, and total capacity of the battery consumed.
3) Battery discharge of resistive loading and cycled capacitive loading have similar lifetime profiles. However, as seen in Figure 2.2 and 2.3 there are significant dynamics occurring at the faster timescale.

4) Leakage loss is proportional to total test time, switching loss and useful capacity are proportional to number of switches. However, the size of the load, current draw of switching and load, and the speed of switching dictate the battery relaxation, and thus the overall time. Therefore there is an interdependence of all of these that needs to be considered.

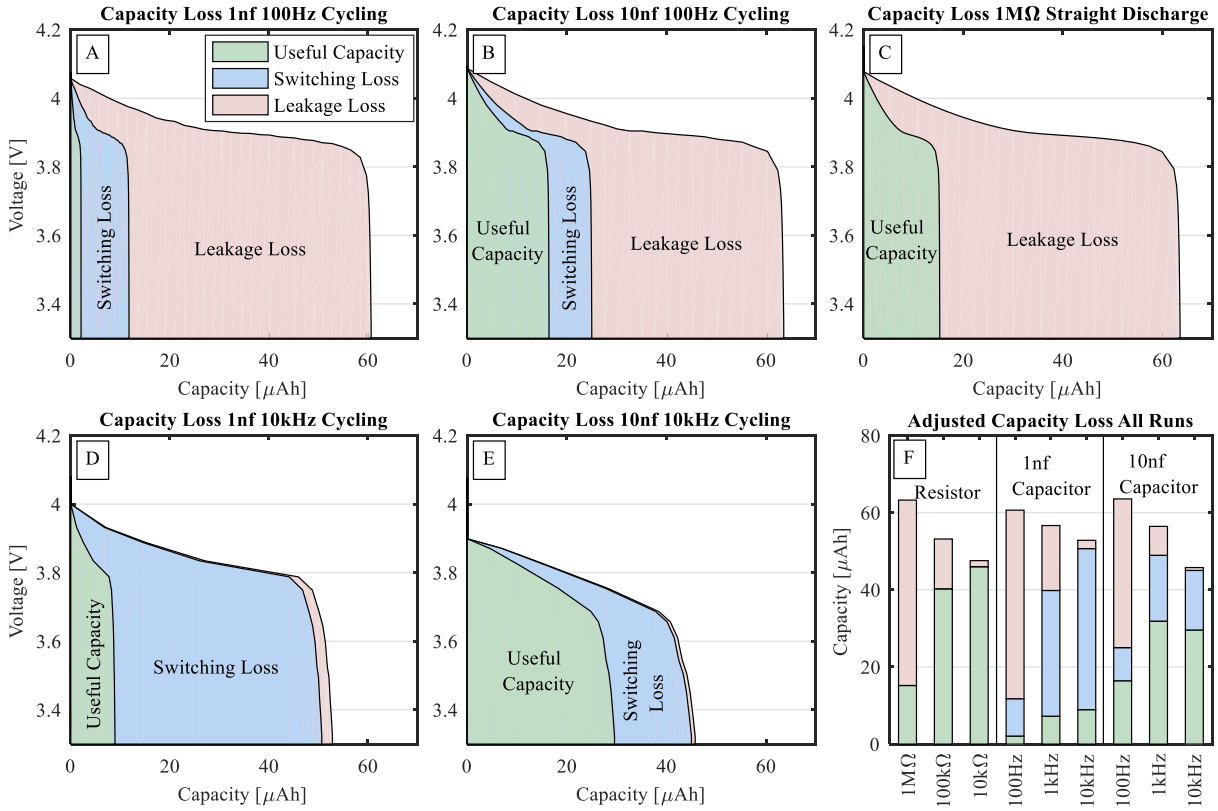

Figure 2.4 Capacity and loss distributions for various test runs. The distribution of typical leakage and switching losses compared to the useful capacity is shown for (A) 1nF at 100Hz (B)10nF at 100Hz (C) 1MΩ DC (D) 1nF at 10kHz (E) 10nF at 10kHz. The data presented in (F) was adjusted to a common starting and cutoff voltage, a few of the tests had multiple runs, but only a sample run for each configuration is shown. (F) is corrected since publication in [41].

2.4.3 Parasitic Capacitance

In all tests there was seen a sharp current spike during the initial switching. It was suspected this was due to parasitic capacitance built up in the battery or circuitry that quickly and easily discharged when the switching briefly shorted to ground (see Figures 2.2 and 2.3).

In addition to the current spike, there were other signs of parasitic capacitance. At the end of the linear charging region in the 1nF capacitor test shown in Figure 2.3, there is a distinct change in slope. The amount of current the battery is able to supply as a function of battery voltage should be a smooth function. As the capacitor is charging during the linear portion, the battery is

fixed at the switching voltage and thus a set current. It is assumed that the parasitic capacitance is held at the battery voltage also. After the switching voltage is reached the battery then has to charge the internal parasitic capacitance and the external capacitor. The addition of this parasitic capacitance charging causes there to be less current available to charge the external capacitor resulting in slower charging and causing an abrupt change in slope in the capacitor charging profile. This is somewhat apparent in the 10nF capacitor data as well but the effect is less pronounced.

One additional test was performed to verify the parasitic capacitance. A manual switching test was performed where the battery could be hooked directly to a capacitor. The circuit was manually closed and the response of the capacitor charge was recorded on the oscilloscope (see Figure 2.5). The bandwidth of the o-scope probes was 300MHz with approx. 15pF capacitance in the probe. The initial jump in voltage of the capacitor indicates a readily available store of charge from the battery. After this initial charge is passed to the capacitor the remaining charging follows a more typical profile. The ringing indicates some inductance in the system.

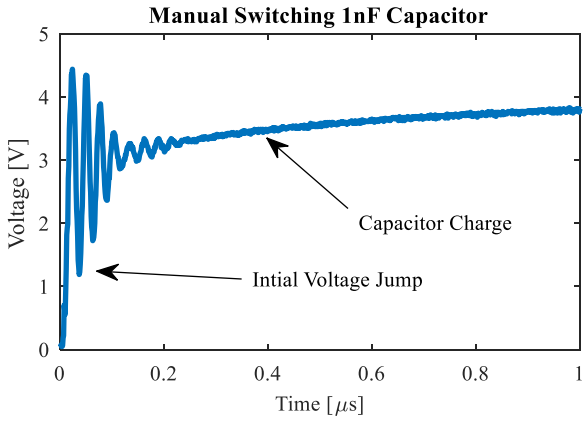

Figure 2.5 Capacitor charge with a manual switch test. The initial jump in voltage indicates a large, readily available current source, such as a parasitic capacitance. The ringing is likely from inductance in the system.

The implications of this parasitic capacitance can be important. With the switching circuit used for this testing there is an initial period during the switching where a momentary path to ground is formed from the battery. If the current is limited by the internal resistance of the battery, losses are kept in check. However, the parasitic capacitance is not checked and thus can dump all of the charge stored parasitically to ground very quickly. Each cycle, this may be a small amount, but over thousands of cycles, these losses can become significant. Considering these losses in the switching design will be important. Additionally, there may be approaches that could take advantage of the initial current.

From a modeling standpoint, adding the parasitic capacitance will be important in that this capacitance may be on the order of magnitude as the actuators themselves. This is seen in the percentage of the voltage that is charged in the initial jump in Figure 2.6. This highlights again the errors that could arise from improper assumptions/simplifications. Further testing is needed to determine if the origin of this capacitance is from the battery and/or packaging.

2.5 Implications

2.5.1 Modeling Details

A basic switching model was developed that incorporates aspects of phenomena discussed here. This electrochemical model is adapted from that developed in [14-16] and is based on a current balance of the different sections of the battery. Aspects of this testing that are incorporated include: time to pull battery to switching voltage, time to begin switching, switching voltage, assumed resistance during switching, and parasitic capacitance.

Parameters were optimized for fitting of a single charge and discharge profile for a 10nF capacitive load. Certain switching characteristics were determined experimentally and the battery parameters (including parasitic capacitance) were optimized by fitting data for a single cycle. Comparison of the experimental data and model can be seen in Figure 2.6. Continuing work is expanding the analytical model and working towards blending the fitting at the micro time scale shown here, with full battery discharge curve fitting.

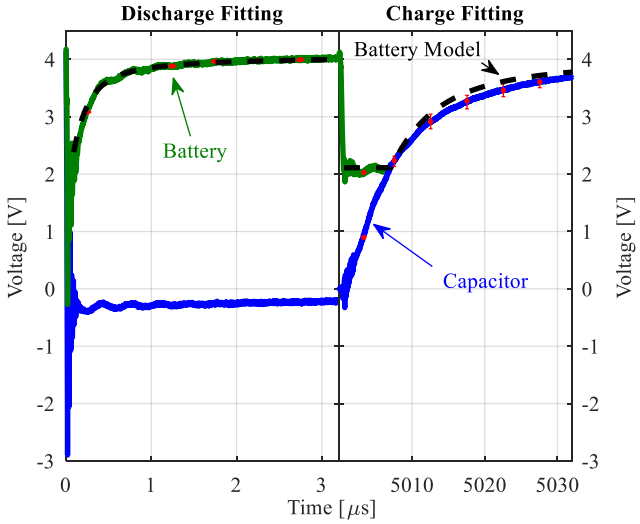

Figure 2.6 Model fitting. Capacitor discharge and charge data is shown for a 10nF 100Hz test. Aspects of this work are incorporated into the model to capture various switching and battery dynamics.

2.5.2 Systematic Design

Trends in power usage may also be incorporated into design characteristics of micro-robots or other autonomous micro-systems, with substantial influence on feasible operating capabilities. To demonstrate how this information might be used, a simple example is shown. In practice, such an analysis would be preceded by improvement of switching drive circuits to better accommodate battery and switch transient behavior, but the concept below may be instructive.

A basic system-level analysis of a walking micro-robot can be performed by simplifying the basic motion equations. In this analysis, the goal is to compare the effects of varying the number of actuators used in a robot leg, N_{act}, which for a given robot payload effectively exchanges leg speed for range of motion, while varying capacitance of the system. A simple hybrid schematic of a robot is shown in Figure 2.7.

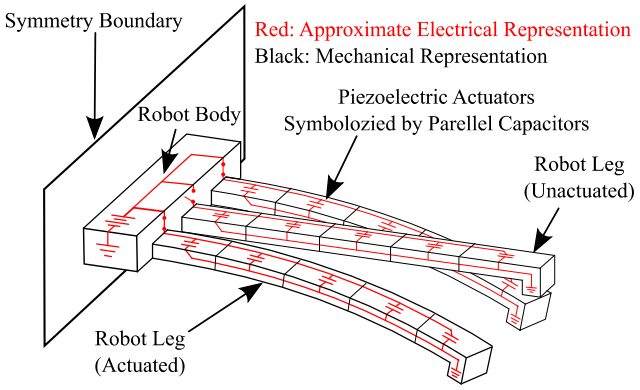

Figure 2.7 Robot schematic. A hybrid representation of a half view of a sample micro robot. The electrical diagram represents the physical actuators where additional actuators increse the length of the leg.

To begin, the distance traveled per step for piezoeletrically-driven robot legs can be approximated as:

$$d_{step} = \alpha \frac{N_{act}}{k_{nom}}, \tag{2.1}$$

where d_{step} is step length, α is a proportionality constant that depends on the piezoelectric material and actuator design, and k_{nom} is the nominal stiffness of an actuator. For this example, all actuators are assumed to be 1 nF arranged in a parallel electrical configuration, so the capacitances are additive; this is the typical piezoelectric element size for actuators developed by the authors and their collaborators, although the typical voltage conversion circuitry is omitted here for simplicity. For a given frequency and capacitor size, system efficiency can be determine

using a cubic fit for the data based on Figure 2.4F. Choosing f and N_{act} as our design specifications, and assuming that robot payload is selected so that f is near the natural frequency, an effective mass of the robot, m_{eff},can be calculated as:

$$m_{eff} \approx \frac{k_{nom}}{N_{act}(2\pi f)^2}. \tag{2.2}$$

The total distance traveled for the robot modeled in Equations 2.1 and 2.2 is based on the charge/step and the number of steps:

$$C_{tot} = N_{act}C_{nom}, \tag{2.3}$$

$$Q_{chg} = C_{tot}V_{nom}, \tag{2.4}$$

$$N_{step} = \eta(\mathrm{f}, C_{tot}) * \frac{Q_{batt}}{Q_{chg}}, \tag{2.5}$$

$$d_{tot} = \alpha * \eta(\mathrm{f}, C_{tot}) * \frac{Q_{batt}}{k_{nom}C_{nom}V_{nom}}, \tag{2.6}$$

where C_{tot} is the total capacitance of the actuators, C_{nom} is the nominal capacitance of the actuator, Q_{chg} is the battery capacity needed to charge the actuator, and V_{nom} is the nominal voltage to which the actuator is charged, Q_{batt} is the total capacity of the battery, η is an efficiency of battery use of the switching/circuitry as a function of f and C_{nom}, and N_{step} and d_{tot} are respectively the total steps taken and total distance traveled by the micro-robot on one battery charge.

The robot parameter values that were chosen are given in Table 2.1, and are merely representative and not physical, for more information of possible physical values see [34, 37]. The percent useful capacity determined earlier was used to determine the portion of the full 50μAh charge that could be used. It was assumed that batteries were configured in parallel to have an average 15 V charge for easier comparison to other data.

Table 2.1 Listing of parameter values used for example analysis.

α	C_{nom}	k_{nom}	$Q_{battery}$	V
3 mN	1 nF	10 N/m	50 μAh	15 V

The ideal scenario would be one that offered the farthest travel distance with the greatest payload potential. Here we use effective mass as a payload metric. Over the range of 10-1000Hz and 1-10 actuators the mass and distance values were normalized using the max value in that

range. The tradeoff can be seen in Figure 2.8. It can be seen that in this design space, the highest distance traveled gives the lowest payload. The dashed upper plane represents what the distance traveled would be if the efficiency were assumed 1 (normalized to the maximum d_{tot} value in the design space).

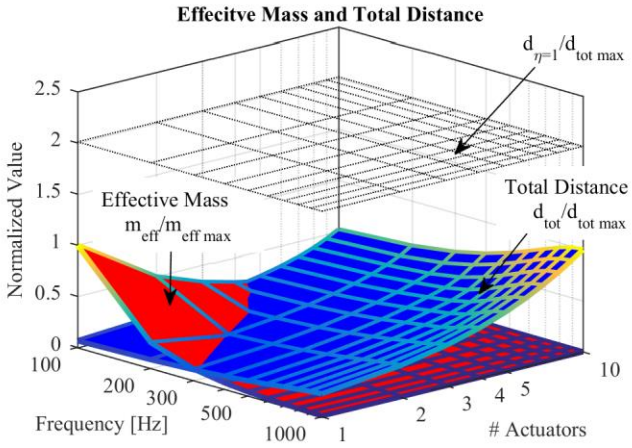

Figure 2.8 Analysis of payload (estimated by effective mass) and total travel for a given frequency and capacitance/N_{act}. Mass and distance are normalized by the max value in the input ranges. The dashed plane represents the total distance traveled if efficiency is assumed one and normalized with the $d_{tot\ max}$.

Again, it should be emphasized that this analysis does not take full account of opportunities to use battery dynamics to refine switching circuit performance, and considers only abstract leg details. In addition, much of the space shown is not physically realizable, chiefly at very high operating frequencies corresponding to low robot mass. However, this type of analysis demonstrates potential design questions that could be aided by the type of information reported here.

2.6 Conclusion

We have presented experimental data for cyclic capacitive loading of thin film batteries. The interplay between these loads and the batteries can be seen and needs to be accounted for in proper modeling of these systems. Important observations include various characteristics such as timescales, relative losses, and parasitic capacitance. Additionally, incorporation of these into a model of the switching dynamics was shown. Additionally, a sample design problem was given. Future work includes the life cycle modeling of a complete battery discharge, and parameter fitting for not merely one cycle but the combination of a single cycle and the full discharge profile. It is hoped that this work can help to inform modeling and design of gait, control, and circuitry of walking micro-robots and power management in autonomous microsystems.

CHAPTER 3 INITIAL MODELING APPROACH[2]

3.1 Abstract

Previous modeling of thin-film batteries has primarily looked at simple discharge loads. This work examines modeling of mid-frequency dynamic loads with large variation in current during repetitive loading cycles, a type of loading that is very common in microelectromechanical system (MEMS) applications. Here we show an extension of traditional modeling of thin-film batteries to account for switching and capacitive loading representing piezoelectric or electrostatic microactuation. This model captures behavior at both fast and slow timescales, including effects of short-duration, high-current spikes. We show validation of the model and introduce a cycle projection scheme that allows for over 94% reduction in numerical calculations over a full battery discharge which includes over a million cycles.

Table 3.1 List of symbols for Chapter 3

Symbol	Description	Units
α	Charge transfer coefficient	[-]
δ	Normalized concentration perturbation size for transition matrix construction	[-]
ε	Normalized concentration perturbation effect	[-]
κ	Conductivity	[S]
π	Non-dimensional parameter	[-]
φ	Coefficient for normalization	Varies
A	Area	$[\mathrm{m}^2]$
c	Concentration	$[\mathrm{mol}/\mathrm{m}^3]$
C	Capacitance	[F]
D	Diffusion coefficient	$[\mathrm{m}^2/\mathrm{s}]$
D_0	Nominal diffusion coefficient	$[\mathrm{m}^2/\mathrm{s}]$
F	Faraday's Constant	$[\mathrm{C}/\mathrm{mol}]$
I	Current	[A]
I_{Leak}	Leakage current through the switching circuitry	[A]
I_{Switch}	Current lost through switching	[A]
i_0	Exchange current density electrode/electrolyte interface	$[A/\mathrm{m}^2]$
L	Thickness	[m]
R	Universal gas constant	$[\mathrm{J}/(\mathrm{mol\ K})]$

Symbol	Description	Units
R_{switch}	Approximate resistance in limited path to ground during t_{charge}-t_{comp}	[Ω]
T	Temperature	[K]
$\boldsymbol{T}$	Transition matrix	
t	Time	[s]
t_{charge}	Time at beginning of capacitor charge	[s]
t_{comp}	Time at switching completion	[s]
t_{hold}	Time at beginning of the delay	[s]
t_{switch}	Time at switch initiation	[s]
U	Open circuit potential	[V]
V	Voltage	[V]
V_{Batt}	Battery Voltage	[V]
$V_{Batt,Nom}$	Nominal battery voltage at full charge (4.1V)	[V]
V_{th}	Switching threshold voltage	[V]
x	Spatial coordinate	[m]
y	Normalized Li concentration	[-]

Sub/Superscript		
+/-	Positive negative electrode	
a	Anodic	
c	Cathodic	
cap	Load capacitor	
e	Electrolyte	
k	Total number of spatial grid points in finite difference	
linear	Time during which the load capacitor has an approximate linear charge	
m, i	Finite difference spatial grid point	
max	Max value possible	
n	Cycle number	
p	Number of cycles projected	
para	Parasitic capacitor	

3.2 Introduction

Limitations of available power sources, such as batteries, place significant constraints on design of engineered systems at many scales, from vehicles to microelectromechanical systems (MEMS) [2]. Battery modeling can be used to help navigate these limitations, and many different modeling approaches have been developed [14, 52]. This work focuses on adapting existing modeling approaches to capture cyclic, capacitive loading (i.e. repeated charging of a load that behaves approximately like a capacitor) of thin-film batteries, a loading which is very common in, for example, MEMS applications. Additionally, for small-scale systems, all-solid-state batteries are an attractive alternative to more traditional liquid electrolyte constructs in that sealing of the liquid electrolyte is avoided [6], generally providing better size and assembly compatibility with micromachined devices. These solid electrolytes typically have lower ionic conductivities, but the effects of this are mitigated by the reduced thickness at which these thin films can be deposited [7]. Various studies have looked at the different properties of various

battery chemistries and configurations [7, 8, 53-58], which is still a very active area of research. However, modeling of cyclic capacitive loads seems to be lacking in the literature.

Understanding the implications of cyclic loading on batteries is important. There have been mixed reports on the broader loading category of intermittent loads on batteries at various scales. Several reports have indicated that loading conditions can have substantial effects on the battery output ability. Fuller et al. [59] discussed different relaxation phenomena in lithium-ion insertion batteries. Feeney et al. [20] recently demonstrated, on a specific primary Li-ion battery, the effect of loading conditions on overall battery capacity utilization, using square wave resistive loads. In that study, experimental results were used to show that the duty cycle had a significant impact on the battery's usable capacity. In an earlier work from Park et al. [21], experimental results also showed that loading conditions have a significant impact on battery usable capacity. Their work was based on the load created by a DCDC converter. In contrast, Castillo et al. [22] provides experimental observations for intermittent discharge showing no effect for Li-ion rechargeable batteries. It should be noted that the conditions, batteries, and loadings are not consistent in these studies, but rather highlight the potential difficulty of fully understanding and modeling intermittent loading conditions.

In applications such as MEMS, understanding loading effects on the battery will be important in light of small system size, weight, and power targets. MEMS-based micro-robots, for example, must operate under very strict power limits and with finite power system payload capacity. Often, electrical circuitry for low powered application can also be very inefficient [45], requiring additional battery capacity which can come at a premium in the often "footprint limited" area of MEMS. Moreover, some of the most common MEMS transduction mechanisms (i.e. electrostatic, piezoelectric) act as primarily capacitive loads resulting in high-speed, high-current intermittent discharge from batteries, which is both less common and less desirable in most larger-scale battery applications. Piezoelectrically-actuated walking micro-robots [37, 45], give a platform for understanding these types of loading conditions having mid-range operating frequencies (10^{1}-10^{3} Hz) and small capacitances (10^{-10}-10^{-8} F).

As stated above, the purpose of this work is to adapt existing modeling approaches to capture cyclic, capacitive loading of thin-film batteries. There are several challenges with modeling and analyzing this type of loading condition, yet by proper modeling, greater understanding and direction can be had in design and control. Recently we experimentally showed effects of

switching capacitive loads on voltage profiles of battery outputs [41] (see chapter 2). That work highlighted various phenomena related to the loading and circuitry, and presented a brief demonstration of one cycle of this modeling approach without modeling details. Here we detail the incorporation of key phenomena into a full switching model to capture effects of cyclic capacitive loading on thin-film batteries. We choose to use an electrochemical approach to more readily correlate between physical properties and the model parameters. This model was based heavily on work presented by Fabre et al. [14] and Danilov et al. [15] and more detailed descriptions of the electrochemical equations can be found there, as well as prior work by Thomas et al. [16] This basic model foundation was then adapted for our loading conditions as well as to include switching and other phenomena seen experimentally [41] (see chapter 2). Model parameters were found using a fitting optimization approach that was developed to correlate the model with experimental data.

Meanwhile, to model faster timescale dynamics of cycling requires a significant numerical cost. A typical battery discharge in our testing could be over a million cycles for some of the tests run. In order to show model responses across the full battery discharge, a projection approach was developed that allowed for projecting battery states over many cycles to reduce numerical modeling costs. By incorporating system characteristics of cyclic capacitive loads on thin-film batteries at very different timescales and current levels, this combined modeling and simulation approach should enable greater understanding and capabilities in design and control of devices operating in this manner.

3.3 Modeling Development

3.3.1 Modeling Background and Assumptions

Two widely used approaches for battery modeling are equivalent circuit modeling, where battery responses are modeled using an analogous electrical circuit [12, 52, 60, 61], and physics-based models [14, 15, 62]. This work is based on physics-based approaches, adapted from solid-state battery modeling presented by Fabre et al. [14] and Danilov et al. [15]. We expand the use of this model to account for and investigate fast dynamics in the electrochemical system. Fabre's model gives a 1-dimesional description of an all solid-state thin-film Li/LiPON/Li_yCoO_2 battery with the following assumptions made to simplify the problem: (1) isothermal behavior with no self-heating, (2) Li electrode acts as a perfect conductor with negligible voltage drop, (3)

negligible volume changes, and (4) constant electrolyte concentration/conductivity. In this work we choose to neglect the voltage drop in the positive electrode. At conditions where constant electrolyte conductivity can be approximated it is assumed that the resistive drop in the positive electrode will be moderate (e.g. using the conductivity of $LiCoO_2$ in Park et al. [63], and the parameters approximated later in this work the positive electrode resistance would be ~3% of that of the electrolyte) and can be compensated for in other parameters. Under this assumption and in light of the increased simplicity of modeling (reduction of unknowns from 5 to 4), this approximation seemed justified. In this paper the loading applied (10nF 100Hz) allows the battery significant time to recover between major switch/charging events, at higher frequencies or higher average currents both the electrolyte conductivity and the positive electrode resistance assumptions (in addition to other limiting assumptions) will likely need to be readdressed. Finally, only battery discharge is considered.

Key equations for the model will be given here; for a more thorough derivation see the source literature [14-16]. Notation will be kept similar to the source literature for convenience. The coordinate system and battery schematic are shown in Figure 3.1. and remain similar to Fabre et al. [14], where the boundary of the negative electrode/electrolyte is set as zero ($x = 0$). Voltages are defined as: $V_0 = 0$, the voltage of the negative electrode which is set as a reference; V_1, the voltage on the electrolyte side of the negative electrode/electrolyte interface; V_2, the voltage on the electrolyte side of the positive electrode/electrolyte interface; and V_3, the voltage of the positive electrode.

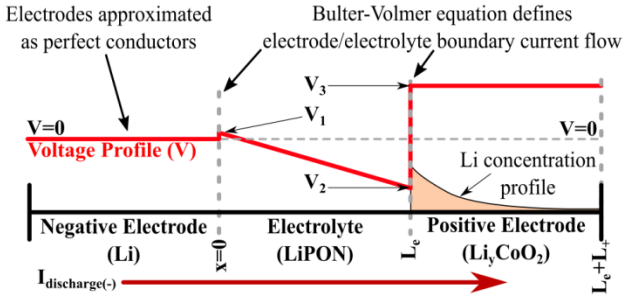

Figure 3.1 Battery schematic. A typical voltage profile for the model is shown on the coordinate system. A theoretical concentration profile for the positive electrode is shown also.

3.3.2 Electrochemical Model Equations

The model is based on current balance through the battery. Current flows through the electrode/electrolyte interfaces are expressed using the Butler-Volmer equation and are defined as follows: across the negative electrode/electrolyte interface ($x = 0$)

$$\frac{I}{A} = i_{0,-}\left(exp\left(\frac{\alpha_{a,-}F(V_0-V_1)}{RT}\right) - exp\left(-\frac{\alpha_{c,-}F(V_0-V_1)}{RT}\right)\right); \quad (3.1)$$

and across the electrolyte/positive electrode interface ($x = L_e$)

$$\frac{I}{A} = i_{0,+}\left(exp\left(\frac{\alpha_{a,+}F(V_3-V_2-U)}{RT}\right) - exp\left(\frac{-\alpha_{c,+}F(V_3-V_2-U)}{RT}\right)\right), \quad (3.2)$$

where I is the current, A is the cross sectional area, i_0 is the exchange current density with subscripts (+,-) indicating positive and negative electrodes respectively, α is the charge transfer coefficient with subscripts (a,c) denoting anodic and cathodic reactions at the given interface, F is Faraday's constant, R is the gas constant, T is temperature in Kelvin, and U is the open circuit potential (derived from a combination of experimental data and datasheet information[27]). Diffusion in the Li_yCoO_2 positive electrode is described as:

$$\frac{\partial c_+}{\partial t} = \frac{\partial}{\partial x}\left(D_+\left(\frac{c_+}{c_{+,max}}\right)\frac{\partial c_+}{\partial x}\right) \; at\; L_e < x < L_e + L_+ \quad (3.3)$$

$$D_+\left(\frac{c_+}{c_{+,max}}\right) = D_{+,0} \times D_{+,norm}\left(\frac{c_+}{c_{+,max}}\right) \quad (3.4)$$

with $c_+(x)$ the concentration in the positive electrode as a function of x, the subscript max denoting the maximum concentration, $D_{+,0}$ the nominal diffusion coefficient, $D_{+,norm}(c_+/c_{+,max})$ concentration dependent function of the normalized diffusion coefficient, and L_e and L_+ the thicknesses of the electrolyte and positive electrode respectively. Boundary conditions are given as:

$$\frac{\partial c_+}{\partial x} = 0 \; at\; x = L_e + L_+ \quad (3.5)$$

$$\frac{\partial c_+}{\partial x} = \frac{I}{AFD_+} \; at\; x = L_e \quad (3.6)$$

In Fabre et al. [14] the electrolyte concentration and conductivity are approximated as constant which is adequate for low current applications. We do the same, though for higher average current applications this would likely need to be revisited. The electrolyte resistance is defined as:

$$R_e = \frac{V_2-V_1}{I} \approx \frac{V_{Batt,Nom}L_e}{FD_{e,0}c_eA} \quad (3.7)$$

with $D_{0,e}$ the electrolyte diffusion coefficient, c_e the electrolyte Li concentration, and $V_{Batt,Nom}$ is the nominal battery voltage (taken as 4.1 V in this work). Equations 3.1-3.3 and 3.7, define the system of four equations and four unknowns (i.e. V_1, V_2, V_3, and c_+).

3.3.3 Cyclic Capacitive Load Modeling

Next, modeling is extended to account for effects of cyclic capacitive loading on thin film batteries, primarily through additional load dynamics. Previous solid-state battery analysis has focused primarily on other loading conditions such as constant current or voltage, with limited information on capacitive loads [24], so to better understand what additional phenomena are important to incorporate into a model with capacitive loading, initial experimental work was performed. A conceptual representation of this is shown in Figure 3.2.

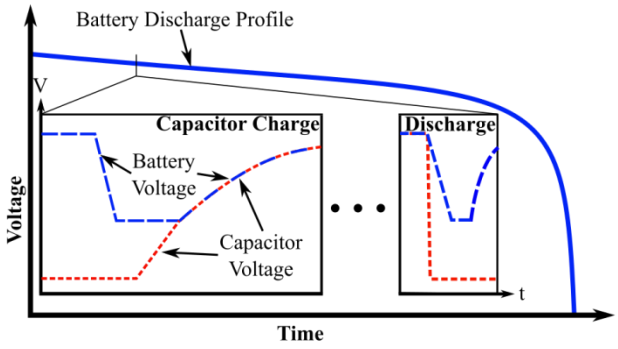

Figure 3.2 Battery discharge schematic. Switching dynamics have various timescales in these applications. The various switching times are represented in the subfigure.

Experimentally, a simple H-bridge switching circuit was used to cycle a 50μAh battery over various capacitive loads. The basic circuit schematic is shown in Figure 3.3. Details of experimental setup and findings were reported elsewhere demonstrating the importance of consideration of these losses [41] (see chapter 2). Key findings are summarized here.

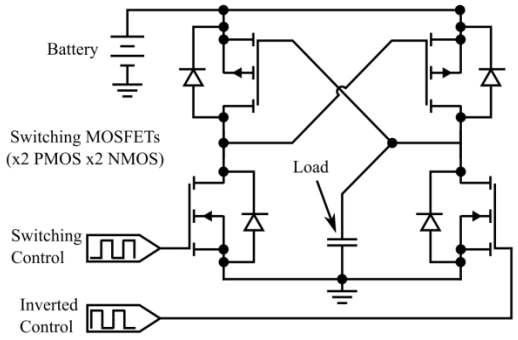

Figure 3.3 H-bridge switching circuitry for experimental testing. Reprinted with permission [41] (see chapter 2), and based on the circuit presented by others [64].

Timescale considerations: It is noted that timescales of the capacitor charging, battery dynamics, and switching characteristics can be very similar and therefore may all need to be addressed during individual cycle modeling (e.g. the battery cannot be assumed to be a perfect power source, and switching cannot be assumed to be instantaneous). Conversely, changes in system aspects such as open circuit potential and diffusion coefficient can occur over time scales that are orders-of-magnitude longer (minutes or hours vs. microseconds), which makes simulation over the full battery discharge challenging.

Switching and leakage losses: The switching circuit used to drive the capacitive load was not optimized and suffered from substantial losses; however, investigation of those losses was instructive, and necessary for comparison of modeling and experimental data. These losses included a short period where a limited path to ground was made during switching, while switching transistors were only partially charged. Additionally, it appeared that there continued to be transient switching losses at least until the switching was nearly completed. As in any transistor-based circuit, there was also a voltage dependent leakage current in the system. Frequency and size of capacitive loading influenced which type of loss was dominant.

Switching dynamics and timing: The timing of the switching phenomena was examined to provide an accurate load to the battery model. Switching charecteristics and approximate equivilent loading for capacitor charging (switch on) and discharging (switch off) are given in Figures 3.4 and 3.5. Again for more information on experimental setup and results see our prior work [41] (see chapter 2). The main switching events, common in many switching circuits, included the following (shown graphically in Figure 3.2):

1. Switching Initiated ($t_{switch} \leq t \leq t_{hold}$): This is characterized by a sharp drop in battery voltage as the H-bridge transistors are between equilibrium states creating a limited path to ground through the switching circuitry. Battery voltage drops to the threshold voltage dictated by the switching components (V_{th}). This timing was determined separately for on and off switching. For general applications, momentary connection to ground can be reduced or eliminated with more complex circuit design, though often with a tradeoff of greater complexity, larger leakage current, and/or slower response times. Switching circuit optimization was not the purpose of this work. For capacitor discharge, the load capacitor is considered disconnected from the battery and the voltage is removed.

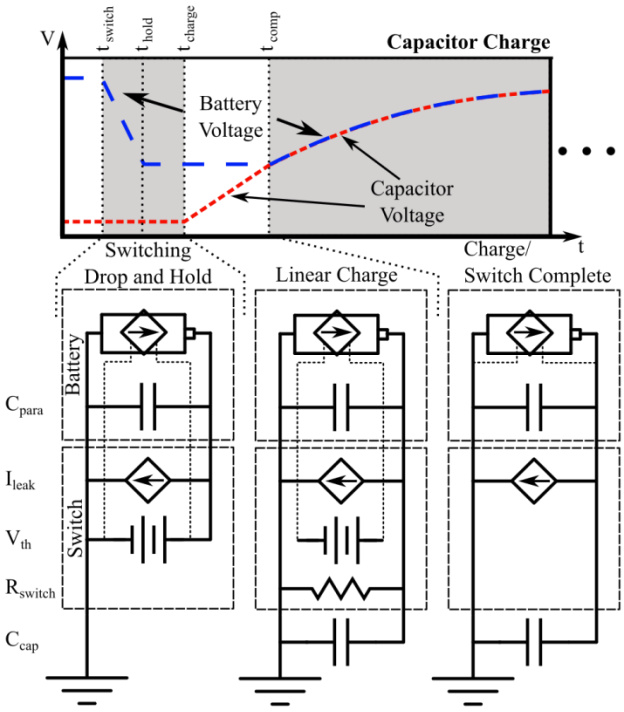

Figure 3.4 Switch timing characteristics and approximate equivalent loading for capacitor charging. The battery is represented as a voltage controlled current source with dotted lines representing the voltage signal.

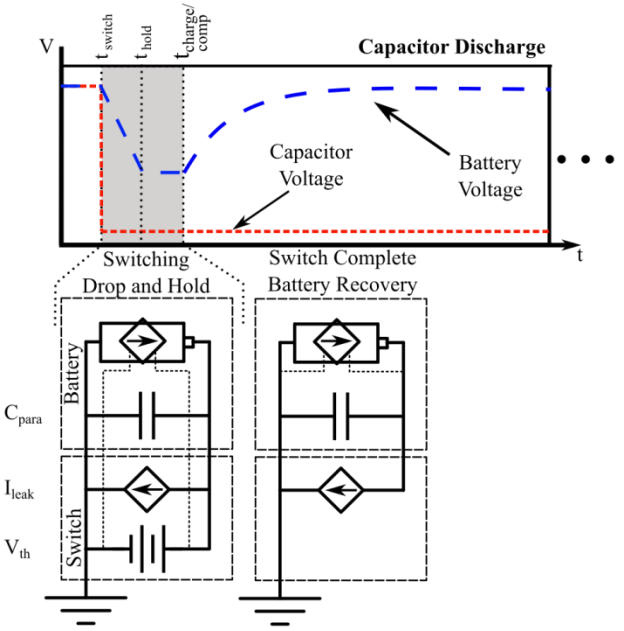

Figure 3.5 Switch timing characteristics and approximate equivalent loading for capacitor discharging. The battery is represented as a voltage controlled current source with dotted lines representing the voltage signal.

2. Switching Delay $(t_{hold} \leq t \leq t_{charge})$: There is then a short period of time before the capacitor begins to charge (switch on/capacitor charge) or the battery begins to recover (switch off/capacitor discharge) where there remains a limited path to ground through the

switch. During initial switching, a large current spike is observed leaving the battery system. This timing was determined separately for on and off switching.

3. Capacitor Linear Charging $\left(t_{charge} \leq t \leq t_{comp}\right)$: For switch on (capacitor charge) only, as the capacitor charges the battery is initially voltage limited by the switching transistors which causes a constant, or near constant, current into the capacitor. This current gives a nearly linear increase in the capacitor voltage that increases until the capacitor reaches the threshold.

4. Switching Complete $\left(t_{comp} \leq t\right)$: For switch on (capacitor charge), after the capacitor has reached the switching threshold voltage for the H-bridge transistors, the switching is considered completed and the battery and capacitor voltage increase in a somewhat exponential fashion, approximately as would an ideal voltage-resistor-capacitor system. For switch off (capacitor discharge), the battery does not need to supply current to the capacitor so after the switching delay the battery begins to recover immediately and the switching is considered completed.

Parasitic capacitance: Parasitic capacitance was manifested in several ways in the battery system. It was not determined if this was from the battery, or some other source (e.g. packaging or electrodes). This capacitance allowed for a small portion of the battery's charge to be stored in a quickly accessible format that was discharged to ground during the switching. This capacitance is in the range of the loads applied and has a substantial effect on charging dynamics.

During the capacitor charging mode of the cycle (switch on, battery discharging), loading on the battery includes switching effects, linear/exponential charging of the capacitor, and parasitic capacitor charging. Capacitive loading was applied to the model by dictating the battery voltage (i.e. capacitor voltage or threshold voltage) for short time steps, and calculating the battery response. At each time step in the model, the current available from the battery was determined based on the battery voltage, V_{Batt}, imposed by the load and the lithium concentration at the positive electrode/electrolyte interface. This current is a combination of current lost through leakage (I_{leak}) and switching (I_{switch}), as well as current into the load (I_{cap}) and parasitic capacitors (I_{para}),

$$I(t) = f\left(\frac{c_+}{c_{+,max}}, V_{Batt}(t)\right) = I_{leak} + I_{switch} + I_{cap} + I_{para}. \tag{3.8}$$

Losses related specifically to the switching events (primarily I_{switch}) were seen in two separate timeframes of the switching, and different modeling approaches were used for each of the two. The first part is for time $t_{switch} \leq t \leq t_{hold}$ during which the battery has a limited path to ground through the switch. The current out of the battery during this time at the given voltages is all lost to ground. During this time the parasitic capacitor tracks the battery voltage from the battery voltage at the time of switching, $V_{Batt}(t_{switch})$, to the switching threshold voltage, V_{th}, and that charge is considered lost to ground as well. The second switching loss period is $t_{hold} \leq t \leq t_{comp}$ (only applies to switch on/capacitor charge) where the battery is now charging the capacitor. These losses were approximated as a set resistance to ground, R_{switch}, in parallel with the load capacitor.

During capacitor discharge mode of the cycle (switch off, battery disconnected), we again see the switching effects, but only parasitic capacitor charging occurs as the battery recovers from the switch. All loading in the model can be described as an imposed voltage load on the battery. The battery voltage (V_{Batt}) corresponds to V_3 in Equation 3.2 and is equal to the voltage on the parasitic capacitor (V_{para}). As the battery recovers, its voltage is dictated by the charge on the parasitic and load capacitors. This dependence gives interplay between voltage and current. Loading is shown in Equations 3.9 and 3.10.

$$\begin{matrix} V_{Batt} \\ V_{para} \end{matrix} = \begin{cases} \text{For Switch } \mathbf{ON} \text{ and } \mathbf{OFF} & \\ V_{Batt}(t_{switch}) - \frac{t - t_{switch}}{t_{hold} - t_{switch}} (V_{Batt}(t_{switch}) - V_{th}), & t_{switch} \leq t \leq t_{hold} \\ V_{th}, & t_{hold} < t \leq t_{comp} \\ \text{For Switch } \mathbf{ON} \text{ only} & \\ V_{th} + \Delta V_{cap}\,, \quad t_{comp} < t & \\ \text{For Switch } \mathbf{OFF} \text{ only} & \\ V_{th} + \Delta V_{para}, \quad t_{comp} < t & \end{cases} \tag{3.9}$$

$$V_{Cap} = \begin{cases} \text{For Switch } \mathbf{ON} \text{ Only} & \\ 0, & t_{switch} \leq t \leq t_{charge} \\ \Delta V_{\text{cap,linear}}, & t_{charge} < t < t_{comp} \\ \Delta V_{\text{cap}}, & t_{comp} \leq t \\ \text{For Switch } \mathbf{OFF} \text{ Only} & \\ 0, \quad t_{switch} \leq t & \end{cases} \tag{3.10}$$

Here C_{cap} and C_{para} are the capacitances of the load and parasitic capacitors. The subscript "linear" refers to the portion of time when the capacitor charges at a near constant rate. The

dynamics of the capacitor voltage after it is switched off are not tracked, and approximated as no longer connected to the battery.

3.3.4 Nondimensional Model Parameters

This system has vastly different timescales and length scales. The timescales will be discussed later, but in both length and timescales there are several orders of magnitude variations (e.g. thickness of the electrode may be a few microns but surface area is on the order of a cm^2). In order to deal with some of these disparities the model was nondimensionalized (an example of electrochemical normalization can be found in Deshpande et al. [65]). This also allows us to consolidate parameters resulting in the final nondimensional parameters, π, and coefficients for non-dimensionalizing time and capacity, φ_1 and φ_2, as follows:

$$\varphi_1 = \frac{D_{+,0}}{L_+^2}\left[\frac{1}{s}\right] \tag{3.11}$$

$$\varphi_2 = \frac{2}{A\times F\times c_{+,max}\times L_+}\left[\frac{1}{As}\right] \tag{3.12}$$

$$\pi_1 = \alpha_{a,+}\ [] \tag{3.13}$$

$$\pi_2 = \frac{c_e}{c_{e,max}}\ [] \tag{3.14}$$

$$\pi_3 = \frac{D_{+,0}\times c_{+,max}\times L_e}{D_{e,0}\times c_{e,max}\times L_+}\ [] \tag{3.15}$$

$$\pi_4 = \left(\frac{2i_{0+,max}\times L_+}{F\times c_{+,max}\times D_{+,0}}\right)\left(\frac{c_e}{c_{e,max}}\right)^{-\alpha_{a,+}}\ [] \tag{3.16}$$

$$\pi_5 = \left(\frac{2i_{0-,max}\times L_+}{F\times c_{+,max}\times D_{+,0}}\right)\left(1-\frac{c_e}{c_{e,max}}\right)^{\alpha_{a,-}-1}\left(\frac{c_e}{c_{e,max}}\right)^{-\alpha_{a,-}}\ [] \tag{3.17}$$

$$\pi_6 = \frac{2C_{para}\times V_{Batt,Nom}}{F\times c_{+,max}\times A\times \mathrm{L}_+}\ [] \tag{3.18}$$

$$\pi_7 = \frac{2V_{Batt,Nom}\times L_+}{R_{switch}\times F\times c_{+,max}\times A\times D_{+,0}}\ []. \tag{3.19}$$

Equation 3.11 represents time normalization. Equation 3.12 represents the current normalization in the positive electrode. Equations 3.13-3.17 are parameters of the model connected with the electrolyte and/or the electrolyte/electrode interactions with $D_{\mathrm{e},0}$ the diffusion coefficient of the electrolyte and the subscript *max* for the exchange current density indicating

the maximum value. Equations 3.18 and 3.19 are parameters regarding the parasitic capacitance and the losses in the switching respectively with $V_{Batt,Nom}$ the nominal charged battery voltage (for this work 4.1V).

3.3.5 Numerical Implementation

Numerical implementation was done similar to Fabre et al. [14] using the Crank-Nicholson approach applied to the Lithium concentration profile in the $LiCoO_2$ (positive electrode) and optimization to balance currents. Initial Crank-Nicholson coding was based on methods presented by Spender and Ware [66], and adapted heavily for the current work. Care needed to be taken for the Neumann boundary conditions in our model. In particular, the large spikes in current cause significant changes in the concentration at the boundary between the positive electrode and the electrolyte. Because of these sharp gradients a very fine discretization was needed near the boundary; however, further in the positive electrode a much coarser grid was adequate. To accommodate the boundary and yet save on computational expense a non-uniform mesh was used. This was implemented based on the equations in the appendix of Bowen and Smith [67]. Time discretization was also varied to capture the areas of faster dynamics with greater accuracy.

3.3.6 Parameter Fitting

Parameter fitting was implemented to correlate the non-dimensional parameters with corresponding experimental data. Fitting was performed using a combination of two types of data: a suite of constant current tests and a single charge/discharge cycle of a capacitor (with validation over a full battery discharge). Using these two data sets it was anticipated that we could fit the fast and slow dynamics of the battery model. The switching fit was performed primarily around the area of large dynamic changes. Errors in fitting were determined from differences in the voltages, timing, and capacity loss (single cycle), of model and experimental data.

Weighting of different aspects of the calibration process was chosen. A variety of different optimization steps were used to target specific parameters. Changes in the concentration dependence of the diffusion coefficient were added in the latter parts of the calibration. Weighting was chosen with primary priority on switch timing and the voltage before each switch. This voltage is key in that it describes the charge transferred to the capacitor, which is

one of the most accurately known variables experimentally. The shape of the capacitor charge was generally given lower priority in the weighting. This was done in part because of the higher-order dynamics that seemed to be at play beyond the fitting capabilities of the model that limit the possible fit. It is not anticipated that a significantly better fit of the capacitor charging profile could be obtained with changing weighting. Low weighting was also given to the highest current of the constant current set because model assumptions break down at high currents, while higher weighting was often given to the lowest current run.

Multiple iterations of a direct search method with an adaptive mesh (patternsearch function in MATLAB®) were used to perform the optimization. In addition to these parameter fits, certain characteristics of the variable diffusion coefficient were also fit to allow the model to mimic in part the concentration dependency of the diffusion coefficient that is described in Fabre et al. [14] Switching parameter times were determined from averaging experimental data.

3.3.7 Full Battery Discharge Modeling

Modeling effects of many cycles of the load is important in understanding full battery responses and implications of the loading for desired applications. However, analyzing the load effects over time can be challenging due to the differences in timescale. In order to demonstrate our model's use at various stages of the battery discharge we implemented a transition matrix projection approach. There may be other approaches that could also be used, such as the method of multiple scales.

The projection approach developed was as follows. Let the dimensionless Lithium concentration in the positive electrode be discretized in time and space as:

$$\frac{c_+(x,t)}{c_{+,max}} = y(x,t) \rightarrow y(m,n) \equiv y_n^m \tag{3.20}$$

where, *k,* is the spatial grid point, and *n* is the cycle number. The full profile vector after a given cycle noted as $\bar{y}_n$. It is then possible to describe the battery in terms of the concentration profile changes from cycle to cycle.

$$\bar{y}_{n+1} = f(\bar{y}_n) \tag{3.21}$$

where *f* is a function representing the battery dynamics for a given set of parameters such as capacitor load size, cycle frequency, etc. If *f* is approximated as a linear function near the current operating point then delta change in concentration per cycle, $\Delta\bar{y}_{n+1}$, can be written as:

$$\Delta\bar{y}_{n+1} \equiv \bar{y}_{n+1} - \bar{y}_n = f(\bar{y}_n) - f(\bar{y}_{n-1}) = g(\Delta\bar{y}_n) \approx \boldsymbol{T}\Delta\bar{y}_n \tag{3.22}$$

The matrix $\boldsymbol{T}$ is a linearized transition matrix for the delta change in concentration profile of the positive electrode during cycle *n* to the delta change in concentration during cycle *n*+1. That is, we take the delta change in concentration profile, $\Delta\bar{y}_n$, as the states of the system for a given cycle. We determined $\boldsymbol{T}$ using a perturbation method on $\Delta\bar{y}_n$. By perturbing each grid point by some δ^m, we can determine the change to every other grid point, ε_m^i, where *m* denotes the grid point being perturbed, and *i* indicates the affected grid point:

$$g\left(\begin{bmatrix} \Delta y_n^1 \\ \Delta y_n^2 \\ \vdots \\ \Delta y_n^m + \delta^m \\ \vdots \\ \Delta y_n^k \end{bmatrix}\right) = \begin{bmatrix} \Delta y_{n+1}^1 + \varepsilon_m^1 \\ \Delta y_{n+1}^2 + \varepsilon_m^2 \\ \vdots \\ \Delta y_{n+1}^m + \varepsilon_m^m \\ \vdots \\ \Delta y_{n+1}^k + \varepsilon_m^k \end{bmatrix} \tag{3.23}$$

Assuming a constant $\delta^m = \delta$, we can construct the transition matrix:

$$\boldsymbol{T} = \begin{bmatrix} T_1^1 & T_2^1 & \cdots & T_k^1 \\ T_1^2 & T_2^2 & \cdots & T_k^2 \\ \vdots & \vdots & \ddots & \vdots \\ T_1^k & T_2^k & \cdots & T_k^k \end{bmatrix} = \delta \begin{bmatrix} \varepsilon_1^1 & \varepsilon_2^1 & \cdots & \varepsilon_k^1 \\ \varepsilon_1^2 & \varepsilon_2^2 & \cdots & \varepsilon_k^2 \\ \vdots & \vdots & \ddots & \vdots \\ \varepsilon_1^k & \varepsilon_2^k & \cdots & \varepsilon_k^k \end{bmatrix}. \tag{3.24}$$

One further numerical challenge of the electrochemical system noted earlier is that it is naturally sequential where the solution for the first step must be solved in order to determine the next step. Because of this, we can take little advantage of parallel computing. Determining the transition matrix in the manner presented here allows some of the computation (the perturbed cycles) to be performed in parallel with ongoing simulation cycles, reducing the sequential numerical burden.

The transition matrix, $\boldsymbol{T}$, allows us to now project forward the system states, $\Delta\bar{y}_n$, p cycles into the future, which can be used to determine the concentration profile as:

$$\bar{y}_{n+p} = \bar{y}_n + \sum_{j=1}^{p} \boldsymbol{T}^{j-1}\Delta\bar{y}_n. \tag{3.25}$$

It is important to remember that this assumes a linear system. However, this problem has a number of nonlinear aspects (e.g. the OCV, electrochemical equations, and variable diffusion coefficient). These nonlinearities introduce error that generally increases with projection length (i.e., the number of cycles projected using a fixed transition matrix approximation). An approach

used in this work to reduce this error was to update the transition matrix before each projection. A flowchart of the model and projection process are given in Figure 3.6.

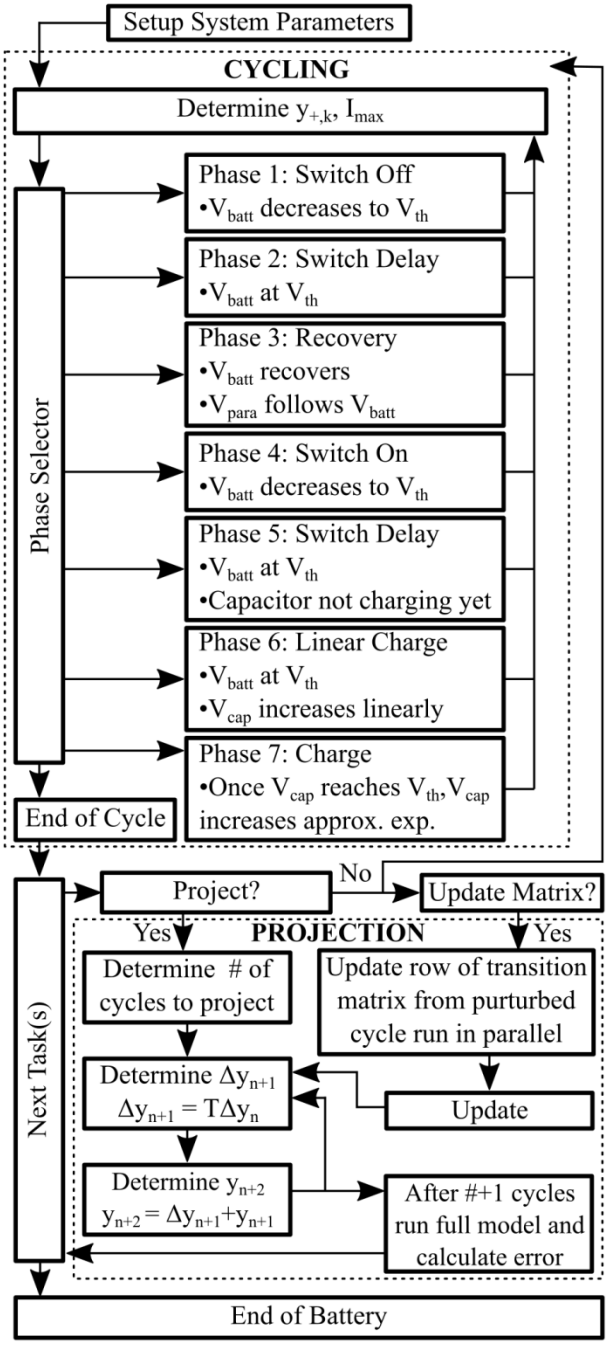

Figure 3.6 Flowchart of cyclic model and projection approach.

3.4 Results

3.4.1 Experimental Data

Three sets of experimental data were used, two for calibration and parameter fitting, and the other for model validation. The first set of calibration data consisted of five different constant current tests including 5μA (0.1C), 20μA (0.4C), 50μA (1C), 200μA (4C), and 500μA (10C). This constant current data was gathered using a Labview setup with the current regulated by a Keithley sourcemeter. Losses and other effects were not considered when collecting this data.

Switching data was also acquired where a 10nF capacitor was cycled at 100Hz. Experimental setup and limitations are reported elsewhere [41] (see chapter 2). The main limitations in the data included accuracy in the current data and conversion from AC probe readings to DC values, as well as noise and other extraneous effects in the current and voltage measurements. Two sets of switching tests were used. The first was used for calibration, and only measurements from a single cycle near the beginning of battery discharge were used. The second was used for validation of the model, using the full battery discharge data.

When converting these datasets to overall battery capacities, the constant current data was significantly different from the values published in the vendor literature compared to that of the switching data. This could be in part due to the differences in setup, or assumptions, or variations between tests due to battery/run variations. To correlate the data for model validation purposes, the constant current data was scaled using an interpolated capacity of the average current for the switching data (15μA). Therefore the data presented here is used primarily for model approach validation, and is not necessarily representative of general capabilities of the specific battery type that was used.

All experimental runs charged the battery to ~4.1V and discharged until ~3.3V. These voltages in the open circuit potential were approximated as being 0.5 and 1.0 values of the normalized lithium concentration in the positive electrode.

3.4.2 Parameter Fitting/Calibration

Parameter fitting was used to extract φ_1-φ_2 and π_1-π_7 in Equations 3.11-3.19 and select points defining the concentration dependent diffusion coefficient. As noted one cycle of a 10nF capacitor at 100Hz was used in connection with the constant current data. The area of the battery was approximated based on the die size. Switch drop and hold times as well as threshold voltage

were averaged from experimental data (but could be taken from a single data set), and are constant throughout the full model.

The final parameter fitting results are given in Figures 3.7-3.9 and Table 3.2. Figure 3.9 shows the points defining the diffusion coefficient and the degrees of freedom associated in the optimization.

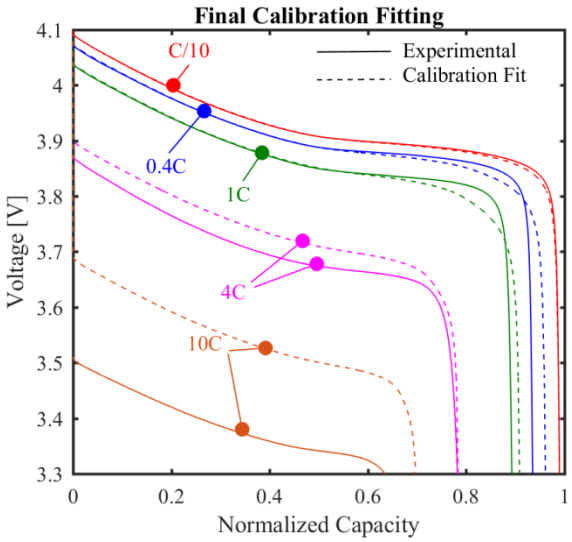

Figure 3.7 Constant current profiles and calibrated fits.

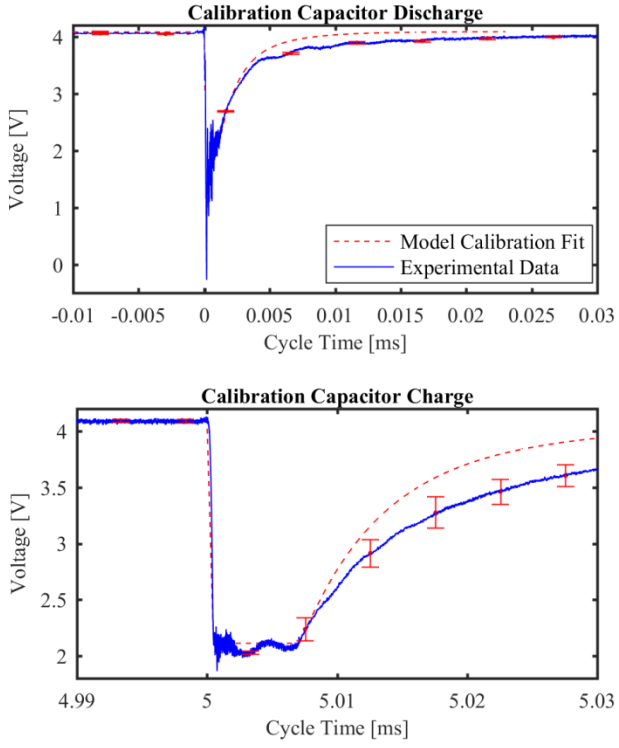

Figure 3.8 Switching profile data and calibrated fit. Error bars are based on rolling average and discrepancies between battery and capacitor voltage measurements.

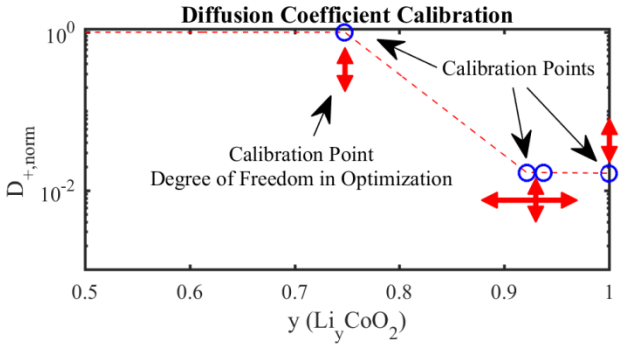

Figure 3.9 Normalized diffusion coefficient calibration. The blue circles in the profile represent points that were allowed to vary within certain limits. The red arrows show the degrees of freedom. The center two points always had the same diffusion coefficient value.

Table 3.3 shows physical parameter values based on the nondimensionalized parameters and two assumed parameter values. The fitting of the constant current discharge is very close, with the exception of the highest current profile which had low priority in the calibration process. This lack of fit is expected in part due to the assumption of constant electrolyte conductivity, which assumption may need to be addressed if loadings are used that create currents consistently higher than seen in the switching tests presented here.

Table 3.2 Calibration parameters. References are for one or more of the parameters in the equation.

Optimized Parameter	Initial Value	Final Value	Ref Value Included in Parameter	Corresponds to:
$\varphi_1[1/s]$	4.54e-2	5.24e-2	$D_{0,+} = 0.2$ [$\mu m^2/s$] [14]	Time
φ_2 [1/mAs]	5.78e-3	4.17e-3	$c_{+,max} = 5 \times 10^{-14}$[mol/$\mu m^3$] [14]	Positive electrode current and capacity
π_1 [-]	0.500	0.525		Electrolyte or electrode/electrolyte boundary
π_2 [-]	0.180	0.191	$c_e = 10.818 \times 10^{-15}$[mol/$\mu m^3$] $c_{e,max} = 6 \times 10^{-14}$[mol/$\mu m^3$]*[15]	
π_3 [-]	0.285	0.285	$D_e = 6 \times 10^{-3}$[$\mu m^2/s$] Based on* [15]	
π_4 [-]	9.03e-2	1.68e-2	$i_{0+,max} = 4.4 \times 10^{-9}$[mA/$\mu m^2$] [14]	
π_5 [-]	0.167	0.281	$i_{0-,max} = 1.5 \times 10^{-8}$[mA/$\mu m^2$] [14]	
π_6 [-]	5.98e-8	6.03e-8		Parasitic capacitance
π_7 [-]	6.09e-2	7.10e-2		Switching loss
Averaged Parameter	Value		Description	
V_{th}	2.112 [V]		Switching threshold voltage	
$t_{drop,on}$	0.124 [µs]		Battery voltage drop time, switch on ($t_{switch} - t_{hold}$)	
$t_{delay,on}$	1.004 [µs]		Switch delay time, switch on ($t_{hold} - t_{charge}$)	
$t_{drop,off}$	0.521 [µs]		Battery voltage drop time, switch off ($t_{switch} - t_{hold}$)	
$t_{delay,off}$	0.069 [µs]		Switch delay time, switch on ($t_{hold} - t_{comp}$)	
Additional Parameter				
$V_{Batt,Nom}$	4.1 [V]		Nominal charged battery voltage	
*Electrolyte parameters initial values were based on LiPO information. [15] Thicknesses used in Initial values were approximated as $2.5\mu m$ for the positive electrode and $10\mu m$ for the electrolyte.				

Table 3.3 Calculated parameters. Physical parameters were calculated from the calibration parameters based on two assumed values as noted.

Assumed Parameter	Value
$c_{+,max}$	$5 \times 10^{-14}[mol/\mu m^3]$
$\alpha_{a,-}$	0.5
Calculated Parameter	Value
$D_{0,+}$	$0.428\ [\mu m^2/s]$
L_+	$2.86\ [\mu m]$
$i_{0+,max}$	$2.5 \times 10^{-9}[mA/\mu m^2]$
$i_{0-,max}$	$2.1 \times 10^{-8}[mA/\mu m^2]$
R_e	$243[\Omega]$
C_{para}	$3.53\ [nF]$
R_{switch}	$4.60\ [k\Omega]$

In the switching fits, it appears that there are higher order dynamics that slow down the charging of the capacitor that are not fully captured by the model. This potentially could be from the switching circuitry as there could still be residual losses from incomplete switching past the time that the battery and capacitor voltages meet. In spite of this, the fast dynamics of the switching are able to be reasonably captured with the model and parameters implemented through the majority of the battery discharge as will be discussed later with validation. Some of the starting parameters for the calibration optimization are based off of LiPO instead of LiPON. It is understood that these will have different properties, but for a starting point for the fitting optimization it was considered adequate. This fitting approach allows for parameter determination using very little high-sample-rate data by being able to base the fit on only one on/off cycle of the capacitor. The majority of the fitting data comes from the coarsely sampled constant current profile that is much easier to attain.

It should be noted that the fitting of the parameters proved to be heavily influenced by the starting point and optimization approach. Precision experimental data and/or an improved calibration approach would be beneficial for more targeted future parameter fitting.

3.4.3 Validation Modeling Results

Using the parameters determined in calibration, a full battery discharge was modeled, with a cyclic discharge at 100Hz over a 10nF capacitor. This validation data set was a separate test run from that used for model fitting and a portion of the capacitor charge of each measured cycle is shown in Figure 3.10. The discharge profiles are presented to show the changes in cycle profile

over the full battery discharge. The experimental data is adjusted so that the switching of the model and each cycle align. Aspects of the switching were incorporated into the model as described. The inputs to the model include the calibration data (parameters, switching times, and threshold voltage), as well as the initial voltage of the validation data set.

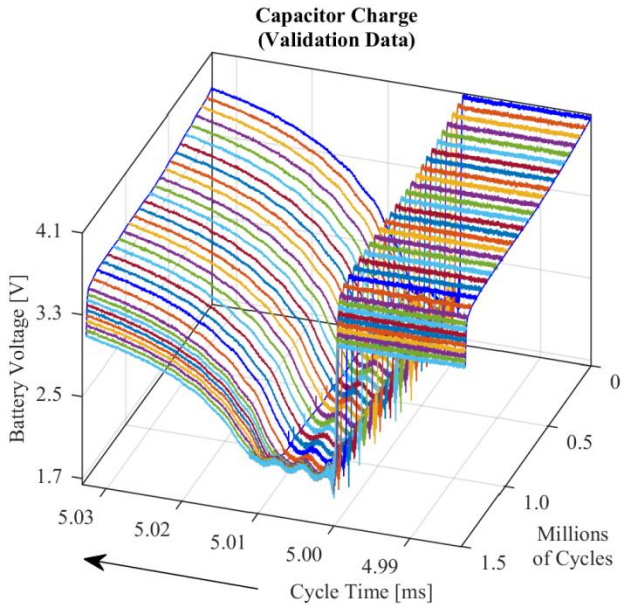

Figure 3.10 Capacitor charge section of the validation data. The battery voltage profile for each measured cycle is shown. Each cycle is aligned to correlate switching times for the model and each cycle. Only capacitor charge data is shown and voltage error bars are omitted.

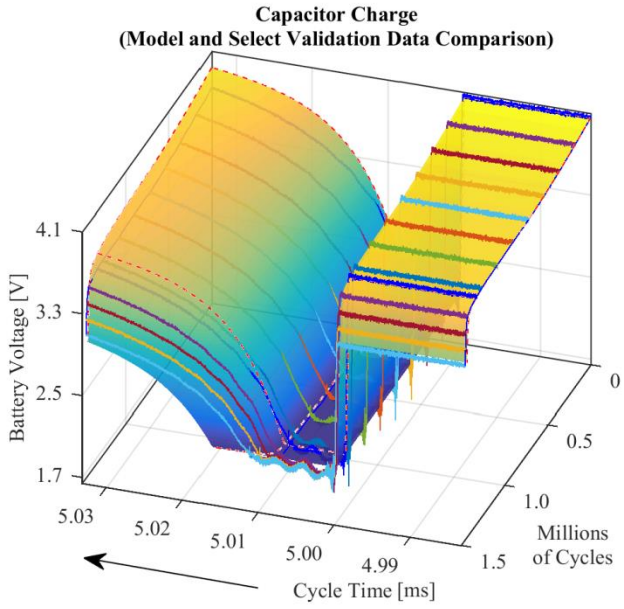

Figure 3.11 Model/select validation data comparison. The model shows a slightly faster charge of the capacitor than the experimental data, however, the final voltages are very similar. The overall battery life also shows good correlation in this scenario. Voltage error bars are omitted on experimental data.

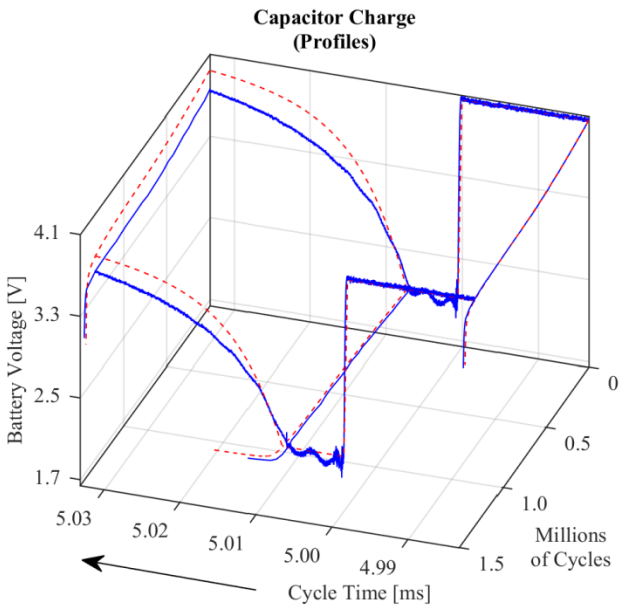

Figure 3.12 The profiles of the model/select validation data comparison are shown. The fit shows that fast and slow dynamics of the battery are represented by the model. Voltage error bars are omitted.

This is the voltage of the battery, including any effects of leakage current. Because of leakage current in the measurement, the initial concentration is not exactly known but rather is estimated from the voltage with the applied leakage current.

A comparison of the model and validation data current profiles was also performed. However, due to limitations in the experimental current data measurement [41] (see chapter 2), comparison of the model current profile and validation data current are used only for reference and are shown in Figure 3.13. The figure shows the losses in switching and the charge transfer to the capacitor, and indicates some of the limitations of the model. It is important to note that in Figure 3.13 the leakage current is small enough to not be discernable in the plot, and parasitic capacitor current is based for plotting purposes on the change in battery voltage.

In the full battery discharge model, 300 initial cycles were run before the first projection. Additionally, a certain number of cycles were allowed after each projection to allow the model to settle before beginning updating the transition matrix. The number of cycles to project was determined on a tradeoff between projection size and error. A few additional cycles were used before each projection to determine an appropriate projection/error. The full battery discharge model data shows reasonable agreement with the experimental data. Figure 3.14 shows a comparison between the experimental and modeled discharge based on the number of cycles performed. Concentration profiles for the full discharge of the battery are shown in Figure 3.15.

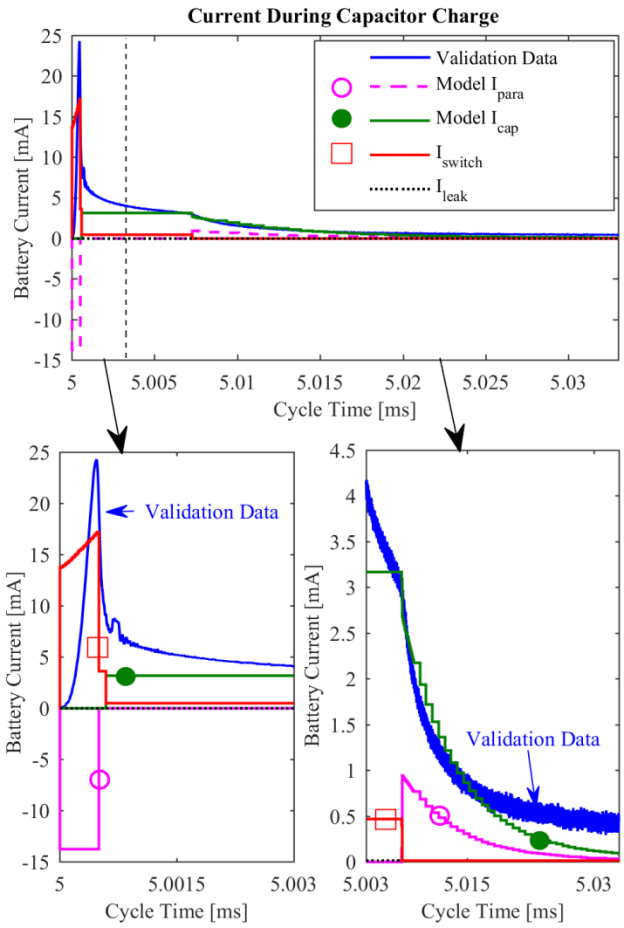

Figure 3.13 Current comparison. The initial part of capacitor charging is shown comparing the validation current[19] and the different components of the model current. Leakage current is small compared to other currents. The large current spike is due to the discharge of the parasitic capacitor. Circle and square symbols are to distinguish different profiles. (Lower) Detailed split view with different scales.

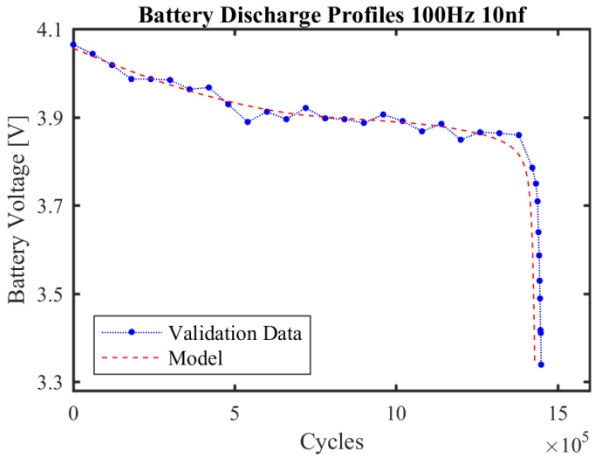

Figure 3.14 Discharge profiles. The discharge profiles of voltage just before capacitor charge are shown for the model and validation datasets.

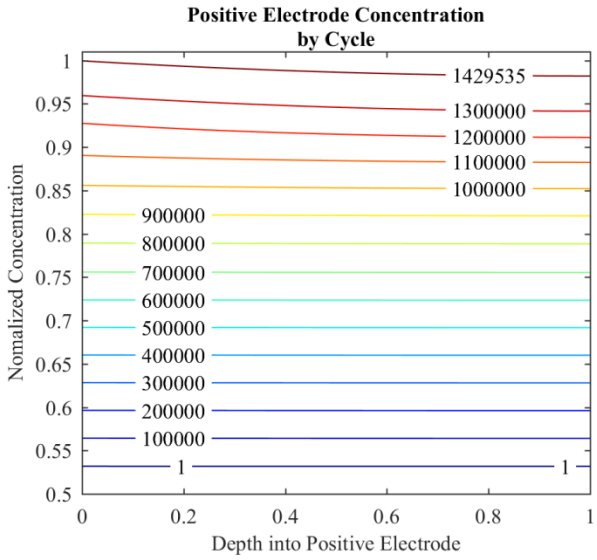

Figure 3.15 Positive electrode concentration profile by cycle. Normalized concentration profiles for the positive electrode over the full discharge of the battery. Labels indicate cycle number.

The small changes in slope of the concentration at the early cycles may indicate that the diffusion did not play a large role. This is assumed in part to be why large projections during this portion were possible.

A significant computational decrease was able to be achieved using this projection approximation. One measure of this reduction is the ratio of cycles fully modeled to the total number of cycles (including projected cycles). The modeled cycles do not include cycles that were performed in parallel (updating the transition matrix, and some trial projections), and certain assumptions were made for other overhead costs. The overall approximate Full Modeled Cycles/All Cycles ratio was to 0.19% after ~0.677 million cycles, and 6% after nearly 1.43 million cycles, which is nearing the end of the battery discharge. Calculations are based on use of a quad core computer for processing. This numerical cost is based heavily on the equipment and projection/error algorithm. For example, if more cores were available for processing the transition matrix could be updated more quickly, or if more error was allowed larger projections could be made, both of which would reduce the numerical cost. Additionally, other approaches to numerical reduction are possible. For example, it may be possible to do a hybrid constant equivalent current projection (which would likely have greater success where the battery is able to recover between switching events like in this work); however, the proposed approach allows us to determine a benchmark for future work in full battery discharge modeling. Ultimately the

projection is useful here to enable us to see the evolution of the modeled cycle profile over the battery discharge and validate the cyclic capacitive discharge model.

3.5 Conclusion

Cyclic capacitive loading of solid-state batteries in the mid-frequency range are of importance in areas such as MEMS. Here we review the fundamental electrochemical equations that define this type of system and the basic model presented by Fabre et al. [14] and Danilov et al. [15], and the phenomena discussed in our previous work [41] (see chapter 2). The underlying battery model was found to be suitable for capturing fast dynamics of individual charge cycles with some parameter adjustment, provided that all aspects of switching losses and parasitic loads were assessed/incorporated. We provide and demonstrated a hybrid parameter fitting framework where limited cyclic data can be used in connection with full discharges at constant current to capture fast and slow dynamics of the system. We developed and demonstrated a projection approach that can capture cyclic data from a limited number of cycles and project that over many cycles to significantly reduce the computational expense of fully modeling these systems. Finally, we implement these into a full battery cyclic model. We were able to show changes in cycle profiles over time with reasonable fitting of the battery discharge. Further work can be done to look at a broader set of loading conditions (capacitance and frequency, particularly higher average currents where the battery is not able to settle as much during cycling), as well as understanding the limitations of and improving the projection approach described here. Overall this work highlights the issues with cyclic capacitive loads, provides a modeling approach to describe these systems, and a projection approach allowing tracking of the cyclic profile over a battery discharge at reduced numerical cost.

CHAPTER 4 MODEL IMPROVEMENTS AND ERROR ANALYSIS[3]

4.1 Abstract

Simulating repeating loading events on dynamic systems can be challenging when large timescale disparities exist coupled with aperiodic effects. Batteries driving switched/pulsed loads represent one such situation. Large timescale disparity can be experienced by solid-state batteries driving switching microactuators or microelectronics, due to extremely short transient response times of microscale systems relative to some of the battery's own dynamics. Projecting state changes over a long series of fast-timescale loading events using a transition matrix approach was shown previously to significantly reduce numerical expense of simulation compared to full modeling. Here we develop an approach for further accelerated simulation of a battery driving a microelectromechanical system (MEMS) actuator that quantifies errors and addresses overhead expenses in projecting battery states across multiple fast events. This is done with a definition of system states that allows efficient transition matrix generation, and an analysis of key errors associated with projection. This error analysis enables targeted modification to the transition matrix during projection. A case study explores these modeling approaches in a capacitively loaded, battery usage scenario of a piezoelectrically-driven microrobot where the proposed improvements reduce the numerical cost (function calls) by over 44x from the prior approach. Conditions for further simplified modeling are discussed.

4.2 Introduction

Thin-film solid-state batteries provide a convenient power source for many small engineered systems, particularly microsystems based on integrated circuit and micro-electromechanical system (MEMS) technologies. In many such systems, battery loading occurs as repeated short-duration transient events, such as to drive microactuators or switching electronics in periodic operation. Individual loading events may occur over time periods of just a few microseconds, given the high bandwidths of associated electrical or electromechanical components, while

[3]A version of this chapter is submitted to "the Journal of Energy Storage" for review.

complete battery discharge may occur over several hours. This vast disparity in timescales can make high-fidelity simulation of battery behavior based on physics-based partial differential equation models, very challenging. Nonetheless, such simulation can be beneficial for understanding influences of system-level design choices (i.e. loading frequency and component sizes) on anticipated battery performance or assessing the accuracy of simplified reduced-order or equivalent circuit battery models. This paper thus proposes a strategy for efficiently simulating repeated transient loading effects on a solid-state battery model using a numerically-identified state-transition matrix approach, and illustrates how error analysis of the numerical method can be used to further improve simulation efficiency and/or accuracy.

In general, modeling of power/battery systems can be an important tool for improving design and control, and has been performed in a variety of ways including electrochemical [14-16] and equivalent circuit modeling [32, 52]. Different approaches for model reduction have also been attempted to make the system easier to handle. For example, Santhanagopalan et al. [30] compares model reduction strategies for lithium-ion batteries with porous electrodes, for full discharge cycling; Kim and Qiao [31] present a hybrid model that combines simplicity with nonlinear effects with demonstration on a limited number of pulses during discharge; and Afshar et al. [33] uses a reduction method to address the boundary conditions transforming them to differential equations through linearization.

In microscale applications, it is also important to understand the usage of battery capacity due to the limited payload and footprint available. The effects of intermittent loading on different types of batteries have been discussed in the literature with varying opinions [20-22]. Additionally, from a computational perspective, merely modeling the individual loading event dynamics can be numerically expensive. Fully modeling this problem, when coupled with the many loading events (potentially millions), can be impractical.

One example of intermittent battery loading for MEMS devices, to be the focus of the case study in this paper, is that of switched piezoelectric or electrostatic MEMS actuation, both of which act as capacitive loads in terms of electrical behavior. This type of loading, especially when coupled with power electronics' dynamics, can have effects on multiple timescales as is shown in the conceptual schematics of a microrobot in Figure 4.1 based on work in [34]. The authors have previously shown experimentally that useful battery lifetime when driving a capacitive load can have complex dependence on details of switching frequency, load

capacitance, and various circuit current and switching losses [41] (see chapter 2). From a modeling perspective, the authors have also shown that resulting battery behavior can be captured through adaptation of existing thin-film electrochemical models [14, 15] through inclusion of additional switching and loading effects [42] (see chapter 3). However, the accumulation of repeated individual loads created a dual-timescale problem when analyzing battery behavior over a complete discharge. In the earlier work, this was addressed by systematically perturbing system states, or changes in Li concentration at discretized points. In that manner, a numerical Jacobian or "transition matrix" could be developed describing changes in the system states over one fast-dynamic event. That transition matrix then could be used to approximate (or "project" over) multiple fast-dynamic events. This permitted simulation of battery discharge to be greatly accelerated, but simulation remained extremely computationally expensive and dependent on available hardware for parallelizing transition matrix development due to the large number of perturbations required. Furthermore, sources of accumulated error between the full model and accelerated simulation were not readily identifiable.

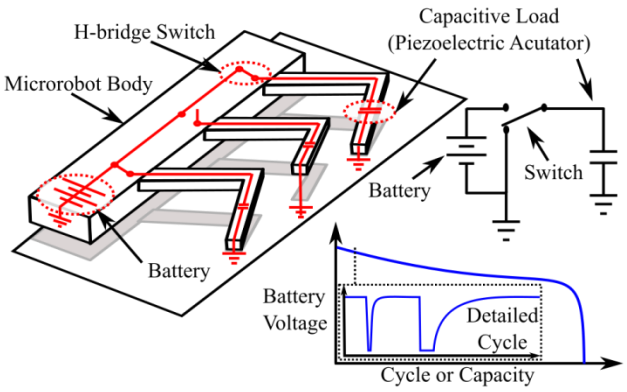

Figure 4.1 MEMS micro-robot [34] switching and actuation schematics. A micro-robot schematic with a simplified equivalent circuit overlaid in red on the robot body is shown. A simplistic battery switching schematic, with an H-bridge (represented schematically as a simple single-pole double-throw switch) is shown, and similar simplistic switching was used in the case study here. A sample battery discharge profile is shown with a representative single capacitor charge cycle profile.

From a numerical methods perspective, the modeling and simulation of systems with disparate timescales is known to be challenging. Nonetheless, different approaches can be used depending on the specifics of the problem being analyzed. Engstler and Lubich presented an extrapolation approach where aspects of the problem are inactivated during portions of the extrapolation to reduce computation [25]. Constantinescu and Sandu extended this for "extrapolated explicit and implicit compound multirate steps" [26]. Roychowdhury discusses analysis of multiple time scale circuits by using different time variables [27]. Edwards shows an

example approach with a heat conduction problem of two timescales [28]. A broad discussion on the topic of multiple timescales is given in [29].

Due to several features common to electrochemical battery modeling, the implementation approach of these traditional multi-scale methods may not be directly applicable. These aspects include: variable coefficients (seen in the concentration dependency of the diffusion coefficient), multiple timescale boundaries (slow evolving open circuit potential and fast switching dynamics), Neumann-type boundaries (positive electrode concentration), non-linear algebraic constraint of the boundary (exponential form of the Butler-Volmer equations), and the fact that the slow dynamics are produced due to accumulation of repeated fast dynamic events. While this does not preclude the possibility of adapting the above methods to the thin-film battery simulation problem examined here, this paper focuses on transition matrix methods as introduced above.

Here, we propose the use of intrinsic dynamics and numerical error analysis to model thin-film solid-state battery behavior over repeated fast timescale loading events in a computationally efficient form. First, we review the basic electrochemical battery model applied in previous work. Then, we describe how to directly compute a transition matrix for states of the discretized electrochemical model over fast timescale events using lithium concentration as the states of a dynamic system. This substantially reduces overhead in identifying the transition matrix relative to past work. Next, further understanding/improvement of projection of system states is achieved through an error analysis performed to decouple sources of error caused by approximations of various nonlinear phenomena that influence the state projections. In combination with knowledge of the expense of reducing certain error contributions, this allows for targeted error reduction. Finally, we demonstrate implementation of these modeling approaches in a case study looking at cyclic capacitive loading of a thin-film battery, arranged to mimic effects that might be seen in a microrobotic application [34, 36, 64]. The implementation of these modeling techniques is able to provide over a 44x reduction in function calls compared to our original approach [42] (see chapter 3) and a 99.96% computational reduction over a full simulation of the battery discharge, with additional savings possible with more aggressive updating and/or optimized time-stepping.

4.3 Modeling Approach

4.3.1 Modeling Nomenclature

Three main approaches to accelerated simulation of battery discharge are discussed in this paper, and will be referred to as follows. The approach from our prior work [42] (see chapter 3) that was based on perturbation of states, where the states were defined as changes in concentration, will be denoted as the "perturbed state approach." The current work develops a transition matrix that is developed directly from a modeled load and will be denoted as the "direct transition matrix approach." Additional improvements are made by targeted updates based on information gathered from the error analysis and this approach will be denoted as the "updating transition matrix approach."

In our prior work [42] (see chapter 3) we referred to the proposed type of loading as "cyclic capacitive" where "cyclic" refers to the repeated switching of a load (e.g. load on/load off), and "capacitive" refers to a load that behaves similar to an electrical capacitor. In common battery terminology "cycles" or "cyclic" generally refers to the full battery charge and discharge, additionally capacity and capacitance are easily confused. To avoid confusion, in this paper we will denote a single capacitive loading period (the actuator, represented by a capacitor, is charged and then discharged from the battery) as a "cap-cycle."

4.3.2 Modeling Background

The foundation of our modeling approach is based on a one-dimensional electrochemical model of a thin-film battery presented in Fabre et al. [14] and others [15, 16]. This was augmented based on the authors' findings in [41] (see chapter 2) to accommodate repeated cap-cycles [42] (see chapter 3). A brief overview of the electrochemical equations will be given here. For a more through development, approximations, and assumptions, see the prior works [14-16, 42] (see chapter 3). The essence of the electrochemical model is a combination of the diffusion equation and boundary conditions describing the Li in the positive electrode, and a current balance through the battery based on the Butler-Volmer equation describing voltage changes at the electrolyte boundaries and Ohm's law describing the voltage drop across the electrolyte. This formulation is a partial differential equation (PDE) with Neumann boundary conditions, where one of those boundary condition is coupled algebraically to the voltage changes in the battery.

The equations were nondimensionalized as noted in [42] (see chapter 3). This gives us a nondimensional diffusion equation and boundary conditions for the positive electrode:

$$\frac{\partial \mathbb{Y}_+}{\partial \mathbb{T}} = \frac{\partial}{\partial \mathbb{X}}\left(\mathbb{D}(\mathbb{Y}_+)\frac{\partial \mathbb{Y}_+}{\partial \mathbb{X}}\right) \tag{4.1}$$

$$\frac{\partial \mathbb{Y}_+}{\partial \mathbb{X}} = f_1(\mathbb{I})|\mathbb{X} = 0 \tag{4.2}$$

$$\frac{\partial \mathbb{Y}_+}{\partial \mathbb{X}} = 0|\mathbb{X} = 1 \tag{4.3}$$

where the double struck charterers (e.g. $\mathbb{Y}_+$) symbolize a normalization or nondimensionalized value: $\mathbb{T}$ is time, $\mathbb{Y}_+$ is the concentration in the positive electrode, $\mathbb{X}$ is the spatial variable in the positive electrode, $\mathbb{D}(\mathbb{Y}_+)$ is the concentration-dependent diffusion coefficient in the positive electrode, and $\mathbb{I}$ is current which in part describes the positive electrode/electrolyte Neumann boundary condition. This current at the boundary needs to be balanced with the current through other parts of the battery using the Butler-Volmer equation which relates current and potential changes within the battery (electrode/electrolyte interfaces):

$$\mathbb{I} = f(\mathbb{Y}_e, \mathbb{Y}_+)\left[-\exp\left((\alpha_{a+} - 1) \times (\mathbb{V}_3 - \mathbb{V}_2 - \mathbb{U})\right)\right] \tag{4.4}$$

$$\mathbb{I} = g(\mathbb{Y}_e)\left[\exp(\alpha_{a-} \times -\mathbb{V}_1) - \exp\left((\alpha_{a-} - 1)\mathbb{V}_1\right)\right] \tag{4.5}$$

where f and g are functions of the current state of concentrations of the positive electrode ($\mathbb{Y}_+$) and electrolyte ($\mathbb{Y}_e$, approximated as constant); α_a is the anodic charge transfer coefficient with additional subscripts denoting the positive or negative electrode; $\mathbb{V}_1$, $\mathbb{V}_2$, and $\mathbb{V}_3$ are the voltages of the electrolyte at the boundary of the negative electrode, the voltage of the electrolyte at the positive electrode boundary, and the voltage of the positive electrode respectively; and $\mathbb{U}$ is the open circuit potential describing the battery potential at equilibrium for a given concentration in the positive electrode, and was determined from a combination of supplier data and experimental data. A basic schematic of the system setup is given in Figure 4.2.

These equations were implemented with a combination of optimization and finite difference approaches to converge on currents and concentrations in the battery as suggested by Fabre et al. [14], with implementation aided by additional numerical method techniques from [67] and [66]. Additional approximations included by Fabre, and retained in our model include: no potential drop in the negative electrode, constant conductivity in the electrolyte, and no self-heating effects.

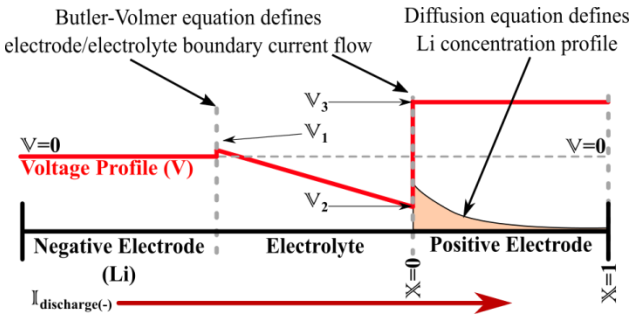

Figure 4.2 Battery model schematic. The one-dimensional battery model is shown with the voltage and spatial locations. The corresponding equations are indicated. Adapted from [42] (see chapter 3).

Additionally we treat the positive electrode as a perfect electrical conductor so no voltage drop occurred. For simplicity the diffusion coefficient was based on the concentration of the previous time step, removing the time dependency.

Due to the fast changes that can take place in repeated cap-cycles, it may be necessary to discretize with very fine time steps during certain periods in the finite difference approach. Numerically, the result of these fast dynamics is an increase in numerical expense for solving a single cap-cycle. This becomes problematic when extending the modeling to long periods of time, where it is not realistic to perform detailed modeling for all cap-cycles. Therefore an approach for taking current system states and being able to project these over many repeated cap-cycles in the future is of great interest.

4.3.3 Projection Modeling: Direct Transition Matrix Approach

Various sets of system quantities can be used as states of a dynamic system. The "perturbed state approach" used changes of concentration in the positive electrode ($\Delta\mathbb{Y}_+$) as states of the system and was presented by the authors with the basic switching model in [42] (see chapter 3). This projection approach used perturbation of the concentration changes at each finite difference grid point of the positive electrode independently to build a numerical Jacobian or transition matrix. One major limitation of this approach was the necessity to perturb the system for each grid point. This burden can be reduced through parallel processing. However, it was determined that if a change was made to the state definition, then the transition matrix could be developed directly from the model without the need of perturbations. Instead of using the change in concentration, $\Delta\mathbb{Y}_+$, as the states of the system, the concentrations themselves, $\mathbb{Y}_+$, were used. The transition matrix associated with these states then becomes the accumulated finite difference

steps during each cap-cycle. This change may seem insignificant, yet as will be seen can have important implications for computational efficiency.

The basic development of the new transition matrix is presented here. The positive electrode lithium concentration profile calculated by the finite difference is a function of the current and diffusion coefficient. The current dictates the boundary condition and all points are functions of the diffusion, which in turn is dependent on the concentration (for simplicity the diffusion coefficient was based on the concentration of the previous time step). The finite difference approach in concentration used to solve Equations 4.1, 4.2, and 4.3, can be expressed as:

$$\mathbf{A}_{i,n}\mathbb{Y}_{\mathrm{i,n+1}} = \mathbf{B}_{i,n}\mathbb{Y}_{\mathrm{i,n}} + \mathbf{r}_{i,n} | \, \mathbf{A}, \mathbf{B} = f(\mathbb{D}) \; and \; \mathbf{r} = g(\mathbb{I}, \mathbb{D}) \tag{4.6}$$

where $\mathbb{Y}_{\mathrm{i,n}}$ is the concentration profile vector in the positive electrode at time step "*n*" of cap-cycle "*i*." Matrices **A** and **B** are functions of the diffusion coefficient and **r** incorporates the boundary conditions for the given time step including the information about the flux (based on the electrical current) and the diffusion coefficients at the boundary.

The implementation of this in practice was done using a combination of information from [67] and [66], with the finite difference matrices set up as follows to account for a non-uniform mesh. For a 1D mesh of N+1 grid points, let h_k be the distance between grid point *k* and *k*+1, $\mathbb{D}_k$ be the diffusion coefficient of the grid point (based on the concentration from the last time step), and τ the time step size. We can then define:

$$p_k = \frac{h_k^2}{4h_{k-1}^2}\,\mathbb{D}_{k-1} + \frac{3h_{k-1}^2+2h_{k-1}h_k-h_k^2}{4h_{k-1}^2}\,\mathbb{D}_k - \frac{1}{4}\,\mathbb{D}_{k+1} \tag{4.7}$$

$$r_k = \frac{1}{4}\,\mathbb{D}_{k-1} + \frac{-h_{k-1}^2+2h_{k-1}h_k+3h_k^2}{4h_k^2}\,\mathbb{D}_k - \frac{h_{k-1}^2}{4h_k^2}\,\mathbb{D}_{k+1} \tag{4.8}$$

$$q_k = -(p_k + r_k) \tag{4.9}$$

$$s_k = \frac{(h_{k-1}+h_k)^2}{2\tau} \tag{4.10}$$

We then can build the inner parts of the **A** and **B** matrices from Equation 4.6:

$$\begin{gathered}\mathbf{A}(k,k-1) = -p_k; \mathbf{B}(k,k-1) = p_k \\ \mathbf{A}(k,k) = s_k - p_k; \; \mathbf{B}(k,k) = s_k + p_k \\ \mathbf{A}(k,k+1) = -r_k; \; \mathbf{B}(k,k+1) = r_k\end{gathered} \tag{4.11}$$

Using ghost points we address the diffusion coefficient at the boundaries,

$$C = \frac{2h_1^2}{\tau} \tag{4.12}$$

$$\mathbf{A}(1,1) = C + 2\mathbb{D}_1,\ \mathbf{A}(1,2) = -2\mathbb{D}_1$$

$$\mathbf{A}(N+1,N) = -2\mathbb{D}_{N+1},\ \mathbf{A}(N+1,N+1) = C + 2\mathbb{D}_{N+1} \tag{4.13}$$

$$\mathbf{B}(1,1) = C - 2\mathbb{D}_1,\ \mathbf{B}(1,2) = 2\mathbb{D}_1$$

$$\mathbf{B}(N+1,N) = 2\mathbb{D}_{N+1},\ \mathbf{B}(N+1,N+1) = C - 2\mathbb{D}_{N+1}$$

Finally, to incorporate the Neumann boundary conditions we convert the value to a Dirichlet condition for that time step to build the **r** vector from Equation 4.6, which is zero except the first element.

$$\mathbf{r}(1) = \mathbb{D}_{N+1} \tag{4.14}$$

With the finite difference matrices formulated we can then incorporate the boundary condition information in **r** with **B** such that Equation 4.6 is rewritten as:

$$\mathbb{Y}_{\mathrm{i,n+1}} = \mathbf{A}_{i,n}^{-1}\mathbf{B}_{i,n}^{*}\mathbb{Y}_{\mathrm{i,n}} |\ \mathbf{B}^{*} = f\left(\mathbb{I}, \mathbb{D}, \mathbb{Y}_{\mathrm{i,n}}\right) \tag{4.15}$$

If $\mathbb{I}$, current, and $\mathbb{D}$, diffusion coefficient, are known at each time step in a cycle, the matrices **A** and **B** can be determined directly. Thus, the full cycle transition matrix **Φ** can be calculated as:

$$\mathbb{Y}_{i+1,1} = \mathbf{\Phi}_{\mathrm{i}}\mathbb{Y}_{i,1} = \left(\prod_{j=1}^{n} \boldsymbol{A}_{i,j}^{-1}\boldsymbol{B}_{i,j}^{*}\right)\mathbb{Y}_{i,1} \tag{4.16}$$

This allows us to create the transition matrix from a single cap-cycle as a composite of all the finite difference steps. If we assume that the transition matrix is approximately constant over the projection of *m* cap-cycles, then, as in the perturbed state approach, we have:

$$\mathbb{Y}_{i+m,1} = (\mathbf{\Phi}_i)^m\mathbb{Y}_{i,1} \tag{4.17}$$

This enables one to use the transition matrix from a single cap-cycle to project over many cap-cycles similar to the perturbed state approach. Performing the calculations this way allows us to get an approximation of the states throughout the projection without needing to solve the algebraic component created by the Butler-Volmer equations, which is a critical source of computational complexity in this type of problem. Additionally, depending on hardware, this approach can have significant overhead reduction compared to the perturbed state approach.

There are two main limitations to this approach. First, as with the prior approach, we assume a constant transition matrix over the projection, which in essence approximates no changes in cap-cycle current and diffusion coefficients profiles over the projection, as well as certain aspects of the boundary concentration information. This assumption will likely be the main limitation in size of projection that can be made for a given permissible error, and will have varying effects dependent on the nonlinearities and loading of the system. Second, by defining the system states as the concentration levels, instead of differential concentration as in our previous work [42] (see chapter 3), we may reduce the sensitivity due to numerical round off error. However, loss in sensitivity can be outweighed by decreased numerical expense in our current application.

4.3.4 Error Analysis

Since a major limiter to the projection size is the error caused by the approximation of a constant transition matrix over the full projection, understanding the severity of various components of this error provides insight for its mitigation. Therefore, here we performed a detailed error analysis of the assumptions related to a constant transition matrix. To frame this analysis we need to revisit the formulation of the direct projection transition matrix,

$$\mathbb{Y}_{\mathrm{i,n+1}} = \mathbf{A}_{\mathrm{i,n}}^{-1}\left(\mathbf{B}_{\mathrm{i,n}}\,\mathbb{Y}_{\mathrm{i,n}} + \mathbf{r}_{\mathrm{n}}\right) = \mathbf{A}_{\mathrm{i,n}}^{-1}\mathbf{B}_{\mathrm{i,n}}^{*}\,\mathbb{Y}_{\mathrm{i,n}}. \tag{4.18}$$

In the first part of the equation $\mathbf{r}_{\mathrm{n}}$ is independent of $\mathbb{Y}$; however, to bring this boundary condition information into the transition matrix, $\mathbf{r}_{\mathrm{n}}$ is incorporated into $\mathbb{B}^*$ resulting in $\mathbb{B}^*$ necessarily becoming coupled with the concentration $\mathbb{Y}$ around the boundary. We can rewrite Equation 4.18 as

$$\mathbb{Y}_{\mathrm{i,n+1}} = \mathbf{A}_{\mathrm{i,n}}^{-1}\left(\mathbf{B}_{\mathrm{i,n}} + \mathbf{r}_{\mathrm{n}}^{*}\right)\mathbb{Y}_{\mathrm{i,n}} \mid \mathbf{r} = f\left(\mathbb{I}_{\mathrm{i,n}}, \mathbb{D}_{\mathrm{i,n}}, \mathbb{Y}_{\mathrm{i,n}}\right) \tag{4.19}$$

where $\mathbf{r}^*$ assumes the dependence on $\mathbb{Y}$ around the boundary. If we assume N finite difference steps for one full cap-cycle, we can then express the concentration changes over the entire cap-cycle as:

$$\begin{aligned}
\mathbb{Y}_{\mathrm{i,N+1}} &= \mathbb{Y}_{\mathrm{i+1,1}} \qquad (4.20)\\
&= \mathbf{A}_{\mathrm{I,N}}^{-1}\left(\mathbf{B}_{\mathrm{I,N}} + \mathbf{r}_{\mathrm{I,N}}^{*}\right) \ldots \mathbf{A}_{\mathrm{I,1}}^{-1}\left(\mathbf{B}_{\mathrm{I,1}} + \mathbf{r}_{\mathrm{I,1}}^{*}\right)\mathbb{Y}_{\mathrm{I,1}} \mid \mathbf{A}, \mathbf{B} = f(\mathbb{D}); \mathbf{r}^{*} = f(\mathbb{I}, \mathbb{D}, \mathbb{Y})\\
&= \prod_{\mathrm{j=0}}^{\mathrm{N-1}}\left\{\mathbf{A}_{\mathrm{i,N-j}}^{-1}\mathbf{B}_{\mathrm{i,N-j}} + \mathbf{A}_{\mathrm{i,N-j}}^{-1}\mathbf{r}_{\mathrm{N-j}}^{*}\right\}\mathbb{Y}_{\mathrm{i,1}}\\
&= \boldsymbol{\Phi}_{\mathrm{i}}\mathbb{Y}_{i,1} \mid \boldsymbol{\Phi}_{\mathrm{i}} = f(\mathbb{I}, \mathbb{D}, \mathbb{Y})
\end{aligned}$$

Here we see that the transition matrix $\mathbf{\Phi}$ is in reality a function of the current profile during the cap-cycle, $\mathbb{I}$, the diffusion coefficient, $\mathbb{D}$, and the concentration $\mathbb{Y}$ around the boundary. Using the projection approaches described previously, $\mathbf{\Phi}$ is approximated as constant over the projection. The error associated with this simplification can be divided into three main components. First is error due to changes in the diffusion coefficient in the main bulk of the electrode. This is caused by the concentration dependence of the diffusion coefficient and comes from errors associated with the $\mathbf{A}^{-1}$ and $\mathbf{B}$ matrices. Second is error due to the changes in the current profile from one cap-cycle to the next. Third is error associated with changes in concentration and diffusion at the boundary. This accounts for the diffusion and concentration dependency of $\mathbf{r}^*$. If we assume that the transition matrix is based on some earlier cap-cycle "*O*," we can define these errors as follows:

$$\mathbf{E}_{\mathrm{A^{-1}:i,n}} = \mathbf{A}_{O,\mathrm{n}}^{-1} - \mathbf{A}_{\mathrm{i,n}}^{-1} \tag{4.21}$$

$$\mathbf{E}_{\mathrm{B:i,n}} = \mathbf{B}_{O,\mathrm{n}} - \mathbf{B}_{\mathrm{i,n}}$$

$$\mathbf{E}_{\mathrm{r^*:i,n}} = \mathbf{r}_{O,\mathrm{n}}^{*} - \mathbf{r}_{\mathrm{i,n}}^{*}$$

where $\mathbf{E}_{\mathrm{A^{-1}:i,n}}$ is the error or difference between the values of $\mathbf{A}^{-1}$ in the current cap-cycle "*i*" and time step "*n*", $\mathbf{A}^{-1}$ of time step "*n*" for the earlier cap-cycle "*O*" on which the projection transition matrix is based. Similarly with $\mathbf{E}_{\mathrm{B:i,n}}$ and $\mathbf{E}_{\mathrm{r^*:i,n}}$. The error $\mathbf{E}_{\mathrm{r^*:i,n}}$ is a combination of $\mathbf{E}_{\mathbb{I}\mathrm{:i,n}}$, the error associated with the change in the current profile, and $\mathbf{E}_{\mathbb{B}\mathrm{:i,n}}$, the error associate with the boundary concentration and diffusion,

$$\mathbf{E}_{\mathrm{r^*:i,n}} = \mathbf{E}_{\mathbb{I}\mathrm{:i,n}} + \mathbf{E}_{\mathbb{B}\mathrm{:i,n}} \tag{4.22}$$

Using this we can generalize and rewrite Equation 4.20 as:

$$\mathbb{Y}_{\mathrm{i+1,1}} = \{f(\mathbf{A}_O^{-1}, \mathbf{B}_O, \mathbf{r}_O^*) - f(\mathbf{A}_O^{-1}, \mathbf{B}_O, \mathbf{r}_O^*, \mathbf{E}_{\mathrm{A^{-1}:}O}, \mathbf{E}_{\mathbf{B}:O}, \mathbf{E}_{\mathbb{I}:O}, \mathbf{E}_{\mathbb{B}:O})\}\mathbb{Y}_{\mathrm{i,1}} \tag{4.23}$$

A more thorough formulation of this expression can be done, but does little here to further the topic so will not be presented. Details of the findings will be given later.

4.3.5 Projection Modeling: Updating Transition Matrix Approach

Ultimately our goal is to be able to model these systems in an accurate, numerically reasonable way. The ability to analyze the error and to separate the various components and interactions is extremely helpful in determining potential error reduction strategies. If at select

steps in the projection we could update the transition matrix with real or approximated values, we could potentially lengthen the projection and/or reduce the error. Some key considerations are as follows: first, updating $\mathbb{B}$, $\mathbb{D}$, and $\mathbb{I}$ of a step during the projection would in essence be similar to running a full model and would essentially eliminate error (and give no numerical savings); second, updating $\mathbb{I}$ is numerically expensive in that we need to calculate the Butler-Volmer equations for each time step of the cap-cycle to gather that information, which is likely comparable to performing the full model; third, updating $\mathbb{D}$ and $\mathbb{B}$, can be done at a lower numerical cost because an approximation at each time step can be determined without needing to solve the algebraic aspects of the Butler-Volmer equations. Using these considerations and outcomes from the error analysis we implemented a transition matrix updating method where key aspects of the transition matrix are adjusted at certain points in the projection.

4.4 Case Study: Thin-film Battery Loading

With a modeling approach fully developed, it is instructive to see this technique demonstrated in a case study. As mentioned previously, one problem of interest for this type of modeling is loading of thin-film batteries with repeated capacitive loads, such as what could be seen in certain microrobot applications [34, 36, 68]. For example, walking gaits for a piezoelectric microrobot requires repeated charging of piezoelectric actuators that behave electrically as capacitive loads. The modeling incorporated findings based on a simplistic switching approach from the authors' in [41] (see chapter 2) to accommodate repeated cap-cycles and the perturbed state approach in [42] (see chapter 3). This application can see fast current and voltage changes at times, necessitating fine discretization during certain time periods in the finite difference approach. Using the approaches mentioned here for taking current system states of the battery and being able to project these over many repeated cap-cycles in the future is of great importance. For a given permissible error in projection, projection lengths will need to be shorter later in the battery discharge as non-linearities increase, as seen in part in the battery discharge profile sketch in Figure 4.1. For this case study, permissible errors were set and simple algorithms implemented to determine projection size.

It is worth noting also that the given load scenario of the case study in this and prior modeling work by the authors is a light load and it has been determined that simpler underlying battery models could be used with equal validity. However, the electrochemical model presented here gives a broader range of applicability than simpler models do (such sceneries have been

identified) and allows for more direct parameter correlation, such that the modeling concepts and approaches presented are considered valid and useful. Some minor issues with the model implementation were addressed for the two new approaches presented here, and the current implementation shows some limitations at times when the battery has low loads on the order of the leakage current of the circuit that cause some numerical oscillations, but these issues are minor.

4.4.1 Experimental Data Acquisition

Experimental testing was performed previously, for calibration and validation, to simulate a load profile similar to a cycled piezoelectric actuator, using a standard capacitor (constant current discharges were also used in calibration). The batteries used for experimental testing were 50μAh thin-film lithium batteries from Cymbet™ [46]. These batteries had a chemistry that would potential be suitable for microrobotic applications, although form factor and other aspects of off-the shelf batteries is not currently compatible. It appears that these may be "Li-free" batteries, meaning the lithium negative electrode is likely plated on the current collector during the first charging of the battery rather than an ideal lithium source, yet our modeling still appears adequate. Model calibration and initial results were published in [42] (see chapter 3). Detailed description of the limitations in the data is given in [41, 42] (see chapters 2 and 3), however four main general points will be noted. First, the current measurement for the cycled tests was measured with an AC probe and converted to a DC reading with accuracy limited by the conversion approach. Second, substantial noise and extraneous effects in the cycled data had to be addressed. Third, the testing was performed with multiple batteries, so some variability was introduced. Fourth, constant current data used for calibration, which reported lower capacities then the published data sheet, was linearly scaled to correspond with those of the calibration switching data set based on an equivalent current in attempt to account for differences in dataset acquisition/assumptions and ultimately to align assumed comparable capacity usage [42] (see chapter 3). It is unclear why the constant current data would be further from the published data values when it was taken with a more straightforward measurement approach. Because of these limitations, the data here is used more for model approach validation rather than for use as precise experimental result presentation. Representative profiles of the switching dynamics will be shown later.

4.4.2 Direct Transition Matrix Approach

From the validation dataset, the starting voltage is input into the model as an initial condition (all other information comes from the calibration). This starting voltage measurement is influenced by the leakage current, and is accounted for in the model as before [42] (see chapter 3). An algorithm was developed to determine projection size based on permissible errors. Projections ranged from 100-40,000 cap-cycles, with more aggressive projection possible. A certain number of fully simulated cap-cycles after each projection were generally added to allow the model to settle. Projections began after the 200th cap-cycle, where projections began after the 300th cap-cycle in the perturbed state approach.

The overall discharge profile of the battery validation dataset [42] (see chapter 3) and the direct transition matrix approach are shown in Figure 4.3 and show good agreement.

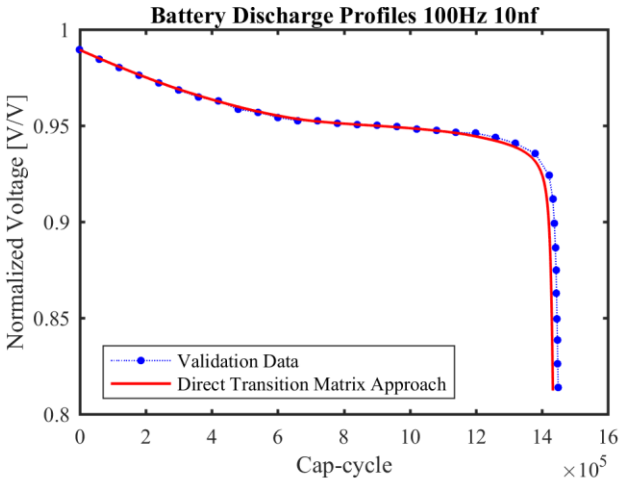

Figure 4.3 Model and validation data comparison full battery discharge. Validation data is averaged unlike that shown in [42] (see chapter 3).

In addition to the overall battery discharge profile, comparison was made between experimental data and the direct transition matrix approach for detailed profiles of the capacitor charge. Two sample charge profiles are given with the overall discharge profile in Figure 4.4 to represent the fit of the model and validation data over time. This fitting of the individual cycles is comparable to the perturbed state approach.

4.4.3 Error Quantification

Quantification of errors caused by approximations during projection is desirable for targeting modeling improvements.

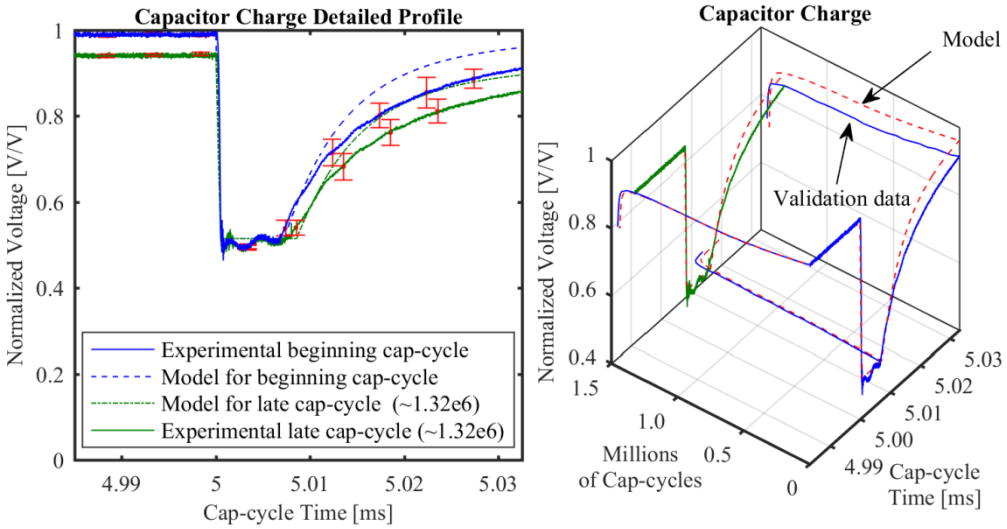

Figure 4.4 (Left) Model and validation data comparison of a detailed capacitor charge profile. Error bars show error from rolling average and from discrepancy between battery and capacitor voltage readings. (Right) The validation and model data are presented with just key features showing the fit in select cycles and over the full battery discharge. Error bars are omitted from the experimental data.

One simplistic method of error quantification is through performing comparison between full modeling of a series of cap-cycles and an associated projection over the same series. This preliminary error quantification was performed for three separate series in the modeled battery discharge that represent three key regimes. The first series begins near cap-cycle 200 of the discharge, where non-linear affects are low. The second series begins near 1e6 cap-cycles, which still has low nonlinearities in the open circuit potential profile but is in the range where diffusion coefficients are changing. The final series begins near 1.4e6 cap-cycles. Here, there are significant nonlinearities and the error grows quickly with projection size. Each of these three series were fully simulated for 1,000 cap-cycles, and a corresponding projection was also calculated over the same period.

Two aspects of the error seen between the fully simulated cap-cycles and the projected cap-cycles are of interest. First is the boundary condition $\mathbb{Y}_{+}(0)$, the normalized lithium concentration at the positive electrode/electrolyte boundary, which is approximated to range from 0.5 if a battery is fully charged to 1V/V and 1 at fully discharged. This boundary influences the voltage of the electrode as well as indicates when the battery is fully discharged. Second is the integrated area of the lithium concentration profile in the positive electrode. This is an expression of the amount of capacity used, and conversely, the amount of capacity left in the battery. The lithium profiles across the positive electrode at the beginning of the three projections are shown in

Figure 4.5. For faster switching (higher average current) and for lower diffusion coefficients, the profiles would show more variation across the electrode.

For each of the three series, the error over the 1,000 cap-cycles was calculated as the difference between the normalized lithium concentration in the positive electrode, $\mathbb{Y}_{+}(0)$, of the direct projection method and the fully simulated series results (i.e. no projections over the 1,000 cap-cycles).

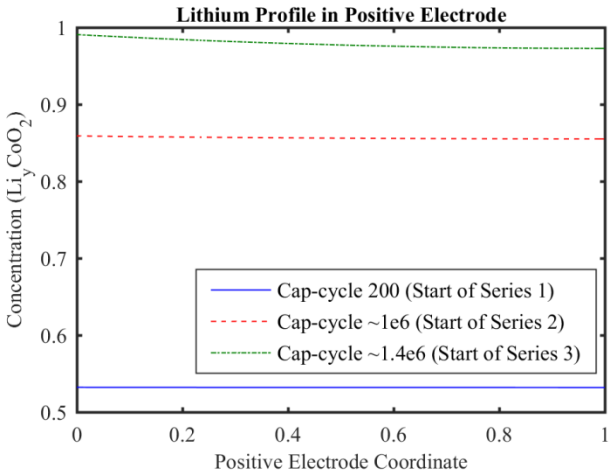

Figure 4.5 Lithium profile in the positive electrode at the beginning of the three projections for error analysis.

This error was then normalized by the change in concentration of cap-cycle 200. This means that the errors presented indicate approximately the fraction of the change seen in one regularly modeled cap-cycle. The errors per cap-cycle are given in Figure 4.6.

It can be seen that the error for the boundary concentration is quite low for series 1, yet is much higher for series 2 and 3 where there are significant nonlinearities. However, for the integrated concentration the errors are more similar, and the first series actually showing slightly more error than the others. These plots suggest that understanding of the error contributions over time could potentially improve the accuracy of the projection, and/or allow for larger projections or decreased numerical expense.

In light of this, a more thorough error analysis was performed, as described in Section 4.3.4. The key feature of the error is that the different components contribute to the combined error at different times and in different ways. To further understand these different components we selected a reference cap-cycle near the beginning of the full battery discharge (10th cap-cycle) as a base. Using notation from Equations 4.18 and 4.23, we can develop the **A** and **B*** matrices for all the steps in this base cap-cycle. These matrices combined can form the base transition matrix.

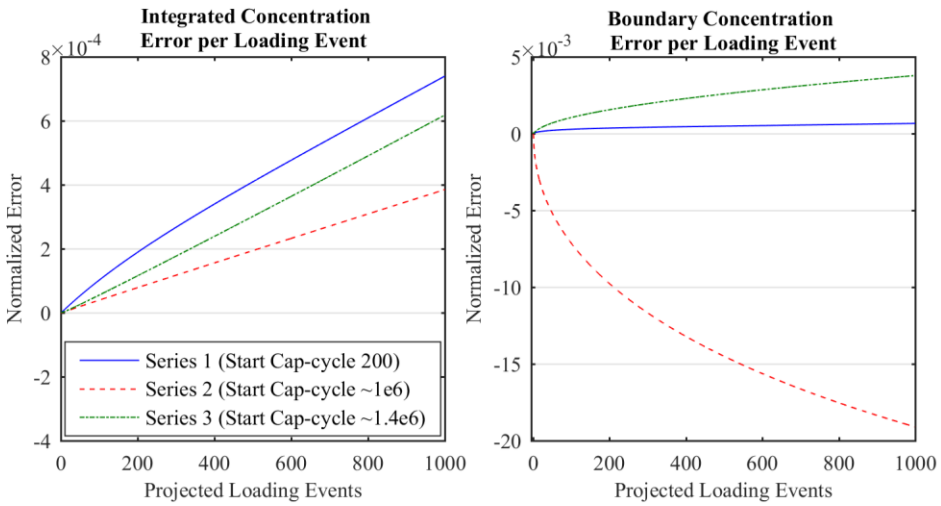

Figure 4.6 (Left) Integrated concentration error per cap-cycle for three separate projections. (Right) Boundary concentration error per cap-cycle for three separate projections.

In order to compare different components of the error, we adjusted these base **A** and **B*** matrices in several ways for each cap-cycle modeled. It should be noted that the cap-cycles modeled in this error analysis are a large subset of the cap-cycles fully modeled during the direct transition matrix approach. For each cap-cycle analyzed we used the concentration profile determined in the direct transition matrix approach, previously presented, as the beginning concentration for the cap-cycle. Then the changes associated with that cap-cycle were calculated in the following way: First, the concentrations were calculated solely using the base matrices (Base). Second, these base matrices were adjusted to account for diffusion coefficient difference in the bulk of the positive electrode, thus removing that error component ($\mathbb{D}$). Third, the base matrices were adjusted to account for the current profile difference, thus removing that error component ($\mathbb{I}$). It should be noted that the current profiles used to update the matrices were from those stored during the full modeling, as these are not readily available without fully modeling the cap-cycle. Fourth, the base matrices were adjusted to account for boundary concentration and diffusion differences, thus removing that error component ($\mathbb{B}$). Combinations of these adjustments were also performed. Because the discretization in time for each cap-cycle was not necessarily equal from cap-cycle to cap-cycle, linear approximations of some values were made when applying data from one cap-cycle to another. Finally these were compared to the fully modeled cap-cycle obtained when running a full direct transition matrix approach. The error then became the difference between the concentration profile change in the fully modeled cap-cycle and the profile developed using the base and augmented matrices. The error between each

approach and the fully modeled cap-cycle was normalized by the change in concentration of the 200th cap-cycle, as before. Boundary and total integration concentration errors are presented in Figure 4.7. Upper plots of Figure 4.7 show the normalized error. The middle two plots show a

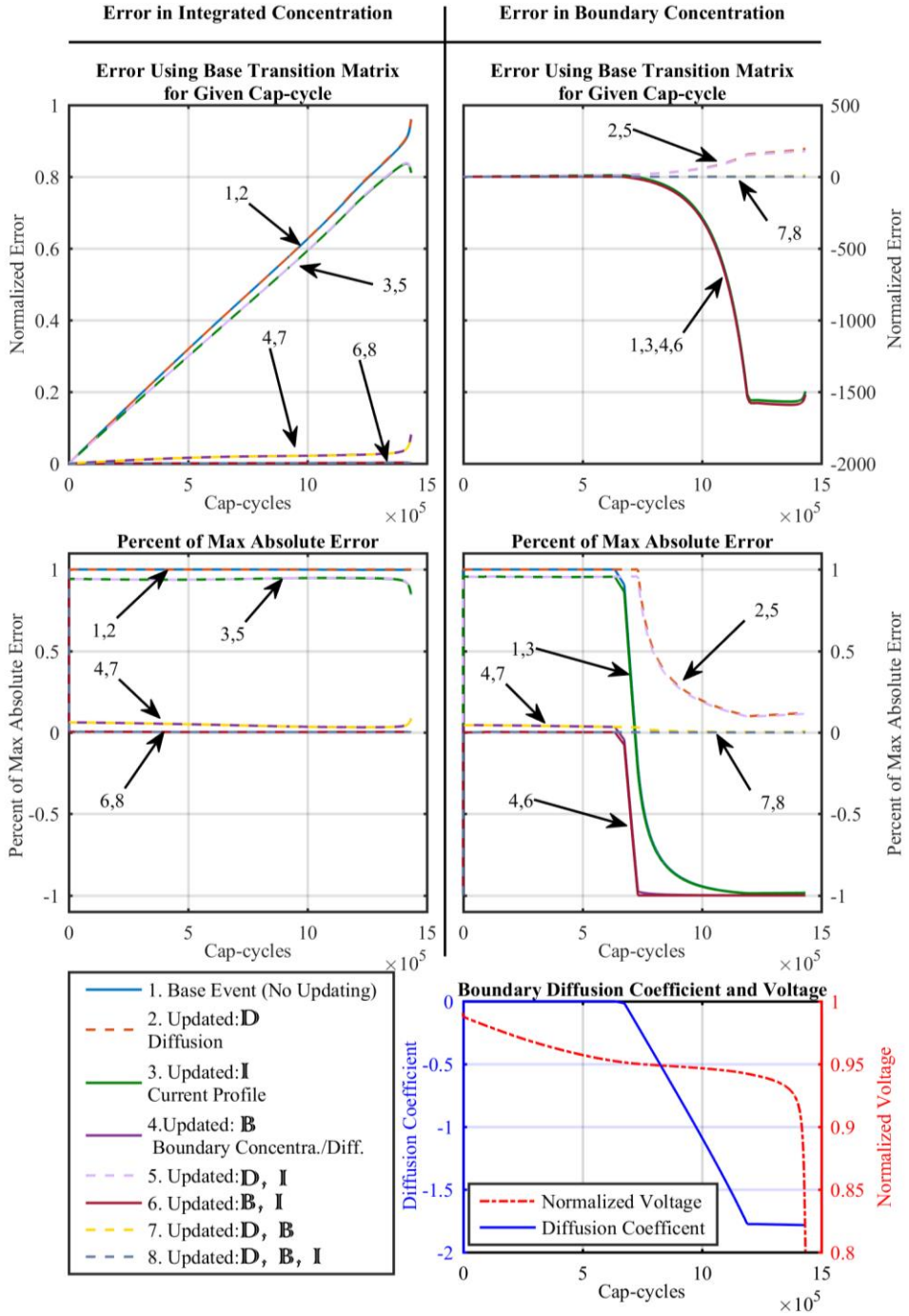

Figure 4.7 Error analysis results. Errors associated with using information from the base (10th) cap-cycle to calculate the concentration change for the given cap-cycle compared to the full modeling of that cap-cycle. (Left) Error in the boundary concentration. (Right) Error in total integrated concentration. (Top) Error for the given scenarios normalized by the change in concentration of the 200th cap-cycle. (Middle) Ratio of the error for each scenario compared to the maximum absolute error of any scenarios for the given cap-cycle. (Bottom-Right) The boundary diffusion coefficient and voltage, given for references to see the nonlinearities introduced.

ratio of the error for each adjustment approach compared to the maximum absolute error seen in any of the adjustment approaches (including no adjustment, or the base transition matrix) for the given cap-cycle. Finally, in the bottom right the boundary diffusion coefficient and voltage are given for reference to help visualize nonlinearities being introduced into the system.

The overall error plots (top two plots) give an understanding that the magnitude of the boundary error is significantly larger than that of the total concentration error. Although not distinguishable in this plot, this is true for earlier loading events, but at a smaller magnitude difference. Additionally, it is striking that the total concentration error has a nearly linear rise compared to the non-linear boundary error. Finally, the total concentration error seems little affected by the changing diffusion coefficient and more affected by the voltage profile, whereas the boundary seems affected by both. This last point compliments the determination of which updating method gives the greatest improvement. For both types of error the best results are when updating is done for all three components, however if only updating two of the three, the best updating approach is different for the boundary or total concentration error (total concentration is benefited by the updating $\mathbb{I}$ and $\mathbb{B}$, and boundary concentration is benefited most by updating the $\mathbb{B}$ and $\mathbb{D}$). Combining these we can state that the total concentration error is most affected by changes in the electrical aspects of the system, that is current and voltage. Whereas the boundary concentration error is more affected by changes in the diffusion and boundary concentration. However, if we were to switch those, the effect of updating only $\mathbb{I}$ and $\mathbb{B}$ has a much more adverse effect on the boundary concentration than updating only $\mathbb{B}$ and $\mathbb{D}$ has on the total integrated concentration. Understanding this can allow error reduction in a more systematic way.

For comparison, the same approach was used for a reduced number of cap-cycles for a 1kHz 10nF loading, and the plots of the normalized error are shown in the bottom plots of Figure 4.8. It can be seen that very similar error occurs at this elevated loading.

4.4.4 Updating Transition Matrix Approach

Using the information gathered from the error analysis we implemented a transition matrix updating method. For each projection, at five points during the projection the transition matrix was updated using current approximations of $\mathbb{D}$ and $\mathbb{B}$. The numerical cost for the combined five updates was equivalent to about one regular function call or cap-cycle.

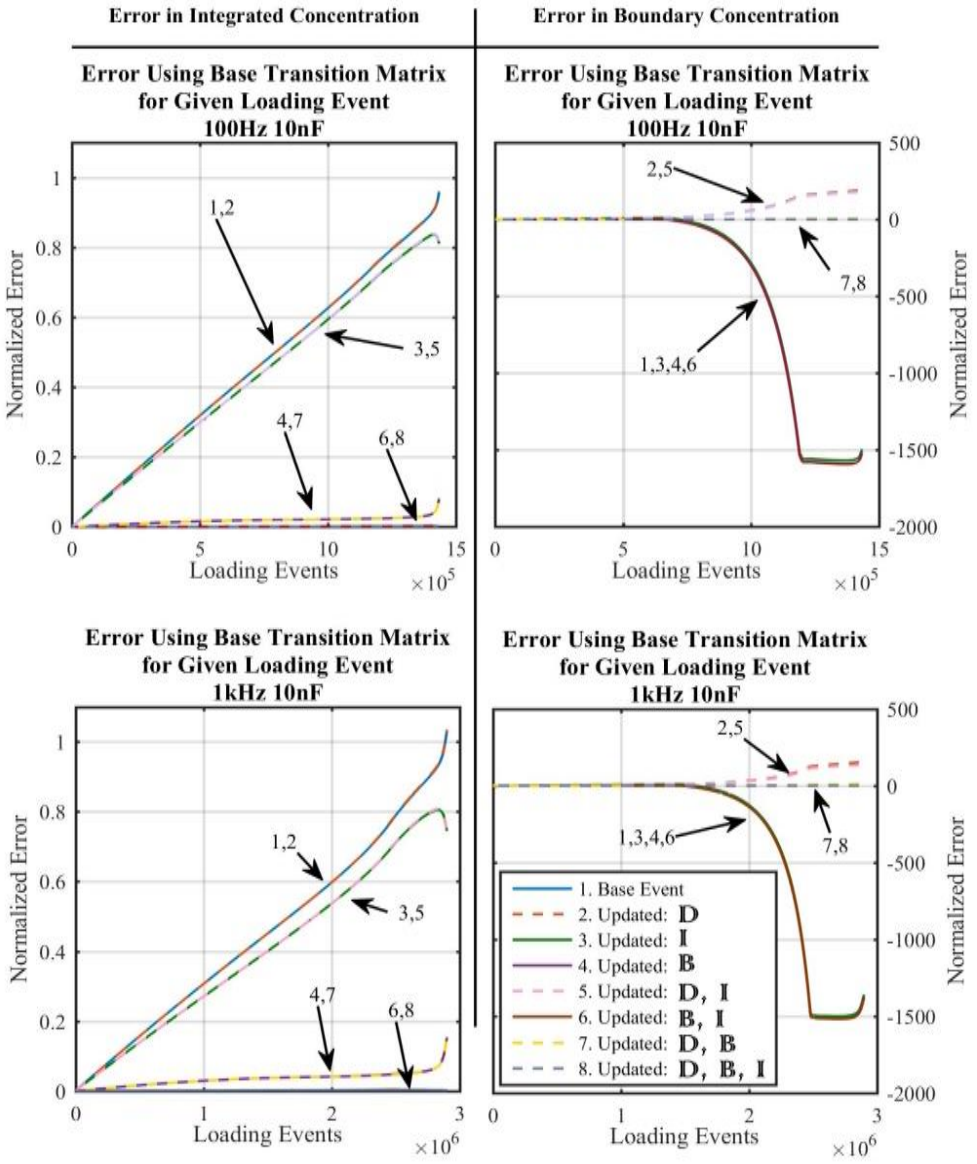

Figure 4.8 Error analysis plots for (Top) 100Hz 10nF for comparison (Bottom) 1kHz 10nF load. Errors associated with using information from the base (10th) cap-cycle to calculate the concentration change for the given cap-cycle compared to the full modeling of that cap-cycle. (Left) Error in the boundary concentration. (Right) Error in total integrated concentration. Error for the given scenarios are normalized by the change in concentration of the 200th cap-cycle.

4.4.5 Approach Comparison

The overall discharge profile of the battery validation dataset and the perturbed state approach [42] (see chapter 3) is compared to the two projection approaches presented here and is shown in Figure 4.9. It can be seen that there is close agreement with all approaches.

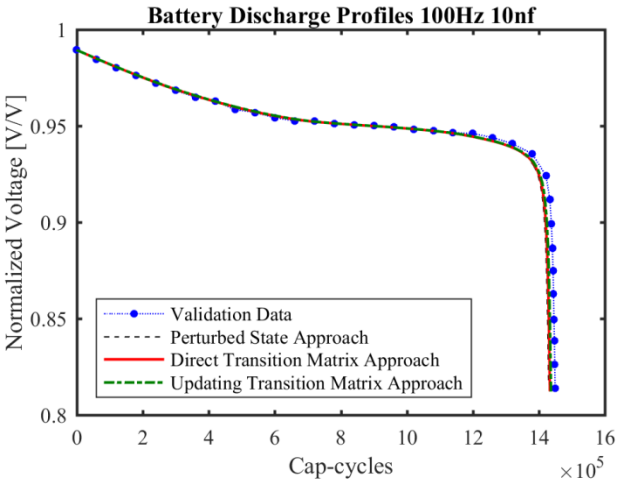

Figure 4.9 Comparison of the updating transition matrix approach with the direct transition matrix approach, experimental data and the perturbed state approach in [42] (see chapter 3). Validation data is averaged unlike that shown in [42] (see chapter 3).

To compare the numerical costs between the perturbed state approach and the approaches reported here it is useful to look at the number of cap-cycles fully modeled (or equivalent function calls) compared to the total number of cap-cycles modeled (including projections). To perform this calculation, certain approximations had to be made as to how to deal with overhead and parallel processing. It is understood that this is not a perfect comparison between the three approaches in that the some variations existed between the methods (e.g. number of cap-cycles before projections began, parallel processing, overhead, and allowed error algorithm variation), but the comparison is still considered instructive.

For the given hardware and permissible error algorithms used, the direct approach had a numerical cost of 0.08% (equivalent function calls/total cap-cycles) after ~0.74 million cap-cycles and 0.46% after ~1.43 million cap-cycles where the updating approach was only 0.14% after ~1.43 million cap-cycles. This may be compared to our previous approach, the perturbed state approach, with states of differential concentration [42] (see chapter 3), which reported a cost of 0.19% after ~0.677 million cycles, and 6% after ~1.43 million cycles. A comparison of the three projection transition matrix approaches is given in Table 4.1 where the numerical expenses are compared with representative times. It is acknowledged that costs will vary depending on hardware, assumptions of overhead etc., and with acceptable error algorithms, however, these findings highlight potential gains for the direct and updating approaches. Times were based strictly off of an approximate 3 sec per function call which is a reasonable approximation for demonstration. The length of this function call is important to highlight for

two reasons. First, the time stepping approach within each cycle was not optimized and improvement could be made in future work in the time required. Second, even with significant improvements in function call time, due to the large number of total cap-cycles per test, any appreciable function call time will likely necessitate model reduction methods. A final note is that the computation time for the updating transition matrix approach in this modeling scenario, was less than the experimental run-time, thus suggesting potential pseudo-real time applications.

Table 4.1 Computational Expense for Various Projection Approaches

Transition Matrix Approach	Total Loading Events	Function Calls	Approx. Function Time [hr]	Numerical Cost
Perturbed	1.430e6	90510	75.4	6.3%
Direct	1.430e6	6558	5.5	0.46%
Updating	1.430e6	2038	1.7	0.14%

4.5 Conclusions

Prior work by the authors aimed at exploring the potential of modeling systems with repeated capacitive loading, in particular for MEMS applications. This prior work combined switching and battery dynamics to explore the effects of this type of loading on a potential battery system. However, numerical expense of one capacitive load event (cap-cycle) was significantly numerically intensive to preclude reasonable modeling of the proposed full system. Therefore, a projection approach was presented in that work to reduce this expense by projecting system states over large series of consecutive cap-cycles. This perturbed state approach greatly reduced the numerical expense, however, significant expense was still required.

This work adapts and expands the perturbed state approach in two significant ways. The first (denoted as the direct approach in the text) is in a fundamental redefinition of the states of the system. By defining the states of the system to be concentration values rather than differential concentrations, the transition matrix is developed directly from the model, eliminating the need for state perturbations. This in turn reduces the numerical overhead while achieving very similar results to the perturbed state approach.

The second improvement is based on information from an error analysis of the projection. By understanding various components and sources of error in the projection, based on approximations inherent in the transition matrix, an error reduction strategy was developed and implemented. This approach periodically updated diffusion coefficient values and boundary diffusion coefficient and concentration values during projections based on the direct transition

matrix approach. The numerical expense of updating can be significantly cheaper than running a full model due to the fact that the algebraic relationships of the Butler-Volmer equations do not have to be resolved. This approach, with the simplistic implementation presented here, has modest gains over the direct approach, however, greater improvements are undoubtedly achievable.

A case study was run to demonstrate the implementation of these projection approaches and significant reduction in numerical expense was seen. Although for the given loading conditions in the scenario presented, more simplistic base models of the battery could be used, the presented modeling approach can be used in a broader range of loading cases, has more direct correlation with physical parameters, and should be able to be adapted for even more extreme loading conditions than currently suited for. Additionally, this methods presented should be applicable to more complex battery dynamics and/or areas beyond the current electrochemical example.

CHAPTER 5 SIMULATION TECHNIQUE CASE STUDIES

5.1 Abstract

Implementation of battery models can vary depending on loading scenario. Recent work by the authors' presents modeling and simulation techniques based on repeated fast dynamic loading of thin-film batteries. These techniques were developed to address timescale issues with modeling these types of loads. To compliment that work, here we explore various aspects of these modeling techniques through a series of case studies. These scenarios explore different battery and load configurations to demonstrate and highlight aspects of these techniques.

5.2 Introduction

Battery modeling and simulation are key aids in design and control of many battery based systems. Various aspects of battery modeling have been explored in the literature [52, 69]. Recent work by the authors has focused on modeling of thin-film batteries subjected to repeated fast-dynamic loads [42, 43] (see chapters 3 and 4). In particular, the battery loading examined was tailored to mimic repeated capacitive loading as seen in common microelectromechanical systems (MEMS) actuators (e.g. piezoelectric). These types of loads can be seen in applications such as the walking microfabricated robots reported in [34, 36, 68].

The basics of the model builds on thin-film battery modeling reported by Fabre et al. [14], and is extended to include switching dynamics and parasitic capacitance as seen experimentally in authors' prior work [41] (see chapter 2). The modeling also accounts for dynamics involved in the battery/load interaction. These combined dynamics exhibited characteristics on disparate timescales, e.g. switching dynamics on the order of microseconds and full battery discharge on the order of hours. These modeling techniques allowed for detailed modeling of individual load events while capturing changes over long stretches of repeated loading events. This bridging of timescales was accomplished by using a transition matrix approach that approximated system state changes over many loading events.

The development of these modeling techniques was done to allow more informed design and control of capacitively loaded systems based on battery power. With the model framework in place, this work uses these modeling techniques in a variety of design "case studies." These case studies explore different modeling aspects that will be important when determining reasonable modeling implementation, and demonstrate example microrobot power system design implementation.

There are two main aspects of model implementation that are addressed. First we look at loadings where simplistic modeling can be adequate instead of a more detailed electrochemical model. In our original work, for simplicity, we used a fairly light load for the model demonstration and validation. However, at such low loads more simplistic electrochemical modeling may often be adequate. Throughout this paper we will refer to the model developed in our prior work, with detailed electrochemical expressions, as the "detailed model." In the first case study we revisit this original light loading and compare our original detailed model with a simplistic model that will be described. The second case study then looks at a heavier battery load where the simplistic model begins to degrade. Again the detailed and simple models are compared. These first two scenarios demonstrate the need at higher average current loading for more detailed, or at least, augmentation of simple modeling techniques.

The last two case studies look at various design configurations for higher voltage operation. The third case study compares batteries in series used to directly charge a capacitor. Only a single loss source in the switching is implemented (others can be easily added), and this is used to determine energy transfer to a load capacitor based on the number of batteries in series. Again the detailed and simple models are run for comparison. The final case study then looks at batteries in parallel or batteries with greater surface area. This battery is modeled with a boost converter circuit. The combination of case studies three and four demonstrate how circuit design can be aided by these modeling techniques to determine the most effective voltage transforming approach. Together all these scenarios allow for a view of different applications of the modeling techniques developed, in a context comparable to microrobotic applications.

It is important to note that battery model reduction or enhancement can likely be done at a variety of levels in the case studies presented; however, the simple and detailed models presented do give a broad range of modeling. Additionally, there are additional advantages to direct electrochemical modeling in terms of fabrication design of the battery.

5.2.1 Nomenclature

A brief description of the nomenclature in this paper will be important. There are two main modeling approaches used in this paper. The first is the "detailed model" that corresponds to the detailed electrochemical model and projection approach presented in our prior work [42, 43] (see chapters 3 and 4). A brief overview of this model will be given. The other modeling approach will be referred to as the "simple model." This model approximates the electrochemical dynamics in the battery in a very simplistic way. The basics of this model will also be explained in the text.

The battery load of interest in this and prior work focuses on repeated fast-dynamic loading of thin-film batteries. In particular we are interested in repeated capacitive loads (mimicking that caused by switched piezoelectric or electrostatic actuators). In this case a "load event" is one charge and discharge of the load capacitor or actuator and will be referred to as a "cap-cycle." In prior work this was sometimes referred to as just cycles, but to remove confusion with battery discharge cycles we will use "cap-cycle."

5.3 Modeling Background

We will give a brief overview of the modeling approach, both the basic electrochemical model and the projection approach used to bridge repeated cap-cycles. The basic electrochemical model was based heavily on the work by Fabre et. al [14] which is similar to, and refers to, the work in [15, 16]. The particular model presentation here is taken from the our prior work [43], and a more complete description can be found there. The model represents a 1D lithium thin-film battery model with the spatial coordinate measured through the battery layers. The current balance in the battery is coupled with the electrochemical processes to determine the battery output. The diffusion of lithium in the positive electrode can be written:

$$\frac{\partial \mathbb{Y}_+}{\partial \mathbb{T}} = \frac{\partial}{\partial \mathbb{X}}\left(\mathbb{D}(\mathbb{Y}_+)\frac{\partial \mathbb{Y}_+}{\partial \mathbb{X}}\right) \tag{5.1}$$

$$\frac{\partial \mathbb{Y}_+}{\partial \mathbb{X}} = f_1(\mathbb{I})|\mathbb{X} = 0 \tag{5.2}$$

$$\frac{\partial \mathbb{Y}_+}{\partial \mathbb{X}} = 0|\mathbb{X} = 1 \tag{5.3}$$

where the double struck letters are nondimensional values: $\mathbb{Y}_+$, lithium concentration profile in the positive electrode, $\mathbb{T}$, time, $\mathbb{X}$, spatial coordinate in the positive electrode, and $\mathbb{I}$, current in

the battery. The positive electrode/electrolyte interface boundary condition is represented by the function f_1, and is current dependent.

Using the Butler-Volmer equation the internal voltages, $\mathbb{V}$, and the open circuit potential (OCV), $\mathbb{U}$, are related to currents at the positive electrode/electrolyte boundary by,

$$\mathbb{I} = f(\mathbb{Y}_e, \mathbb{Y}_+)\left[-\exp\left((\alpha_{a+} - 1) \times (\mathbb{V}_3 - \mathbb{V}_2 - \mathbb{U})\right)\right] \tag{5.4}$$

and the negative electrode electrolyte boundary by,

$$\mathbb{I} = g(\mathbb{Y}_e)\left[\exp(\alpha_{a-} \times -\mathbb{V}_1) - \exp\left((\alpha_{a-} - 1)\mathbb{V}_1\right)\right] \tag{5.5}$$

where *f* and *g* represent functions of the concentrations in the positive electrode and electrolyte, and α the charge transfer coefficient with subscripts denoting the positive or negative electrode. The internal currents are balanced with the boundary current. We approximate a constant resistance across the electrolyte, and zero voltage drops in the electrodes. For other details of the model see the prior work.

This model was shown to capture battery discharge dynamics for the chosen load reasonably [42] (see chapter 3). It will be important to note that, if the average current output of the battery is sufficiently small, concentration gradients in the positive electrode remain small. In that case the boundary concentration corresponds relatively well to the concentration throughout the electrode. In essence then, for low current loads it is possible to describe the concentration profile with a single number rather than a full profile. This can reduce the battery model to a variable voltage source (based on the OCV) and an internal resistance. However, as currents increase this simple model begins to fail and more involved modeling is needed. Using more developed models allows for greater scope of applicability but with the cost of complexity.

With the electrochemical modeling setup, we then incorporate losses and switching effects, as well as parasitic capacitance as seen in prior experimental work [41] (see chapter 2). The nature of the fast, cyclic loading creates dynamics at a very short timescale. However, fully modeling each cap-cycle is numerically expensive and this expense is compounded when analyzing over the long time period of the battery discharge. To help address this we presented a state projection modeling technique where system states (lithium concentration information) can be predicted over many cap-cycles. This is done through a transition matrix which represents the changes from one cap-cycle. If we approximate a near constant transition matrix, we can use this transition matrix to predict future states with reasonable accuracy [42, 43] (see chapters 3 and 4).

This can be described by letting $\mathbf{\Phi}_{\mathrm{i}}$ be the transition matrix of the concentration profile of cycle *i* to cycle *i*+1. We can then write the relationship:

$$\mathbb{Y}_{i+1} = \mathbf{\Phi}_{\mathrm{i}}\mathbb{Y}_i. \tag{5.6}$$

Approximating a constant transition matrix over m cycles we then have:

$$\mathbb{Y}_{i+m} = (\mathbf{\Phi}_i)^m\mathbb{Y}_i. \tag{5.7}$$

In this way we can model individual cap-cycles periodically and approximate changes in between. This modeling framework is presented and validated in our prior work [42, 43] (see chapters 3 and 4). Projection sizes are limited by the nonlinearities of the system.

5.4 Limitations

Before we explore applications of these techniques it should be noted that there are some limitations to the modeling and experimental data that have been addressed with our prior work:

- Limitations with the experimental data for calibration and validation are discussed in [41, 42] (see chapters 2 and 3). Because of these issues, the experimental data presented is used for modeling demonstration purposes rather than experimental result presentation.
- Limitations with the modeling approaches are discussed in [42, 43] (see chapters 3 and 4).
- Some algorithms such as those used for determining cap-cycle projection size and error may vary between case studies.
- Some modeling runs were aided by parallel processing.

5.5 Case Studies

For modeling of batteries with repeated fast dynamic loads, the projection concept described can be useful to reduce numerical costs. As stated above, in this paper we will explore two aspects of model implementation through a series of case studies. The order of these case studies is made to begin with demonstrating how average current impacts the need for detailed electrochemical modeling, or if more simplistic modeling is adequate. To do this we will first develop a simple battery model and describe calibration for the parameters. The first case study demonstrates a loading where the simple model adequately captures the dynamics, whereas the second case study presents more extreme load where the detailed model works well, but our

simple model has significant deviation. After addressing current loading, the third and fourth case studies explore different design characteristics that can be captured through this modeling. The third approximates batteries in series to achieve higher load voltages, as well as showing targeted analysis of a particular switching loss. The fourth approximates batteries in parallel and examines a different load circuit, boost converter.

5.5.1 Simple Model Formulation and Calibration

For mild average current loads on batteries, a reasonable approximation of the electrochemistry is a simple variable voltage source, based on the OCV, and an internal resistance. This model approximates the electrochemistry in a very simplistic way, yet can be adequate for low average current loads where the lithium concentration profile in the positive electrode remains fairly uniform.

To calibrate this "simple model," we used the same calibration method as used for the detailed model reported in [42] (see chapter 3). This combined fitting of complete battery discharges at several current levels and fast dynamic fitting of a single early cap-cycle. These two datasets were chosen to help fit both slow and fast dynamic responses in the battery. The parameters fit for the simple model were internal resistance, a parameter for losses in the switching, and the battery parasitic capacitance. The overall capacity of the battery was taken from the detailed model calibration.

Using this method we obtained comparable detailed and simple models. The calibration fitting of the detailed model from [42] (see chapter 3) and simple model are shown in Figure 5.1 and Figure 5.2. Figure 5.1 shows fitting of constant current profiles for various current levels. Both models have difficulties matching initial voltage drops at very high currents, but for currents at least up to 1C (perhaps beyond) the detailed model is still able to capture these voltage drops where the simple model degrades earlier.

Additionally, there is no mechanism to capture lost capacity at higher currents in the simple model, so all current levels produce the same output capacity, whereas the detailed model fitting matches capacities reasonable well at least up to 4C discharge rates. It is important to acknowledge there are various levels of modeling for batteries, and other modeling approaches categorized between the two presented here definitely exist.

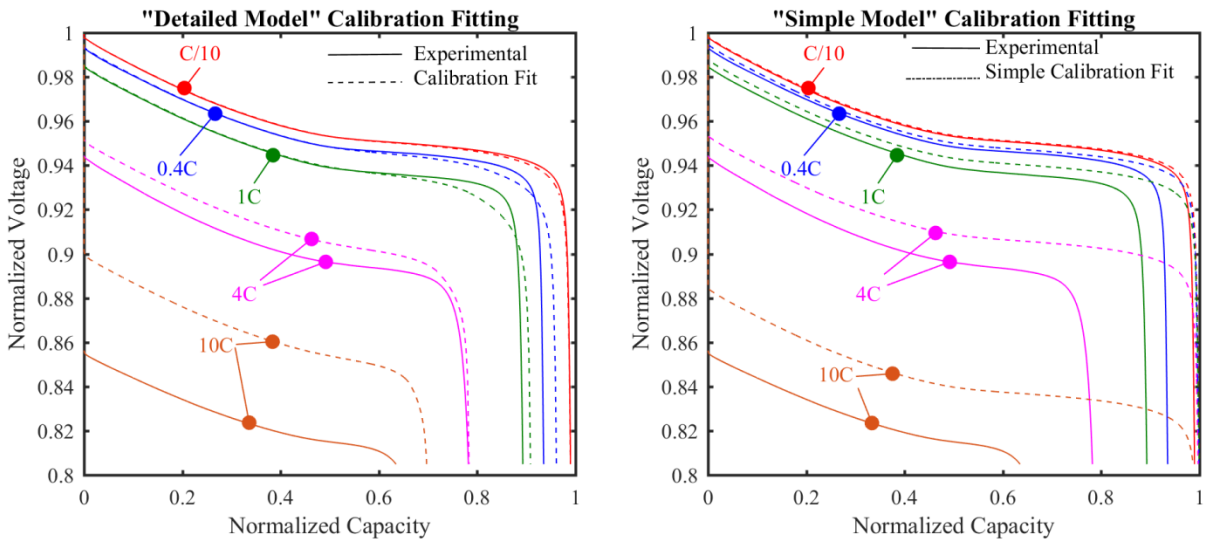

Figure 5.1 Calibration fitting constant current. (Left) Calibration fitting from detailed model calibration modified from [42] (see chapter 3). (Right) Simple model calibration fitting.

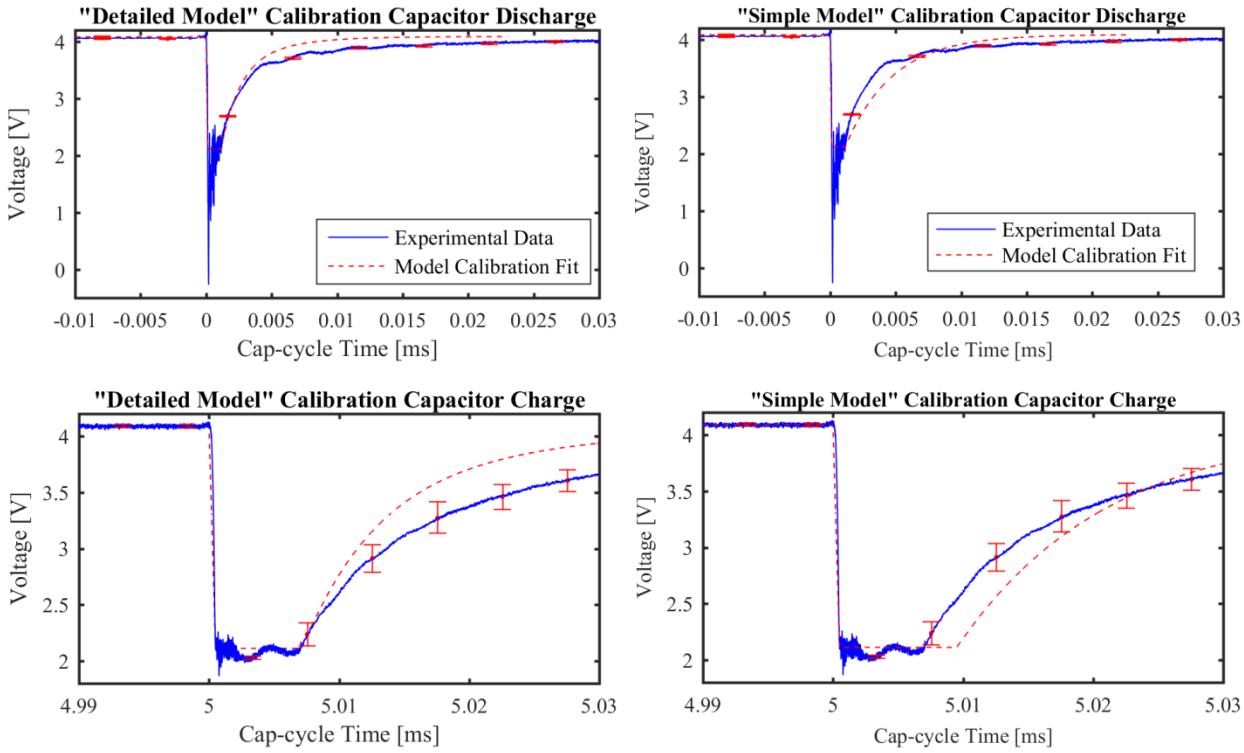

Figure 5.2 Calibration fitting constant current. (Left) Calibration fitting from detailed model calibration modified from [42] (see chapter 3). (Right) Simple model calibration fitting.

However, here we present these particular examples for demonstration of the modeling techniques mentioned, and the contrast the simple model selected gives is considered adequate.

Future work can be done to explore model reduction of the detailed model that could optimize numerical expense.

In addition to constant current profiles fitting, calibration also included a set of cap-cycle charge/discharge dynamics as shown in Figure 5.2. Due to the reduced number of fitting parameters in the simple model it is not possible to fit the fast dynamics and the voltage drops in the constant current runs as well as the detailed model. For the calibration of the simple model here, higher priority was given to the constant current fitting, but other weightings could be done.

The simple electrochemical model, although reducing numerical expense, does not inherently eliminate the timescale issues discussed. These are addressed in a similar manner to the detailed model, where system states are projected over many cap-cycles. However, with the simple model, instead of having the system states represented by the lithium concentration information in the positive electrode, needing to be solved using the diffusion equation, the Butler-Volmer equation, and the electrolyte ionic resistance, the states of the simple model come down to a single state, capacity, and the transition matrix equivalent is the capacity loss per cap-cycle. Assuming this capacity loss per cap-cycle from the battery as constant over some period, we can then project over many cap-cycles the loss in the same way the transition matrix is used for the detailed model. Using the calibrated parameters and projection method for the simple model we can now examine the four case studies.

5.5.2 Case Study 1: Capacitive Load, Low Current

As stated there are two main objectives for presenting these case studies. Through this first case study we see how simplistic models can be used with particular loads with similar fidelity to more detailed modeling. In our prior work we used a light average current to demonstrate and validate the modeling techniques described above [42, 43] (see chapters 3 and 4). The electrical configuration was a capacitor loaded directly from the battery through a switching circuit. The losses in the circuit were not optimized physically, but were captured in the model. For demonstration we used a switching frequency of 100Hz and a load capacitor of 10nF, which resulted in an average modeled current of about 15.2μA or 0.3C. This type of load was used to imitate a capacitive load that might be seen in MEMS actuation and microrobotic settings, although the battery modeled would be too large physically for the robot in the current configuration. This loading worked well for the demonstration of the projection approaches developed; however, it was not sufficient to demonstrate the range of the detailed

electrochemical model involved. To illustrate this we present the battery discharge profile from [42] (see chapter 3) in Figure 5.3.

This shows validation data and model data as voltages at the beginning of various cap-cycles throughout the battery discharge. In addition the simple battery model was run with the same load and significantly reduced numerical expense.

As can be seen in the figure there is reasonable good fit for both models. The detailed model shows an error of approximately 1.4% in the overall number of cycles possible from the battery, and the simple model is also only approximately 3.4% error. However, the energy transferred to the capacitor had a more significant difference being around 9.2% different between the detailed and simple models. Here we can see that although the detailed model can capture the discharge profile of the battery, a more numerically economical way is to use the simple model.

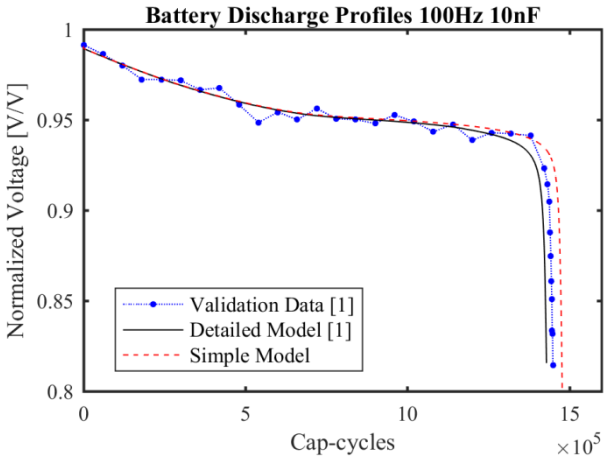

Figure 5.3 Battery discharge profile for detailed and simple models 10nF capacitor cycled at 100Hz. Adapted from [42] (see chapter 3).

5.5.3 Case Study 2: Capacitive Load, High Current

Case 1 raises the question: "When, if ever, is more detailed modeling needed?" The answer is in part demonstrated through the second case study. Here we have a loading condition very similar to case 1; however, the loading frequency is increased by an order of magnitude, from 100Hz to 1kHz. This consequently raises the average current seen by the battery. The battery discharge profile is presented in Figure 5.4. Here we see that at this elevated average current load (69μA or 1.4C based on the detailed model) the detailed model still adequately captures the overall discharge of the battery with an approximate error of 1.7%, and the simple model begins to deviate significantly with an approximate error of 10.9%. Energy transferred to the capacitor differed by over 17% between the two models. It should be noted here that although the detailed

model matches well for this loading, there are approximations in it that will break down at even higher loads. The model could likely then be adapted to address those limitations, but probably at the cost of greater complexity.

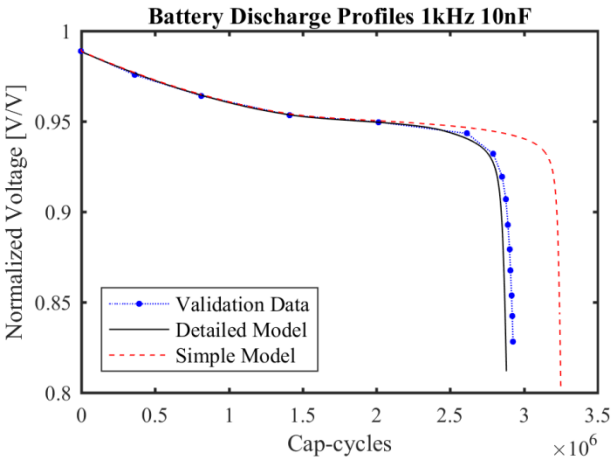

Figure 5.4 Battery discharge profile for the detailed and simple models for a 10nF capacitor cycled at 1kHz.

5.5.4 Case Study 3: Batteries in Series

Having demonstrated that detailed modeling differs from the simplistic model at higher average current levels, we now can use the detailed model to demonstrate potential design analysis approaches that would be unobtainable with our presented simple model. For the third case study we analyze batteries in series to obtain higher voltages, as needed in the microrobotic application mentioned above.

The load setup in similar to before; however, we concentrate our analysis on one type of switching loss (a loss of the parasitic charge for each cap-charge and cap-discharge switch) and remove the majority of other losses from the switching circuit (e.g. leakage) as well as set the switching threshold voltage to zero. For complete analysis the additional losses can be incorporated.

In an ideal series configuration of batteries (stack), each battery experiences the same voltage drop and current flow. In actuality there can be variations and imperfections in individual batteries causing imbalances in the stack. This will depend on the individual batteries used and how they degrade over time. An example where this had a critical effect was in experimental testing by Jones and Akridge who reported a series of five thin-film batteries that showed only 70% cathode efficiency, which they supposed was due to a marginal cell in the stack [70]. For the present analysis these variation effects are neglected.

If we take n batteries in series, the total voltage of the stack will be $n\mathrm{V_B}$, where $\mathrm{V_B}$ is the voltage of a single battery, and this stack voltage will be equal to the voltage on the load capacitor $\mathrm{V_{CL,}}$ neglecting line and switch resistances. Each battery in the stack experiences the same current flow i_B which is equal to the current into the load capacitor i_{CL}. Putting these together we see that:

$$i_B = i_{C_L} = C_L \frac{dV_{C_L}}{dt} = C_L \frac{d(nV_B)}{dt} = nC_L \frac{dV_B}{dt} \tag{5.8}$$

and therefore we can mimic the stack current flow to a capacitor by modeling one battery loaded with a capacitor with capacitance proportional to the number of batteries in the original stack as shown schematically in Figure 5.5. Using this approach we are able to merely adjust the load capacitor size in the model to approximate different series configurations.

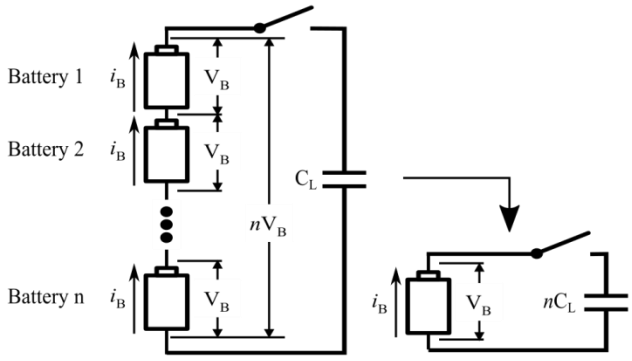

Figure 5.5 Schematic representation of approximating batteries in series.

After each simulation we can adjust the voltage data appropriately to get the stack voltages. In determining energy transferred from the battery stack to the load capacitor we need to look at the associated equation and perform similar steps as before:

$$E_{B\to C_L} = \frac{1}{2} C_L V_{C_L}^2 = \frac{1}{2} C_L (nV_B)^2 = n\left(\frac{1}{2} nC_L (V_B)^2\right) \tag{5.9}$$

with $E_{B\to C_L}$ as the energy transferred from the battery stack to the load capacitor. Thus we see that when calculating the energy transfer we need to multiple the energy calculated by the battery model, by the number of batteries in the stack to get the total energy. One final consideration that needs to be taken is for the parasitic capacitance. Since it, like the load capacitor, will be charged to a higher voltage we would need to multiple the parasitic capacitance by the number of batteries in the stack. However, the parasitic capacitance of each battery is in series so the total is divided by the number of batteries, and in the end these two factors offset.

This process was applied and the detailed model was run for a single battery and two, three, and four batteries in series. The battery discharges curves are shown in Figure 5.6. These behave similarly to what would be expected, however, it would also be of interest to know the energy transferred to the capacitor in each configuration. In Figure 5.7 we show the energy transferred to the load capacitor. The energy is normalized to the energy transferred in the single battery configuration. Both the total energy from the stack, and a per battery energy are shown.

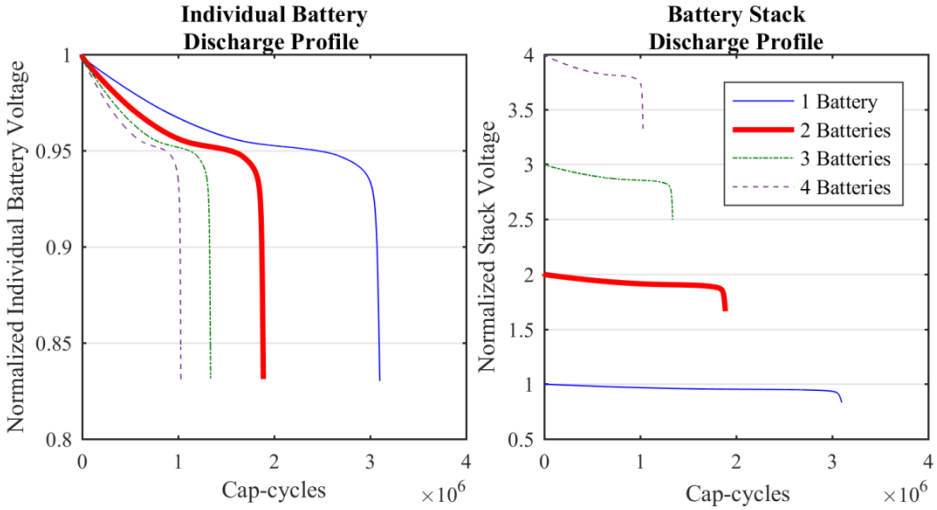

Figure 5.6 Battery discharge curves for batteries in series. (Left) individual battery discharge profiles. (Right) Stack discharge profile.

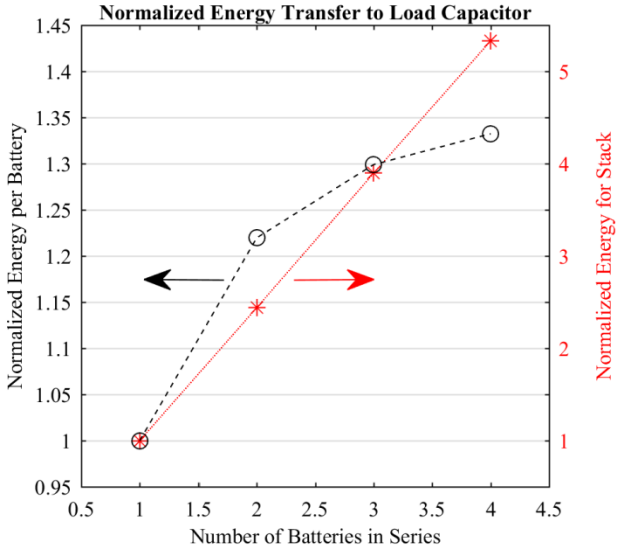

Figure 5.7 Energy transferred to load capacitor in various series configurations.

It can be seen that more energy per battery is delivered as the number of batteries increases. This is likely due in part to the loss that we included in our modeling of the parasitic capacitance. Because the parasitic capacitances are in series yet are charged to higher voltages, the energy lost

remains constant per switch regardless of the number of batteries. As the number of batteries increases this becomes smaller and smaller compared to the charging loss. Figure 5.8 shows the entire battery discharge curve again with a comparison to the simple model.

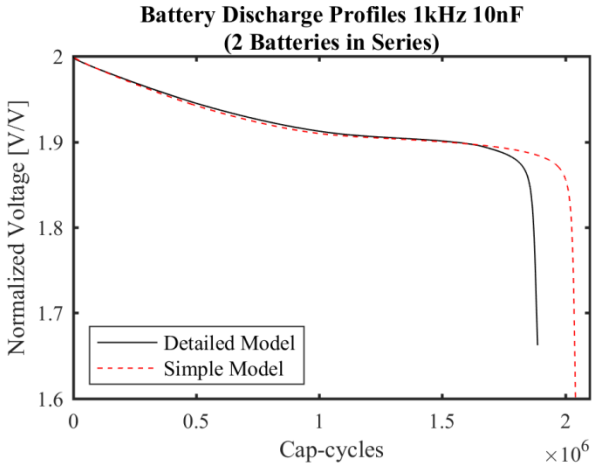

Figure 5.8 Two batteries in series discharge profile with detailed and simple models for a 10nF capacitor cycled at 1kHz.

5.5.5 Case Study 4: Batteries in Parallel, Boost Converter

The final case study that we present is an idealized parallel configuration. Just as with batteries in series, a marginal cell in a parallel configuration has adverse effects on overall performance; however, again these would be based on the individual batteries used and are not considered here. Ideally treating batteries in parallel is comparable to simulation of batteries with increased active surface area. Therefore, these effects might be able to be accomplished using 3D structures or perhaps nanomaterials or treatments [7, 71].

The parallel configuration allows us to achieve higher current draws from the battery pack. We couple this with a boost converter circuit to achieve elevated voltages comparable to the series configuration. The implementation of the circuit is not ideal in that a very low duty cycle and low boost frequency was used to keep the current draw and numerical expenses reasonable. The circuit is shown in Figure 5.9 and is one way to achieve these higher voltages.

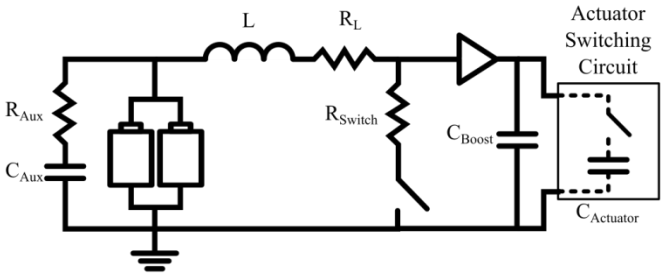

Figure 5.9 Boost converter schematic

Another notable example would be a switched capacitor circuit. The components variables shown are the inductor, L, inductor resistance, R_L, auxiliary capacitor and resistance, C_{Aux} and R_{Aux}, boost capacitor, C_{Boost}, and actuator capacitance $C_{Actuator}$, with the values selected shown in Table 5.1. The losses then that are modeled are losses from charging the actuator from the boost capacitor, losses in the battery, losses in the diode, and other losses associated with the load capacitor. Additionally minor resistive losses in the inductor, switch, and auxiliary capacitor are modeled. The majority of the switching losses were not modeled, both in the boost converter, and in the actuation circuit, but could be added for a full analysis.

Table 5.1 Boost converter circuit parameters

Component	Value
Inductor (L)	90μH
Inductor Resistance (R_L)	1Ω
Auxiliary Capacitor (C_{Aux})	100nF
Auxiliary Resistor (R_{Aux})	1Ω
Boost Capacitor (C_{Boost})	100nF
Duty Cycle	0.97%
Boost Switching Frequency	20kHz
Actuator Capacitance ($C_{Actuator}$)	10nF
Actuator Switching Frequency	1kHz
Diode I_s	1e-14A

The simulation was started with the boost and auxiliary capacitors charged to minimize transience. A similar approach was used with this simulation as with the prior simulations. A complete cycle of the actuator charge was simulated (this incorporated 20 switching cycles of the boost convertor). At this time the charge needed to charge the actuator was reduced from the boost capacitor thus dropping equalizing their voltages. This can be written as:

$$V_{C_{Boost}}^{+} = V_{C_{Boost}}^{-}\left(\frac{C_{Boost}}{C_{Boost} + C_{Actuator}}\right)$$

where $V_{C_{Boost}}^{+}$ is the boost capacitor voltage after actuator charge, $V_{C_{Boost}}^{-}$ is before actuator charge and $C_{Actuator}$ is the actuator capacitance. Each actuator charging cycle is comparable to the cap-cycles from previous modeling. This requires more numerical expense in that 20 boost converter switches must be modeled for a cap-cycle and thus to develop the transition matrix. Ways to address this expense will be discussed later.

Both detailed and simple battery models were loaded with the boost converter circuit. A combination of Matlab script and Simulink were used for the boost converter simulation. All other simulations previously were run solely in Matlab. The battery discharge profiles are shown in Figure 5.10. Additionally, the energy losses were determined and are shown in Figure 5.11. This figure also shows how energy losses are distributed among various sources, including losses in the diode, losses in the battery, and energy used in capacitor charging. Also noted is a mismatch between cumulative energy calculated, denoted as modeling error.

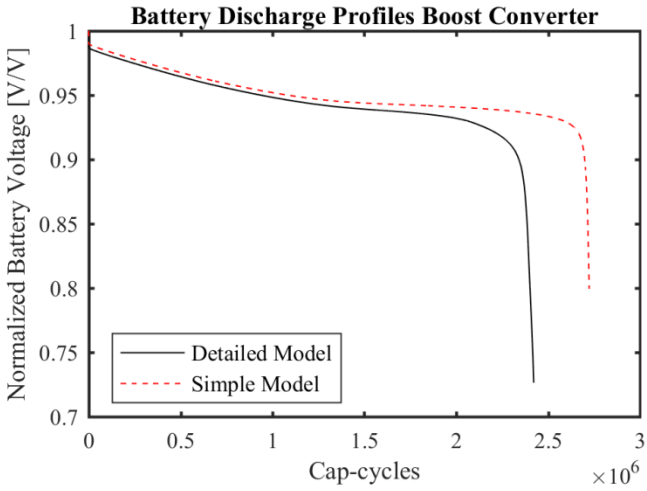

Figure 5.10 Boost converter circuit battery discharge profile with detailed and simple models.

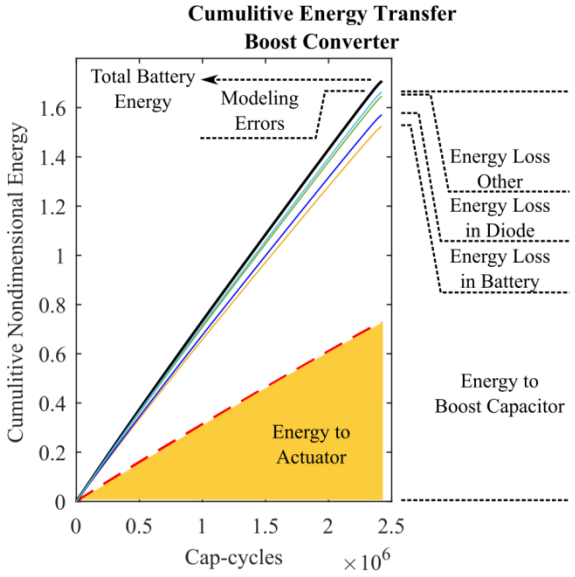

Figure 5.11 Energy losses and allocations from battery driven boost converter circuit. (Energy normalization was adjusted to correlate with those from Case 3).

The overall energies did not match exactly, likely due to modeling implementation (such as backward difference used in integration in the Simulink model), and this is noted in the plot. One source of error was in modeling of the inductor, which did not show 0 energy loss. Energy to the actuator as noted is the energy transferred to the actuator from the boost capacitor. Other losses of note are those associated with the boost capacitor, diode and internal battery losses.

This scenario is instructive for several reasons. First, it demonstrates another circuit loading being analyzed using these modeling techniques besides the switching load first used. Second, this lays a foundation for additional work in dual projection applications. The numerical expense of doing all 20 switches of the boost converter is significant in this scenario. For ideal settings, the boost converter would likely switch many more times than 20 between each actuation event. If a similar projection approach could be used across boost cycles as is used across actuation cycles, then potentially significant gains could be made. Third, although the comparison between case study three and four is not perfect it allows us to hypothetically compare the number of actuation cycles between different battery configurations for elevated voltages. If the data presented here was considered to capture adequately the losses, then we could conclude the boost converter had superior performance as seen in Figure 5.12. Using this, it would be possible to have a more extensive understanding of tradeoffs in design such as added weight of the inductor compared to the increased number of actuation cycles.

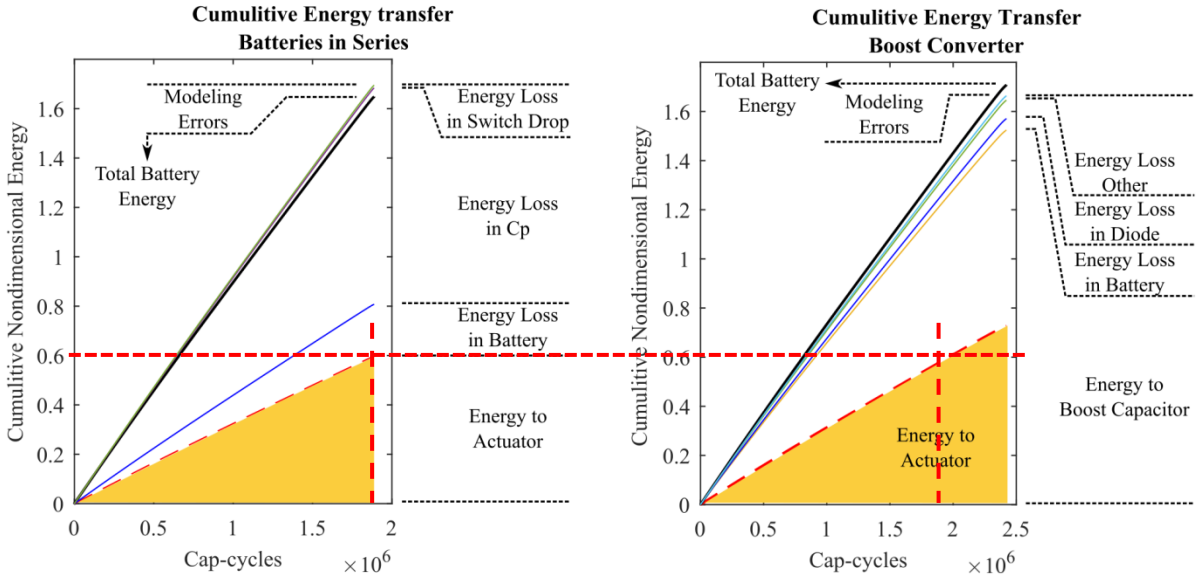

Figure 5.12 Comparison of energy distribution in case studies 3 and 4. (Energy normalization was adjusted for case 4 to correlate with those from Case 3). Dashed red lines show approximate comparisons between the plots. (Right) Cp denotes the parasitic capacitance. An additional minor switching loss that was incorporated is shown as energy loss in switch drop.

5.5.6 Case Study Comparison

A brief comparison of the different case studies is informative. In Table 5.2 we show function call times for each of case study. This time is based on a dual core computer, but highlights the expense difference between models. The large time for the detailed model in case study 4 is due in part to the increased data storage required by the boost converter cycles. Overall simulation time will depend on parallel implementations and hardware. Additionally, average currents are shown. It should be noted that validation data was only shown up to the detailed model current in case study 2 and further validation is needed to properly verify model accuracy for the higher currents in other scenarios.

Table 5.2 Function call and average current comparisons across case studies.

	Case Study 1 100Hz 1nF		Case Study 2 1kHz 1nF		Case Study 3 x2 Battery Series		Case Study 4 Boost Converter	
	Simple	Detailed	Simple	Detailed	Simple	Detailed	Simple	Detailed
Function Call Time [s]	1.6	7.2	1.3	5.1	1.1	4.2	1.2	51.2
Average Current [μA]	16.2	15.2	73.8	69	117.5	109.1	176.1	175.4

5.6 Conclusions

Here we have explored several key case studies implementing previously developed modeling techniques. These scenarios have demonstrated detailed modeling under certain loading conditions. Additionally, we have seen how various battery configurations can be analyzed, capturing fine details over long periods of time. Finally we have seen how different circuits might be implemented. Using these case studies as a template, these modeling techniques can be used as design tools. Further work could be done to understand the level of modeling needed at various current levels, but here we focused on presenting implementation of these specific techniques. Future work could also be to look at hybrid models that incorporate the projection approach but that take advantage of model simplifications where possible. Additional if higher currents are further explored, additional model validation and potentially adaptation will be needed.

CHAPTER 6 CONCLUSIONS

6.1 Summary

In this thesis we have explored many aspects and effects of fast, repeated, dynamic loads on thin-film batteries. These loads have specific application in MEMS microrobotics, but it is hoped that these methods would be useful beyond that area.

In Chapter 2 we presented experimental findings showing how repeated capacitive loads on thin-film batteries, coupled with the switching dynamics and losses, caused marked changes in battery discharge over a range of different loading parameters. Additionally, we observed parasitic capacitance effects in the battery, although the exact source was not determined. A Cymbet™ [46] 50μAh battery was used for these tests.

In Chapter 3 we used these experimental results to model the dynamics over complete battery discharge for a set loading condition. In order to do this we needed to address issues of timescales. The switching dynamics were extremely fast, on the order of microseconds, where the full discharge of the battery was on the order of hours. This disparity was bridged using a transition matrix approach. This transition matrix was developed to describe the changes in battery states (lithium concentration information) for a single capacitive load or cap-cycle. Using the approximation that over a certain number of cap-cycles this transition matrix was constant, system states could be predicted several cap-cycles into the future. This approach was able to achieve significant numerical cost reduction over full modeling.

In Chapter 4 we built on the model presented in Chapter 3. This was done in two significant ways. First, a different system state definition was chosen that allowed direct development of the transition matrix (the approach in Chapter 3 required perturbation of each state, which could prove to be a significant numerical expense depending on computing hardware). Second, an error analysis was performed of the projection approximations. In this way we were able to determine the extent of certain sources of error and adjust the projection approach of the system states to reduce this error.

In Chapter 5 we explored several case studies that helped in understanding and demonstrating these modeling techniques. In particular we addressed average current levels and how at higher average currents, simple modeling begins to degrade. We also demonstrated implementation of these approaches in a battery series configuration as well as a boost converter circuit loading. Each scenario enabled better understanding of the modeling implementation.

6.2 Implications

In regards to the microrobotics application discussed throughout this thesis, there are several aspects of the work presented that give insight on potential design decisions. One will be highlighted here as an example. Chapter 2 provided key insights into losses and parasitics. Coupling these with the case studies in Chapter 5 suggest that care needs to be taken in regards to these losses. One particular aspect is the losses associated with charging of a capacitor that come into play not only in the charging of the actuator, but also in charging of the parasitic capacitance. For example, in the boost converter, the battery voltage is steadier than in the switching capacitors (where the battery voltage is pulled down to the switching threshold voltage each switch) so the parasitic capacitor does not need to be constantly charged, whereas if the battery voltage has a significant range each loading event then the parasitic capacitance is constantly being charged and discharged. If this charge is lost in switching, then this issue is amplified. This could be addressed by having a more constant loading on the battery that distributes the loading to the battery through circuitry. Further investigation of the source of the parasitic capacitance may be needed to determine if other approaches can reduce this loss. This may be a limiting factor in the ability to apply pulsed loads that create significant voltage changes across the battery, at least if significant parasitics exist.

6.3 Contributions

This information together is hoped to help further research in areas such as MEMS microrobotics where battery energy is premium due to size and weight requirements. The modeling techniques presented here should be tools that can aid in this research.

The main contributions from this work include:

1) Experimentally observed of characteristics of switching loads on thin-film batteries,
2) Augmented existing thin-film battery models to explore fast cyclic dynamic loads on thin-film batteries,

3) Addressed modeling of dynamics in these systems with disparate timescales through a transition matrix approach,
4) Addressed numerical cost in transition matrix approach by changing system state definitions,
5) Performed error analysis on projection approach that enabled targeted error reduction,
6) Provided several scenarios to demonstrate the use of these techniques, and their relation to autonomous MEMS systems.

Additionally in the course of this work there have been several lessons learned that would be good to document

1) Modeling Nondimensionalization: In modeling these battery systems, we chose to nondimensionalized the problem. This became valuable for a variety of reasons. First, the difference in scale were more readily handled (cross-sectional areas in cm^2 and thicknesses in μm). Second, calibration and fitting was able to be done with slightly fewer parameters. Third, comparison between scenarios can become easier as you work from a common benchmark. However, nondimensionalization does have the drawback that the numbers lose familiarity (such as 4V on a battery).
2) Comparison Measurements. As with any study, the key measurement for comparison is important. Throughout this work, we have used primarily the number of cap-cycles the battery was able to perform as a figure of merit. However, other values may have been more insightful such as energy, as introduced in Chapter 5.
3) Multiple Timescales: The way we use the term multiple timescales throughout this thesis may not be strictly traditional. If fast dynamic event are occurring with no time between, then the timescale may very well be just the fast one. However, accumulated effects from individual loads have long term changes, and is where we consider the multiple timescales.
4) State Definitions: When projecting states over multiple loading events, the definition of the states is important. In this work we used mainly information about the lithium concentration profile. In general we would use the voltages of the battery before the projection, with the new concentrations, for continued modeling after the projection. In reality the voltages of the battery should likely be considered states as well and potentially other aspects of the model. In Chapter 4 we address this in part by updating

the voltages during the projection occasionally. Further work looking at this could be done. This ties closely with the issue of circuit states. With the switched charging of a capacitor, the capacitor was fully discharged before charging again. This allowed for a set loading condition after each cap-cycle. However, with a circuit like the boost converter, the circuit states may not be as easy to approximate, and may need to be projected forward just as the battery states are. In Chapter 5 we minimized this by using a full actuator charge/discharge for one "cap-cycle," and started the circuit in a preloaded state. Additionally, the inductor loading was not ideal for actual implementation, but chosen to aid in model demonstration. Issues like these would be important to address for further understanding of the potential for these techniques.

5) Relaxing Effects of Batteries: One issue that had to be addressed is that even after a capacitor is "fully" charged by the battery and the next switching cycle has not happened, there is still a voltage rise in the battery as the lithium in the electrode diffuses to an equilibrium (which likely would not happen before the next loading in a realistic setting).
6) Model Order: One issue that was encountered with the boost converter modeling is in the order and differentiation approach of the battery and circuit. The battery model was a second order Crank-Nicholson approach, but the circuit was a backwards differentiation. In the future, this could be improved for accuracy. This ties into the need for proper meshing of the models, in time and space, both of which likely will be non-uniform to improve numerical performance.

6.4 Future Work

6.4.1 Reduced/Hybrid Models

The modeling approach presented in this thesis uses a fairly detailed electrochemical model to determine the lithium concentration profile in the positive electrode. This modeling detail comes with numerical cost. Future work needs to be done to properly determine when this depth of modeling is needed and when more simplistic models can be used. Conversely there are certain assumptions in this model that may need to be addressed if even higher current levels are desired (e.g. zero potential drop in the positive electrode and constant electrolyte conductivity).

It is likely that a combination of approaches will give the best numerical cost results. That is, it may be that occasional detailed modeling with a high fidelity model is needed during periods

of high nonlinearities, but for other portions, or in between times, a simpler model could be used. In a sense the projection method presented here is in fact a hybrid model, and additional combinations of such approaches may be advantageous.

6.4.2 Microrobotic Applications

The primary purpose for this research was for help in determining the design and drive parameters for microrobotics. A framework is laid with the modeling presented that could be used to address design decisions for such microrobots, a few examples will be illustrative. First, we have shown in Chapter 5 how different drive circuits can be analyzed to determine the most efficient drive circuit when utilization of the battery is considered. This could be implemented with a variety of different scenarios, and with detailed losses incorporated. Studies could be done that would investigate both different circuits as well as different configurations of a given circuit. From this, one could gain understanding how the battery model affects circuit design decisions. Additionally, the locomotion parameters such as gait could also be explored. Some work would need to be done to determine consistent comparison standards between the results.

6.4.3 Dual Projection

As was discussed in Chapter 5, occasionally there are more than two timescales, such as in the boost converter. In that situation there were multiple switches in the boost converter for each actuator charge. If the projection approach could be applied over multiple switches in the boost converter, and over multiple actuator switches, potentially significant savings could be made. One issue that would likely need to be addressed is the circuit states over the projections. If at the end of each cycle the circuit comes back to a known state then starting the next cycle after the projection can be approximated fairly easily, however, if the circuit also has states that are changing, then these need to be resolved in some way. One solution would be in projecting the circuit states in parallel with the battery states.

6.4.4 Other Applications and Model Improvements

These techniques may also be able to be applied to other systems beyond what has been looked at in this thesis. This may include other applications where fast dynamic loads cause incremental changes to the system. Since the projected states are based off of the diffusion

equation, other systems based on the diffusion or heat equations with dynamic boundary conditions may be good candidates.

Additional work ought to be done to understand numerical errors in this model, as well as optimization of meshing. Improving the calibration approach would also be advantageous, especially if parameter extraction is to be done. It would also be informative to compare the calibration against known battery parameters, as the actual parameters of the batteries in this work were not precisely known. This may lead to adaptations to the model and or calibration to better fit specified physical data. Further investigation of the parasitic capacitance will also be important. Determination of the sources (e.g. battery, packaging, circuit, etc.) and magnitudes of these parasitics will aid in future design decisions. Ultimately, determination of the depth of modeling required to achieve the needed precision for the given task will decide those situations in which the modeling presented here is best in the form presented, or if alternative modeling and adaptations will be advantageous.

BIBLIOGRAPHY

[1] M. Armand and J. Tarascon, "Building better batteries," *Nature,* vol. 451, no. 7179, pp. 652-657, 2008.

[2] M. Ghaed *et al.*, "Circuits for a cubic-millimeter energy-autonomous wireless intraocular pressure monitor," *IEEE Transactions on Circuits and Systems I-Regular Papers,* vol. 60, no. 12, pp. 3152-3162, 2013.

[3] B. Edamana and K. Oldham, "Optimal low-power piezoelectric actuator control with charge recovery for a microrobotic leg," *IEEE-ASME Transactions on Mechatronics,* vol. 18, no. 1, pp. 251-262, 2013.

[4] E. Erdem *et al.*, "Thermally actuated omnidirectional walking microrobot," *Journal of Microelectromechanical Systems,* vol. 19, no. 3, pp. 433-442, 2010.

[5] X. B. Zhang, J. Zhao, Q. Zhu, N. Chen, M. W. Zhang, and Q. M. Pan, "Bioinspired aquatic microrobot capable of walking on water surface like a water strider," *ACS Applied Materials and Interfaces,* vol. 3, no. 7, pp. 2630-2636, 2011.

[6] K. Takada, "Progress and prospective of solid-state lithium batteries," *Acta Materialia,* vol. 61, no. 3, pp. 759-770, 2013.

[7] J. Oudenhoven, L. Baggetto, and P. Notten, "All-solid-state Lithium-ion microbatteries: A review of various three-dimensional concepts," *Advanced Energy Materials,* vol. 1, no. 1, pp. 10-33, 2011.

[8] A. Patil, V. Patil, D. Shin, J. Choi, D. Paik, and S. Yoon, "Issue and challenges facing rechargeable thin film lithium batteries," *Materials Research Bulletin,* vol. 43, no. 8-9, pp. 1913-1942, 2008.

[9] J. Randles, "Kinetics of rapid electrode reactions," *Discussions of the Faraday Society,* vol. 1, pp. 11-19, 1947.

[10] S. Abu-Sharkh and D. Doerffel, "Rapid test and non-linear model characterisation of solid-state lithium-ion batteries," *Journal of Power Sources,* vol. 130, no. 1-2, pp. 266-274, 2004.

[11] J. Gomez, R. Nelson, E. Kalu, M. Weatherspoon, and J. Zheng, "Equivalent circuit model parameters of a high-power Li-ion battery: Thermal and state of charge effects," *Journal of Power Sources,* vol. 196, no. 10, pp. 4826-4831, 2011.

[12] M. Greenleaf, H. Li, and J. Zheng, "Application of physical electric circuit modeling to characterize Li-ion battery electrochemical processes," *Journal of Power Sources,* vol. 270, pp. 113-120, 2014.

[13] S. Li, B. Wang, H. Peng, and X. Hu, "An electrochemistry-based impedance model for lithium-ion batteries," *Journal of Power Sources,* vol. 258, pp. 9-18, 2014.

[14] S. Fabre, D. Guy-Bouyssou, P. Bouillon, F. Le Cras, and C. Delacourt, "Charge/discharge simulation of an all-solid-state thin-film battery using a one-dimensional model," *Journal of the Electrochemical Society,* vol. 159, no. 2, pp. A104-A115, 2012.

[15] D. Danilov, R. Niessen, and P. Notten, "Modeling all-solid-state Li-ion batteries," *Journal of the Electrochemical Society,* vol. 158, no. 3, pp. A215-A222, 2011.

[16] K. E. Thomas, J. Newman, and R. Darling, "Mathematical modeling of Lithium batteries," in *Advances in Lithium-ion Batteries,* W. van Schalkwijk and B. Scrosati, Eds. New York, NY: Kluwer Academic/Plenum Publishers, 2002, p. 362.

[17] S. Rahimian, S. Rayman, and R. White, "Extension of physics-based single particle model for higher charge-discharge rates," *Journal of Power Sources,* vol. 224, pp. 180-194, 2013.

[18] M. Baba, N. Kumagai, H. Kobayashi, O. Nakano, and K. Nishidate, "Fabrication and electrochemical characteristics of all- solid-state lithium-ion batteries using V2O5 thin films for both electrodes," *Electrochemical and Solid State Letters,* vol. 2, no. 7, pp. 320-322, 1999.

[19] F. Savoye, P. Venet, M. Millet, and J. Groot, "Impact of periodic current pulses on Li-ion battery performance," *IEEE Transactions on Industrial Electronics,* vol. 59, no. 9, pp. 3481-3488, 2012.

[20] L. M. Feeney, C. Rohner, P. Gunningberg, A. Lindgren, and L. Andersson, "How do the dynamics of battery discharge affect sensor lifetime?," in *Wireless On-demand Network Systems and Services (WONS),* 2014, pp. 49-56.

[21] S. Park, A. Savvides, M. Srivastava, and ACM, "Battery capacity measurement and analysis using lithium coin cell battery," in *International Symposium on Lowpower Electronics and Design (ISLPED),* 2001, pp. 382-387.

[22] S. Castillo *et al.*, "Experimental analysis of batteries under continuous and intermittent operations," in *International Conference on Embedded Systems and Applications (ESA)*, 2004, pp. 18-24.

[23] D. Bell, T. Lu, N. Fleck, and S. Spearing, "MEMS actuators and sensors: observations on their performance and selection for purpose," *Journal of Micromechanics and Microengineering*, vol. 15, no. 7, pp. S153-S164, 2005.

[24] K. Salloux, J. Lim, B. Dunn, P. Chaplya, and G. Carman, "Rechargeable lithium batteries for powering piezoelectric devices," *Journal of Intelligent Material Systems and Structures*, vol. 11, no. 12, pp. 930-935, 2000.

[25] C. Engstler and C. Lubich, "Multirate extrapolation methods for differential equations with different time scales," *Computing*, vol. 58, no. 2, pp. 173-185, 1997 1997.

[26] E. Constantinescu and A. Sandu, "Extrapolated Multirate Methods for Differential Equations with Multiple Time Scales," *Journal of Scientific Computing*, vol. 56, no. 1, pp. 28-44, 2013.

[27] J. Roychowdhury, "Analyzing circuits with widely separated time scales using numerical PDE methods," *IEEE Transactions on Circuits and Systems I-Fundamental Theory and Applications*, vol. 48, no. 5, pp. 578-594, 2001.

[28] D. A. Edwards, "An Alternative Example of the Method of Multiple Scales," *SIAM Review*, vol. 42, no. 2, pp. 317-332, 2000.

[29] C. Kuehn, *Multiple Time Scale Dynamics*. Springer International Publishing, 2015.

[30] S. Santhanagopalan, Q. Guo, P. Ramadass, and R. White, "Review of models for predicting the cycling performance of lithium ion batteries," *Journal of Power Sources*, vol. 156, no. 2, pp. 620-628, 2006.

[31] T. Kim and W. Qiao, "A Hybrid Battery Model Capable of Capturing Dynamic Circuit Characteristics and Nonlinear Capacity Effects," *IEEE Transactions on Energy Conversion*, vol. 26, no. 4, pp. 1172-1180, 2011.

[32] L. Gao, S. Liu, and R. Dougal, "Dynamic lithium-ion battery model for system simulation," *IEEE Transactions on Components and Packaging Technologies*, vol. 25, no. 3, pp. 495-505, 2002.

[33] S. Afshar, Kirsten and A. Khajepour, "Fully dynamical representation of a LFP battery cell," American Control Conference (ACC), 2017.

[34] K. Oldham, C. Rhee, J. Ryou, R. Polcawich, and J. Pulskamp, "Lateral thin-film piezoelectric actuators for bio-inspired micro-robotic locomotion," in *ASME International Design Engineering Technical Conferences (IDETC)*, 2009, pp. 759-768.

[35] J. Ryou and K. Oldham, "Simulation study and experimental testing of foot-terrain dynamics in piezoelectric micro-robots," in *ASME Dynamic Systems and Control Conference (DSCC)*, 2010, vol. 2, pp. 97-104.

[36] J. Choi *et al.*, "Thin-film piezoelectric and high-aspect ratio polymer leg mechanisms for millimeter-scale robotics," *International Journal of Intelligent Robotics and Applications,* vol. 1, no. 2, pp. 180-194, 2017.

[37] C. Rhee, J. Pulskamp, R. Polcawich, and K. Oldham, "Multi-Degree-of-Freedom Thin-Film PZT-Actuated Microrobotic Leg," *Journal of Microelectromechanical Systems,* vol. 21, no. 6, pp. 1492-1503, 2012.

[38] X. Zhang *et al.*, "A Fully Integrated Battery-Powered System-on-Chip in 40-nm CMOS for Closed-Loop Control of Insect-Scale Pico-Aerial Vehicle," *IEEE Journal of Solid-State Circuits,* vol. PP, no. 99, pp. 1-14, 2017.

[39] X. Zhang, T. Tong, D. Brooks, and G. Y. Wei, "Evaluating Adaptive Clocking for Supply-Noise Resilience in Battery-Powered Aerial Microrobotic System-on-Chip," *IEEE Transactions on Circuits and Systems I: Regular Papers,* vol. 61, no. 8, pp. 2309-2317, 2014.

[40] M. Karpelson, J. P. Whitney, G. Y. Wei, and R. J. Wood, "Energetics of flapping-wing robotic insects: towards autonomous hovering flight," in *2010 IEEE/RSJ International Conference on Intelligent Robots and Systems*, 2010, pp. 1630-1637.

[41] K. Teichert and K. Oldham, "Dynamics and characteristics of thin film batteries cycled over capacitive load," in *IEEE International Conference on Advanced Intelligent Mechatronics (AIM)*, Banff, Canada, 2016.

[42] K. Teichert and K. Oldham, "Modeling Cyclic Capacitive Loading of Thin-Film Batteries," *Journal of The Electrochemical Society,* vol. 164, no. 2, pp. A360-A369, 2017.

[43] K. Teichert and K. Oldham, "Simulation of thin-film battery response to periodic loading by a transition matrix approximation using boundary and nonlinearity error analysis," *Journal of Energy Storage (Under Review)*, 2017.

[44] K. Oldham, B. Hahn, and P. Park, "On-off Control for Low-power Servo Control in Piezoelectric Mico-robotics," in *ASME Dynamic Systems and Control Conference*, 2008, pp. 1035-1042.

[45] K. Oldham, B. Edamana, and B. Hahn, "Coordinated voltage conversion and low-power micro-actuator switching," in *ASME Dynamic Systems and Control Conference and Bath/ASME Symposium on Fluid Power and Motion Control (DSCC)*, 2011, vol. 2, pp. 33-40.

[46] Cymbet. (2016). *Enerchip CBC050*. Available: http://www.cymbet.com/pdfs/DS-72-01.pdf

[47] K. Furset and P. Hoffman, "High pulse drain impact on CR2032 coin cell battery capacity," Available: http://m.eet.com/media/1121454/c0924post.pdf

[48] Cymbet. *EnerChip Standards Compliance and Use Procedures*. Available: www.cymbet.com/pdfs/PI-72-04.pdf

[49] H. Dadgour and K. Banerjee, "Design and analysis of hybrid NEMS-CMOS circuits for ultra low-power applications," *2007 44th ACM/IEEE Design Automation Conference*, vol. 1 and 2, pp. 306-311, 2007.

[50] A. Peschot, C. Qian, and T. Liu, "Nanoelectromechanical Switches for Low-Power Digital Computing," *Micromachines*, vol. 6, no. 8, pp. 1046-1065, 2015.

[51] B. Stark, P. Mitcheson, P. Miao, T. Green, E. Yeatman, and A. Holmes, "Converter circuit design, semiconductor device selection and analysis of parasitics for micropower electrostatic generators," *IEEE Transactions on Power Electronics*, vol. 21, no. 1, pp. 27-37, 2006.

[52] X. Hu, S. Li, and H. Peng, "A comparative study of equivalent circuit models for Li-ion batteries," *Journal of Power Sources*, vol. 198, pp. 359-367, 2012.

[53] Y. Zhou, M. Xue, and Z. Fu, "Nanostructured thin film electrodes for lithium storage and all-solid-state thin-film lithium batteries," *Journal of Power Sources*, vol. 234, pp. 310-332, 2013.

[54] K. Cook-Chennault, N. Thambi, and A. Sastry, "Powering MEMS portable devices - a review of non-regenerative and regenerative power supply systems with special emphasis on piezoelectric energy harvesting systems," *Smart Materials and Structures*, vol. 17, no. 4, 2008, Art. no. 043001.

[55] Y. Wang *et al.*, "Lithium and lithium ion batteries for applications in microelectronic devices: A review," *Journal of Power Sources,* vol. 286, pp. 330-345, 2015.

[56] A. Vu, Y. Qian, and A. Stein, "Porous Electrode Materials for Lithium-Ion Batteries - How to Prepare Them and What Makes Them Special," *Advanced Energy Materials,* vol. 2, no. 9, pp. 1056-1085, 2012.

[57] J. Kim *et al.*, "A review of lithium and non-lithium based solid state batteries," *Journal of Power Sources,* vol. 282, pp. 299-322, 2015.

[58] K. Chen, Y. Shen, Y. Zhang, Y. Lin, and C. Nan, "High capacity and cyclic performance in a three-dimensional composite electrode filled with inorganic solid electrolyte," *Journal of Power Sources,* vol. 249, pp. 306-310, 2014.

[59] T. F. Fuller, M. Doyle, and J. Newman, "Relaxation Phenomena in Lithium-Ion-Insertion Cells," *Journal of The Electrochemical Society,* vol. 141, no. 4, pp. 982-990, 1994.

[60] A. Rahmoun and H. Biechl, "Modelling of Li-ion batteries using equivalent circuit diagrams," *Przeglad Elektrotechniczny,* vol. 88, no. 7B, pp. 152-156, 2012.

[61] H. He, R. Xiong, and J. Fan, "Evaluation of Lithium-Ion Battery Equivalent Circuit Models for State of Charge Estimation by an Experimental Approach," *Energies,* vol. 4, no. 4, pp. 582-598, 2011.

[62] S. K. Rahimian, S. Rayman, and R. E. White, "Comparison of single particle and equivalent circuit analog models for a lithium-ion cell," *Journal of Power Sources,* vol. 196, no. 20, pp. 8450-8462, 2011.

[63] M. Park, X. Zhang, M. Chung, G. Less, and A. Sastry, "A review of conduction phenomena in Li-ion batteries," *Journal of Power Sources,* vol. 195, no. 24, pp. 7904-7929, 2010.

[64] B. Hahn, "Energy Efficient Iterative Adaptive On-Off Control of Capacitively-Loaded Actuators for Micro-robots," PhD, Mechanical Engineering, University of Michigan, 2012.

[65] A. Deshpande, S. Phul, and B. Krishnamurthy, "A generalized mathematical model to understand the capacity fading in lithium ion batteries effects of solvent and lithium transport," *J. Electrochem. Sci. Eng.*, 2015.

[66] R. L. Spencer and M. Ware, *Computational Physics 430, Partial Differential Equations (Course Packet)* (Department of Physics and Astronomy, Brigham Young University). Department of Physics and Astronomy, Brigham Young University, 2012.

[67] M. Bowen and R. Smith, "Derivative formulae and errors for non-uniformly spaced points," *Proceedings of the Royal Society a-Mathematical Physical and Engineering Sciences,* vol. 461, no. 2059, pp. 1975-1997, 2005.

[68] B. Edamana, B. Hahn, J. S. Pulskamp, R. G. Polcawich, and K. Oldham, "Modeling and Optimal Low-Power On-Off Control of Thin-Film Piezoelectric Rotational Actuators," *IEEE/ASME Transactions on Mechatronics,* vol. 16, no. 5, pp. 884-896, 2011.

[69] M. R. Jongerden and B. R. Haverkort, "Which battery model to use?," *IET Software,* vol. 3, no. 6, pp. 445-457, 2009.

[70] S. D. Jones and J. R. Akridge, "A microfabricated solid-state secondary Li battery," *Solid State Ionics,* vol. 86, pp. 1291-1294, 1996.

[71] S. Ferrari, M. Loveridge, S. Beattie, M. Jahn, R. Dashwood, and R. Bhagat, "Latest advances in the manufacturing of 3D rechargeable lithium microbatteries," *Journal of Power Sources,* vol. 286, pp. 25-46, 2015.